The Synthesis and Validation of Multimodal PET/Fluorescence Zinc Sensing Probes as Potential Imaging Agents for Prostate Cancer

---

Thesis Submitted for the Degree of
MSc Biological Sciences
at the University of Hull

by

George Firth BSc
School of Life Sciences

August 2017

Abstract

Prostate cancer (PCa) is the 2nd most common cancer worldwide for males, and the 4th most common cancer overall, accounting for 15% of all male cancers in 2012. PCa is asymptomatic in its early stages, advances in medical imaging are improving diagnosis, however novel simple medical imaging agents are needed to diagnose the disease early. A fluorescent imaging probe, 2-((2-(2-fluoroethoxy)ethyl)amino)-N-(quinolin-8-yl)acetamide (AQA-F), that changes emission profile when binding the metal zinc has been synthesised. A Stokes shift of 80 nm can be observed upon zinc binding, enhancing the emission wavelength from 420 to 500 nm, with a K_d of $14x10^{-6}$ M. It was shown that AQA-F has the highest affinity for Zn^{2+} which will allow for the *in vitro* differentiation of zinc bound and free probe. AQA-F was non-toxic at imaging concentrations in healthy prostate, prostate cancer and healthy tissues. It was also shown that AQA-F was internalised by healthy and prostate cancer cell lines across both 2D and 3D models. This allows for the probe to function as an endogenous zinc sensor *in vitro* with the potential of being translated into clinical use for the diagnosis of prostate cancer in men. Further studies will be required to identify a radiolabelling procedure for the probe with ^{18}F to enable possible dual modal imaging.

Declaration

The work described in this thesis was performed solely by the author unless stated otherwise and the results reported reflect true and accurate findings of the work. All experiments were carried out in accordance with the University of Hull's Health and Safety guidelines. A full COSHH and risk assessment was carried out for each new experiment, signed by the undertaking student, supervisor (Dr Graeme Stasiuk) and the departmental safety officer (Dr Tom McCreedy) before any practical work started. Copies of each form were provided for reference to the departmental safety officer and supervisor. The COSHH forms carry the reference numbers GF001 and GF002.

The cell lines used during this project are commercially available and were derived from patient biopsies who gave their informed consent for the use of their cells in research. The research undertaken in this thesis is ethically approved and each experiment was performed without any deviation from the human tissue act 2004.

Acknowledgements

I would like to give special thanks to all those that have provided not only their time but also their expertise to assist me throughout this project. Firstly, I would like to say thanks to my supervisors Dr Graeme Stasiuk and Dr Justin Sturge for all their help and guidance during my masters and for making me feel like not only a student, but part of the research group. Thanks to Thomas Price who was invaluable when completing this thesis, who always had time to listen and discuss various areas of the project, and without him the transition from biomedical science to chemistry wouldn't have been achievable. Thank you to Charlotte Eling for help with all things physics including recording the fluorescence, absorbance and quantum yields measurements. Special thanks to my good friend Mitchell Clarke who was invaluable in all things chemistry and provided brilliant feedback throughout the year. Thanks to Michelle Kinnon for previous work on the probe and to the rest of the Stasiuk group who always made me feel welcome. Lastly I would like to say thanks to Kamil Talar for providing assistance with the 3D models and always offering help when asked and to Dr Cordula Kemp for assistance with the confocal microscope.

Table of Contents

Abbreviations

Abbreviation	Connotations
^{18}F-FDG	^{18}F-Fluoro-deoxyglucose
AQA-OH	2-((2-(2-hydroxyethoxy)ethyl)amino)-N-(quinolin-8-yl)acetamide
AQA-F	2-((2-(2-fluoroethoxy)ethyl)amino)-N-(quinolin-8-yl)acetamide
AQA-Gd	Gd·2,2',2''-{[2-aminoethoxy-ethyl-N-(quinol-8-yl)acetamide]-1,4,7,10-tetraazacyclododecane- 1,4,7-triacetate}
BPE	Bovine pituitary extract
BPH	Benign prostatic hyperplasia
CT	Computed tomography
DAPI	4',6-Diamidino-2-phenylindole nuclear Stain
DCM	Dichloromethane
DIPEA	N-N-diisopropyethylamine
DMEM	Dulbecco's modified eagle's medium
DMF	Dimethylformamide
DMSO	Dimethyl sulfoxide
DRE	Digital rectal examination
EGF	Human recombinant epidermal growth factor
ESI	Electrospray Ionisation
EtOAc	Ethyl acetate
FBS	Fetal bovine serum
FTIR	Fourier-transform infrared spectroscopy
g	Gram
HEK293	A human embryonic kidney cell line
LD_{50}	Lethal dose
M	Molar
MAX OD	The maximum optical density
MeCN	Acetonitrile
MeOH	Methanol
mg	Milligram
mL	Millilitre
MRI	Magnetic resonance imaging
NMR	Nuclear magnetic resonance
MS	Mass spectroscopy
PBS	Phosphate buffered saline
PCa	Prostate cancer
PenStrep	A penicillin streptomycin mixture that contains penicillin G in a sodium salt form as well as streptomycin sulphate in 0.85% saline.
PET	Positron emission tomography
PSMA	Prostate specific membrane antigen
PSA	Prostate specific antigen
rBM	Reconstituted basement membrane
RWPE-1	Human epithelial prostate cell line
RWPE-2	Ras-mutated human epithelial prostate cell line
S_N2	Bimolecular nucleophillic substitution
TEA	Triethylamine
TFA	Trifluoroacetic acid
TNM	Tumour node metastasis classification system
TRUS	Transrectal ultrasound scan
ZIP1	Zrt-like Irt-like Protein 1

List of figures:

List of tables:

1.0. INTRODUCTION

1.1. Prostate Gland

The human prostate is a small walnut-sized gland located below the bladder which forms part of the urethra. This tubuloalveolar exocrine gland is a major part of the male reproductive system where it produces seminal fluid to help promote fertility and spermatozoa growth and mobility (Perry *et al,* 2013). The gland weighs approximately 8 grams in young males and grows with age reaching around 40 grams, and as large as 150 grams by the age of 50 (Standring and Gray, 2008). The location of where the prostate gland lies within the male reproductive system can be seen in **Figure 1**.

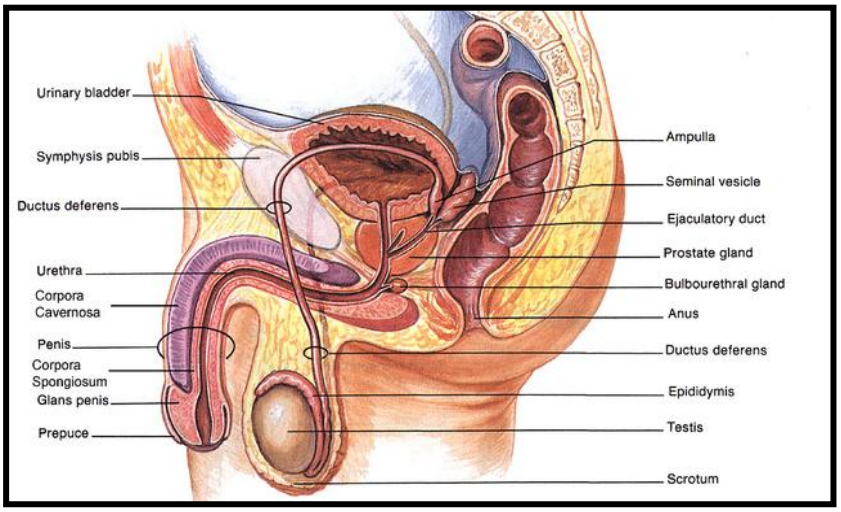

Figure 1: This diagram represents the male reproductive system and the different components of that system (Stanfield, 2013).

The prostate gland has dimensions of approximately 2x3x4cm and consists of four histological zones which include: the peripheral, central, transition and anterior fibromuscular zones. Most carcinomas are associated with the peripheral zone and rarely the central zone (Standring and Gray, 2008); whereas benign prostate hyperplasia (BPH) largely occurs in the transition zone. This results in the increase in

size seen later in life (Standring and Gray, 2008). Seminal fluid is composed of a range of components including: citrate, zinc, seminal plasma and prostatic specific antigen (PSA). This multicomponent fluid is secreted by highly specialised epithelial present in the peripheral zone, with the peripheral zone accounting for 70% of the volume of the gland (McNeal, 1981).

1.2. Prostate Cancer

Prostate cancer is the most common non-cutaneous malignancy in men in the United Kingdom, accounting for an estimated 1.1 million cases worldwide in 2012 (Torre *et al*., 2015). Prostate cancer is defined as the unregulated differentiation of epithelial cells in the prostate gland. It is more commonly seen in men over the age of 60 with African-American men at an increased risk. A family history of prostate cancer can also increase the risk of prostatic malignancy (Potter and Partin, 2000), for example a man who has a first degree relative with a history of prostate cancer can be twice as likely to develop a malignancy.

1.2.1 Staging

Prostate cancer is a progressive disease that can take decades to manifest; this slow progression allows it to be staged, primarily using the Gleason grading system (Gleason & Mellinger, 1974). This histological staining system allows the clinician to determine prognosis and to select a suitable method of treatment for the patient. A simple haematoxylin and eosin (H+E) stain is used where the nucleus is stained blue by

the haematoxylin and the cytoplasm pink by eosin. Once the tissue sample has been stained, differentiation patterns can be grouped together to form a grade.

Grade 1 is associated with a well differentiated cluster of cells that are uniform and separate. This rare grade lacks tumour infiltration with a similar arrangement to adenosis and is classed as a low grade tumour.

Grade 2 is a well differentiated pattern that looks similar to grade 1; however an inconsistency can be seen in cell spacing and the size of cells (Humphrey, 2004).

Grade 3 is the most common histological pattern seen in prostate cancer, with the majority of scores being 3+3=6, and can be further characterised into three sub patterns: A, B and C. 3A consists of medium sized glands that are inconsistent in shape and spacing with stromal infiltration. 3B is very similar to 3A, however it possesses smaller glands. 3C is comprised of papillary tumours with no necrosis. These sub classes are not necessary when calculating the Gleason score and are instead used to better identify grade 3 (Humphrey, 2004).

Grade 4 represents a high grade tumour that possesses poorly differentiated cells and can be sub divided into A and B. 4A corresponds to infiltrating fused or chained cells forming the tumour which are also seen in 4B, however ragged edges of cells is indicative of 4B (Humphrey, 2004).

Grade 5 is the highest grade a prostate cancer can be and represents the most poorly differentiated pattern. It can present as two types, A and B, however both sub classes are associated with the presence of necrosis and solid masses that vary in size (Humphrey, 2004).

The following grades can be seen highlighted below in **table 1**.

Table 1: This table illustrates the Gleason grading system first established by Gleason & Mellinger in 1974 and contains key information about each grade (Humphrey, 2004).

Grade 1	Well differentiated	Tightly packed cells	No infiltration	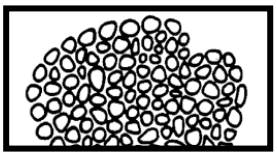
Grade 2	Well differentiated	Gland size and spacing varies	Some infiltration into stroma	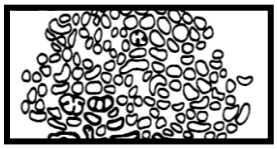
Grade 3	Well differentiated	Medium sized glands, marked size irregularity	Infiltration into the stroma	
Grade 4	Poorly differentiated	Irregular shape and unevenly spaced, some glands are not formed properly	Infiltration cells, often fused together	
Grade 5	Undifferentiated	Lack of gland formation	Sheets or clusters of infiltrating tumour cells	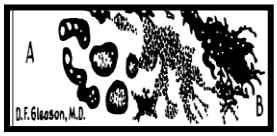

A Gleason score is then determined by adding the two most common patterns together with a range of 2-10. A Gleason score of less than 5 should not be investigated using a needle core biopsy due to poor reproducibility (Gordetsky and Epstein, 2016). A score of 8-10 is associated with a high grade tumour and is more likely to metastasise and proliferate at a faster rate. Although this grading system is currently used, it does have its disadvantages. For example, it is subjective and therefore has issues with under or over grading the carcinoma. To overcome this, staging methods are used in combination with other diagnostic methods to predict the prognosis and clinical management for a patient (Humphrey, 2004).

The tumour node metastasis (TNM) system is often applied in a clinical setting to diagnose prostate cancer. It uses: the size of a tumour and its localisation (abbreviated to T), lymph node involvement (abbreviated to N) and the presence of metastasis (abbreviated to M) (Sobin *et al,* 2010). This particular system can be characterised by stage I, represented by a small localised cancer, to stage IV associated with a metastatic cancer.

One example of collaboration between these two techniques is the D'Amico risk group stratification model. This model also uses the preoperative PSA level to assess the risk of the disease. This information is then used in combination to determine a method of treatment and to estimate the prognosis of the patient (Hernandez *et al,* 2007).

The following risk categories are defined as:

- **Low risk –** PSA level ≤10 ng/ml, Gleason score ≤6 and T1c-T2a.
- **Intermediate risk –** PSA level 10.1-20 ng/ml, Gleason score of 7, T2b.
- **High risk –** PSA level >20 ng/ml, Gleason score 8-10, T2c.

1.2.2 Diagnosis

The diagnosis of prostate cancer uses multiple techniques in combination to provide a reliable and effective diagnosis. Currently, these techniques include: analysing prostate specific antigen (PSA) levels, performing prostate biopsies, performing a digital rectal examination (DRE) and undertaking a trans-rectal ultrasound scan (TRUS). Prostate cancer is a progressive disease which is most curable when diagnosed early, however it is often asymptomatic in its early stages. Early malignant development is confined to the prostate gland and small tumours have little effect on surrounding tissue (Nash and Melezinek, 2000). Prostate cancer in its late stages can metastasise to the bone, lymph nodes, rectum and bladder. Metastasis is responsible for 90% of cancer patient mortality therefore highlighting the importance of identifying and preventing the progression of prostate cancer to decrease metastatic potential (Hanahan and Weinburg, 2011). Current techniques can't diagnose prostate cancer in its early stages; therefore a more specific biomarker is required. Zinc has shown promise as a marker for prostate cancer, which if successful could minimise over diagnosis, overtreatment and better differentiate between mild and aggressive forms of malignancy (Cuzick *et al,* 2014).

PSA is a serine protease that is measured to diagnose prostate cancer as it is shed by prostate cancer cells and so its levels are increased in the blood compared to normal (Lilja *et al,* 2008). Total PSA levels higher than 4 ng/ml are considered abnormal and are often followed with a biopsy to confirm the diagnosis, however on average 75% of these show no evidence of prostate cancer (Hong, 2014). The reference ranges for PSA is therefore a controversial topic as unnecessary biopsies can cause anxiety and further risks to healthy patients. The Prostate Cancer Risk Management Programme (PCRMP)

recommends a multiple core sampling technique where at least ten cores covering all parts of the gland are biopsied using ultrasound-guided techniques (Eskicorapci *et al*., 2004). This method allows for a representative sample of the prostate gland to be obtained, however this blind systematic technique is not ideal with the possibility of oversampling benign disease and undersampling significant disease (Briganti *et al,* 2015).

Total PSA levels lower than 4 ng/ml can also be seen in patients with prostate cancer, therefore PSA is not used exclusively to diagnose prostate cancer (Thompson *et al*, 2004). There are many factors that could influence the PSA value, examples include: age, weight and a DRE performed shortly before measuring PSA can cause PSA levels to rise. PSA is not disease specific and can be seen elevated in prostate cancer and benign prostatic hyperplasia (BPH). To overcome this, free and bound PSA, as well as PSA density, can be used in combination with total PSA to increase prostate cancer specificity (Loeb and Catalona, 2007). Elevated total PSA can be seen during the early progression of prostate cancer; however the problem lies with identifying risk groups and screening early enough to see these changes (Botchorishvili *et al,* 2009).

Magnetic resonance imaging (MRI) can also be used to diagnose prostate cancer. Diffusion weighted magnetic resonance imaging (DW-MRI) is an example of MRI that uses image contrast obtained as a result of the difference in the rate of water molecules moving through different tissues to generate an image (Koh and Collins, 2007). The differences in tissue structure of normal prostate and prostate cancer provide the potential for a high image contrast (Koh and Collins, 2007). The benefits of this method can be seen highlighted in **Table 2**.

Table 2: A table to highlight the advantages and disadvantages for different methods of detecting prostate cancer.

Method of diagnosis	Advantages	Disadvantages	Reference(s)
Biopsy	Most accurate way to detect prostate cancer Quick process Highly effective when used in combination with MRI	Invasive Risk of injury or damage to the prostate gland	Presti 2007
Diffusion Weighted MRI (DW-MRI)	Produces images with high contrast No imaging agents required	Ineffective at imaging movement, for example in the chest and abdomen	Tamada *et al,* 2013
Digital rectal examination (DRE)	No special equipment required Cost effective	Uncomfortable Small nodules may not be noticed Time consuming	Walker 1990
^{68}Ga-PSMA-PET	Increased expression in prostate cancer Higher accuracy than PET/CT Produced on site so can be used immediately	Radioactive Results suggest PSMA expression does not correlate with gleason score Short half-life means radiotracer must be produced on site	Afshar-Oromieh *et al,* 2015 Afshar-Oromieh *et al,* 2014
Prostate specific antigen (PSA)	Good at detecting early prostate cancer	Only 25% of abnormal results (4-10 ng/ml) are prostate cancer Abnormal results could lead to further unnecessary tests	Stricker 2001
Trans-rectal ultrasound scan (TRUS)	Used alongside a biopsy needle to help guide sample collection	Poor at detecting anterior, apical and central lesions Damage can occur	Norberg et al, 1997

1.2.3 Zinc

Zinc (Zn^{2+}) is a d^{10} transition metal that is well documented to play a vital role as a co-factor for many structural and regulatory enzymes. Zn^{2+} is the second most abundant transition metal in the body and has been recognised as a potential diagnostic marker for the progression of prostate cancer (Franklin and Costello, 2011). This is due to the large concentrations found in the prostate, with zinc levels in the peripheral zone of the prostate gland being ten times greater than any other tissue (Costello and Franklin, 2011). Zinc concentrations in the prostate gland were first determined as early as the 1920's, where Bertrand and co-workers (1921) estimated that the prostate contained 489 and 533 μ/g in the left and right lobes respectively.

The homeostasis and localisation of Zn^{2+} is important to understand as there is subtle differences in this pathway between a healthy and disease state that can be utilised to diagnose prostate cancer. In the healthy prostate, Zn^{2+} enters a specific citrate secreting cell, known as the peripheral zone acinar secretory epithelial cell, *via* the Zrt-like, Irt-like protein 1 (ZIP1) transporter. Costello and Franklin, 2016 have shown that zinc uptake increases when ZIP1 levels are upregulated, with endogenous zinc levels decreasing during ZIP1 downregulation. Once Zn^{2+} moves into the cell, it inhibits the enzyme *m*-aconitase, which catalyses the conversion of citrate into isocitrate, therefore inhibiting citrate oxidation and promoting the secretion of citrate.

In prostate cancer, the gene that codes for ZIP1 (*SLC93A1*) possesses a mutation which results in the downregulation of the zinc transporter. As a result of this, *m*-aconitase is no longer inhibited allowing citrate to be oxidised and used to generate ATP through the Krebs cycle. It has been shown that intracellular Zn^{2+} levels can be 62-75% lower

than healthy prostate tissue concentrations (Franklin *et al,* 2005). This increase in the generation of ATP promotes the rapid cellular proliferation seen in malignant cells. This process can be seen highlighted in **Figure 2**. These ZIP1 deficient malignancies can theoretically be diagnosed long before current methods using zinc sensing probes to identify the decrease in intracellular zinc concentration. A study by Rishii *et al.* in 2003 has shown that ZIP1 gene expression is lower in African-American compared to matched Caucasians, supporting the evidence for the increased risk seen in African-American men.

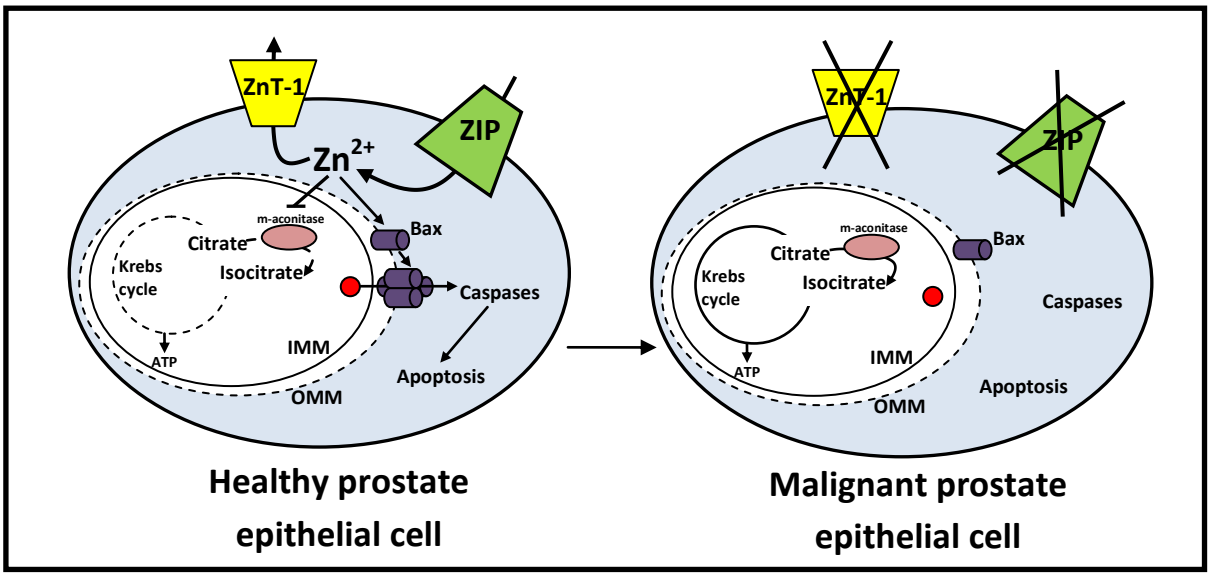

Figure 2: A diagram to summarise the differences in the zinc metabolic pathway in a healthy prostate and a malignant prostate cell (modified from Costello and Franklin, 2006b). ZIP: Zrt-like, Irt-like Protein, ZnT-1: zinc transporter 1, IMM: inner mitochondrial membrane, OMM: outer mitochondrial membrane, Bax: BCL-2-associated X protein, Cyt-C: cytochrome-C, ATP: adenosine triphosphate.

1.3. Molecular Imaging

Molecular imaging is a multi-disciplinary field that non-invasively visualises human physiology. This functional imaging technique involves the visualisation of physiological processes at the sub-cellular level. Molecular imaging modalities can be categorised into five main branches which include: optical imaging (OI), X-ray computed tomography (CT), radionuclide imaging (positron emission tomography (PET) and single photon emission computed tomography (SPECT)), magnetic resonance imaging (MRI) and multispectral optoacoustic tomography (MSOT).

1.3.1. Positron Emission Tomography

Positron emission tomography (PET) is a method of medical imaging that constructs a three dimensional image of a functional process by using the annihilation of a positron from a tracer. Positron emission, also known as beta decay, from the radiotracer is used to diagnose disease as the tracer localises to the area of interest and the decay can be detected. The emitted positron travels a short distance (0.5-2.0 cm) before colliding with an electron resulting in annihilation and the production of two 511 keV gamma rays (Miller *et al,* 2008). These gamma rays travel in opposite directions simultaneously until they are converted in to photons by the scintillator, which are recognised in temporal pairs by the surrounding detectors (Amatemey *et al,* 2008). This process can be seen simplified as a diagram in **Figure 3**.

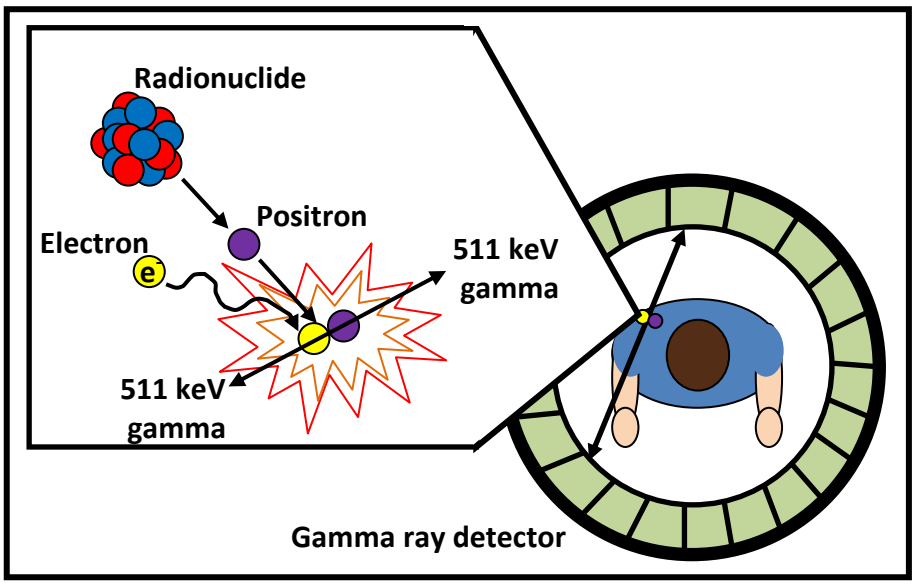

Figure 3: An illustration highlighting the basic principles of positron emission tomography.

1.3.2. PET Radioisotopes

There is an arsenal of radioisotopes that chemists can use to radiolabel compounds and choosing the right one is vital to meet medical imaging/disease states needs. An isotopes half-life, that is the time it takes for half of the radionuclide to decay, often governs the chemist's choice as probes are generally synthesised and purified within minutes. Therefore, radionuclides with a short half-life such as ^{11}C (20.4 minutes) and ^{18}F (110 minutes) are commonly synthesised in proximity to the PET scanner reducing transport time and allowing them to be used immediately following their synthesis (Miller *et al,* 2008). Long lived isotopes can be beneficial as they can be imaged once the probe gets washed out of non-significant areas, producing an image with lower background and therefore better contrast. A range of radionuclides can be seen in **table 3**.

Table 3: A table highlighting different radioisotopes, half-life and decay products (Miller *et al,* 2008. Asabella *et al,* 2014, Price *et al,* 2016).

Radionuclide	Half-life, $t_{1/2}$ (min)	Decay Process	Decay Product
^{11}C	20	β^+ (100%)	^{11}B
^{13}N	10	β^+ (100%)	^{13}C
^{15}O	2	β^+ (100%)	^{15}N
^{18}F	110	β^+ (96.9%) γ (3.1%)	^{18}O
^{64}Cu	762	β^+ (19%) γ (43%) β^- (38%)	^{64}Zn ^{64}Ni
^{68}Ga	68	β^+ (90%) EC (10%)	^{68}Zn
^{89}Zr	4710	EC (77%) β^+ (23%)	^{89}Y

1.3.3. ^{18}F-Fluoro-deoxyglucose

Radiotracers can be analogues of compounds from normal physiological pathways or they can be targeted probes which use specific binding interactions to localise an area of interest (Miller *et al,* 2008). An example of a radiotracer is ^{18}F-Fluoro-deoxyglucose (^{18}F-FDG) which is currently used in the UK in more than 90% of oncologic PET imaging (Zhu *et al,* 2012). ^{18}F-FDG is an analogue of glucose first synthesised by electrophilic fluorination in 1976 by Wolf *et al*, which uses normal physiological pathways to localise to an area of interest. The uptake of ^{18}F-FDG in tumours is greater than that of normal tissue, due to increased glucose metabolism in neoplastic tissue, allowing the identification and the staging of cancer (Hoh, 2007). This method is not perfect; ^{18}F-FDG is non-specific and so struggles differentiating between malignant and benign lesions (Zhu *et al,* 2012). PET can also be combined with other imaging modalities to overcome associated disadvantages, for example PET/CT is currently implemented to combine the anatomical power of CT with the metabolic functional imaging. This technique, seen in **figure 4**, can more accurately differentiate between normal organ uptake and pathological uptake in tumours (Langer, 2010).

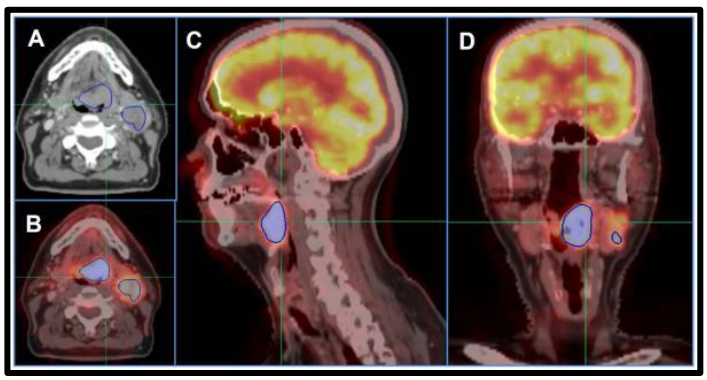

Figure 4: An image of a FDG-PET/CT scan showing a 62 year old male with squamous cell carcinoma of the tongue. (A) Axial CT image; (B) Axial integrated PET/CT image; (C) Sagittal integrated PET/CT image; (D) Coronal integrated PET/CT image (Zhu *et al,* 2012).

1.3.4. Prostate Specific Membrane Antigen (PSMA)

PET tracers are used depending on the cancer and specificity of the probe. These mostly include: ^{11}C labelled compounds and ^{18}F labelled compounds (Bouchelouche *et al,* 2011). ^{11}C-acetate has shown promise at imaging hepatocellular carcinomas whereas prostate cancer is most commonly imaged using ^{11}C labelled choline (Beadsmoore *et al,* 2015). Novel radiotracers are in development with the aim of improving the ability to differentiate between biologically aggressive and benign forms of cancer.

Prostate specific membrane antigen (PSMA), a type II transmembrane receptor found on the epithelial prostate cell membrane, has shown to be considerably upregulated 100-1000 fold in prostate cancer cells compared to normal physiologic levels in other epithelial cells (Maurer *et al,* 2016). As a result of this upregulation, PSMA is showing promise as a radiotracer target (Lindenberg *et al,* 2016).

PSMA-based PET imaging agents fall into three categories: antibodies, aptamers, and PSMA inhibitors of low molecular weight. Glu-NH-CO-NH-Lys(Ahx)-HBED-CC (^{68}Ga-PSMA-HBED-CC) is a low molecular weight urea-based PSMA inhibitor first synthesized by Eder *et al,* 2012 that is currently the most common agent for imaging the prostate (Maurer *et al,* 2016). Once the probe binds to PSMA it is internalized and can be imaged, showing large concentrations even in small metastases from the primary cancer. One major benefit to this inhibitor is that it can be easily labelled with radioactive ^{68}Ga at room temperature on site (Roesch and Riss, 2010), therefore reducing the time from production to clinical use. Other families of PSMA-inhibitor include those that are thiol-based and phosphorous-based; however urea-based

inhibitors are more common as a result of their high affinity and specificity for PSMA (Maurer *et al,* 2016). ^{18}F-labelled PSMA inhibitors have shown promise in prostate cancer imaging and may be advantageous over their ^{68}Ga counterparts. For example, ^{18}F is produced in larger concentrations from a cyclotron compared with ^{68}Ga generators (Dietlein *et al,* 2015). This would allow clinicians to perform more imaging examinations using ^{18}F-labelled PSMA inhibitors; however a greater number of pre-clinical and clinical studies of these compounds are required for clinical application.

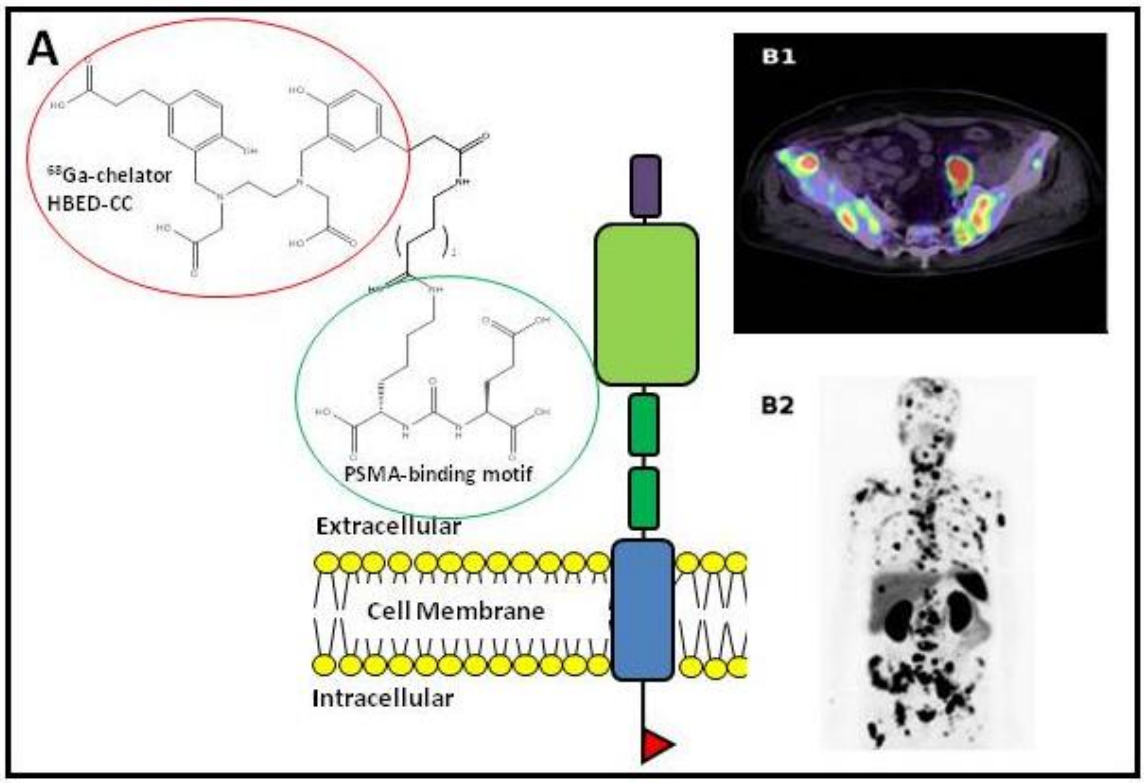

Figure 5: An image highlighting (A) a diagramatic representation of the PSMA receptor and how the radiotracer binds to its target. (B1) PET/CT scan and (B2) maximum intensity projection (MIP) of a patient with lymph node and bone metastases from prostate cancer (Afshar-Oromieh *et al,* 2013).

Another example of a PMSA-specific binding probe is [^{18}F]DCFPyL which has the advantage of providing a theranostic response whereby cancer is not only diagnosed but is also treated. [^{18}F]DCFPyL also has benefits at imaging castration-resistant cancers which can often not be assessed using PSA in isolation (Szabo *et al,* 2015). Its specificity and sensitivity for prostate cancer show promise as a widely available radiotracer for the clinic, with a binding affinity five times greater than its predecessor ^{18}F DCFBC (Szabo *et al,* 2015).

1.3.5. Fluorescence

Fluorescence is defined as a form of luminescence that involves the emission of light following the absorption of light. This process involves the excitation of electrons to a higher energy state as a result of photon absorption. During this excited state (S_n where n>0), an electrons can return to the ground state (S_0) using many different pathways. These pathways include: internal conversion which involves returning to the ground state without fluorescence, vibrational relaxation and intramolecular charge transfer. Fluorescence occurs as a result of the loss of energy as the electron returns to S_0 through vibrational relaxation. This process follows Kasha's rule which states that photon emission is greatest when returning from the lowest excited state (S_1). This loss of energy causes the release of a low energy photon that has a longer wavelength than the absorbed photon (Valeur, 2002). The principles of fluorescence can be seen in **Figure 6**. The Stokes shift is defined as "the gap between the maximum of the first absorption band and the maximum of the fluorescence spectrum" measured in wavelengths (Valeur, 2002).

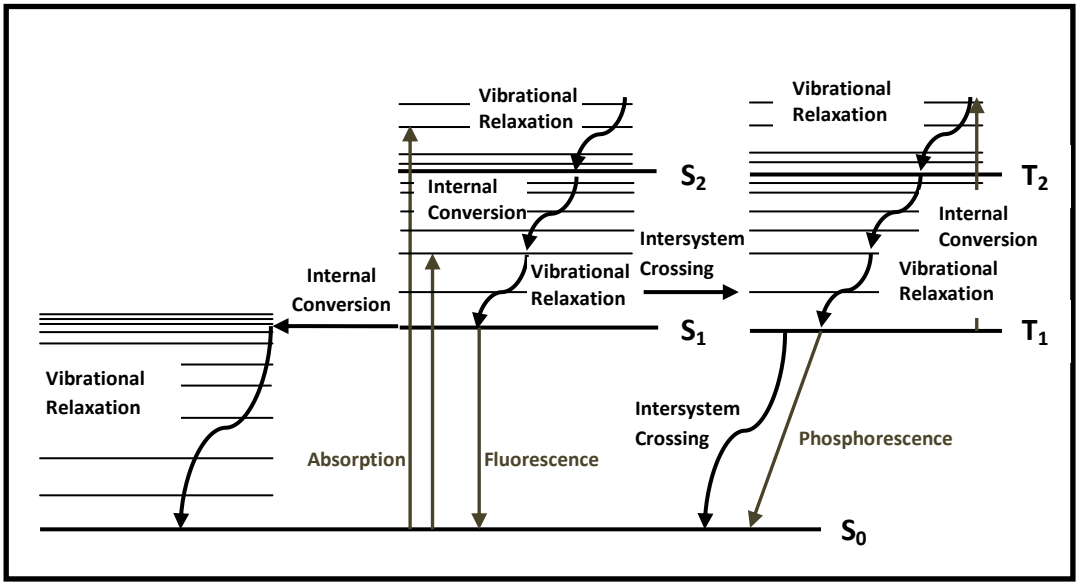

Figure 6: An illustration of a Jablonski diagram which summarises the release of a photon due to the excitation to a higher energy state and the return to the ground state (Sauer *et al,* 2011).

Fluorescence imaging is associated with having a high specificity and contrast, which makes it a highly sensitive method for analysing protein-protein interactions (Hamdan, 2007). It also has applications as a tool to guide surgery as surgeons have a real time visualisation of the designated operating area. This method of application overcomes the low tissue penetration associated with fluorescence; however a fluorescent probe such as indocyanine green (ICG) emits in the near infrared spectrum at 800nm so has some tissue penetration. Many fluorescent probes are at a disadvantage as a result of photo bleaching therefore many probes are being designed using a dual modal approach (Frangioni, 2003).

1.4. Zinc Sensing

Decades of research has focused on zinc and its relationship with prostate cancer. During this period of research, many zinc sensing probes have been produced with the aim of improving the early diagnosis of disease (Nolan and Lippard. 2009, Ghosh *et al.* 2010, Stasiuk *et al.* 2015). It is well known that zinc concentrations are significantly lower in prostate cancer; this zinc depletion is not seen in prostatitis or benign prostate hyperplasia (BPH) allowing zinc to be a potential specific marker of prostate cancer (Costello and Franklin, 2009).

Di-2-picolylamine (DPA) is a common zinc binding motif that has been incorporated into many fluorescent probes (Walkup *et al*, 2000, Burdette *et al*, 2001). DPA provides a change in fluorescence intensity upon binding zinc, however there is only a limited change in emission wavelength. Zinpyr-1 (ZP1) is a fluorescein-based DPA probe that binds to mobile zinc and produces an excitation maximum at 507 nm, compared to 515 nm when unbound (Walkup *et al,* 2000). While highly sensitive, this zinc binding unit may not be suitable for quantifying intracellular Zn^{2+} as changes may be due to other factors such as concentration. For the purpose of measuring endogenous zinc, a probe which changes emission wavelength upon zinc binding is desired to differentiate between zinc-free probe and zinc-bound probe.

A water-soluble quinoline-based zinc binding probe has been developed by Zhang *et al,* (2008) and has showed success in fluorescence studies when binding to zinc. 2-((2-(2- hydroxyethoxy)ethyl)amino)-N-(quinolin-8-yl)acetamide (AQA-OH) has a large Stokes shift of 90 nm upon binding zinc compared to 8 nm with ZP1. This large green shift allows for better differentiation between zinc-bound and non-zinc-bound probe

as a green fluorescence can be seen during zinc binding and a blue fluorescence in the absence of zinc binding.

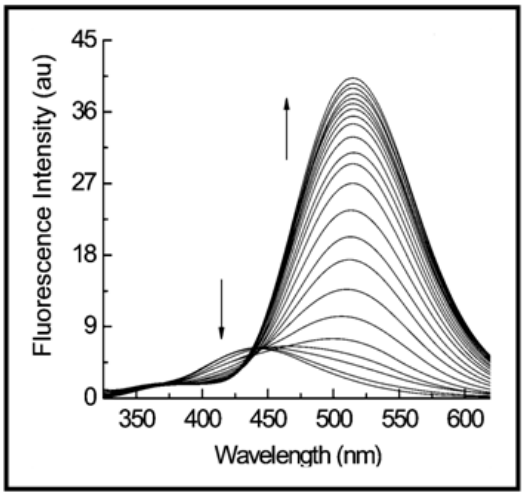

Figure 7: A graph showing the emission for AQA-OH where the fluorescence intensity increases with the addition of zinc (modified from Zhang *et al,* 2008).

AQA-OH has the potential to measure endogenous Zn^{2+} levels and therefore diagnose prostate cancer, however it is limited due to the low tissue penetration associated with fluorescence as an imaging modality. This could be overcome with the incorporation of another imaging modality, such as PET. PET would provide a higher sensitivity *in vivo* and fluorescence could be implemented on tissue samples *ex vivo*.

Dual modal zinc sensing probes have been synthesised previously. MRI/fluorescence probe based on DPA (Zhang *et al*, 2007) and AQA (Stasiuk *et al*, 2015) have been produced. While MRI provides a good tissue penetration, it is significantly less sensitive than fluorescence. However, PET is associated with high sensitivity and good tissue

penetration and would therefore act as a good corresponding imaging modality for fluorescence.

AQA-OH was previously incubated with a healthy prostate cell line (RWPE-1) and a range of studies were performed (Firth, 2016). The probe was seen to localise to the edge of the RWPE-1 cells upon internalisation. This could suggest that the probe localises within membrane bound vesicles or that it is binding metals from intracellular proteins. The chelator has been shown to bind other metals such as Ca^{2+}, Mg^{2+} and Na^{+} as Zhang *et al* (2008) suggests, however this probe produces a weak fluorescence with these other metals when compared to zinc. These previous studies have set the foundation for the work that will be completed during this project. The image from the co-localisation experiment can be seen in **Figure 8** below.

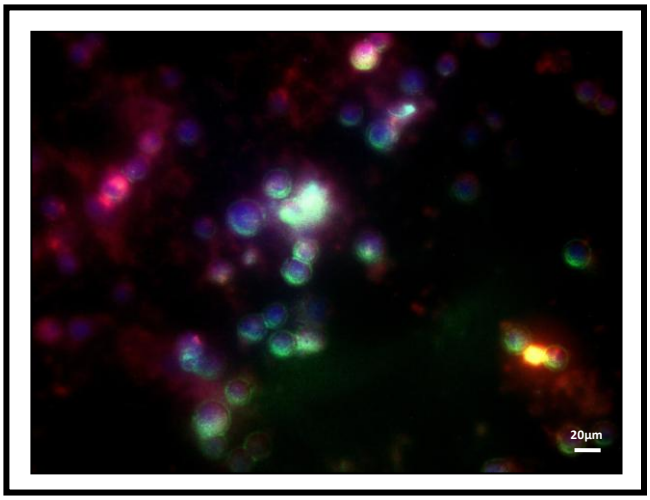

Figure 8: This image shows the results obtained from the co-localisation experiment using the zinc sensing probe on RWPE-1 cells. The red fluorescence represents Rhodamine Concanavalin A, a membrane dye, the blue fluorescence corresponds to the unbound probe and the green fluorescence highlights the probe bound to zinc (Firth, 2016).

1.5. Aims

The aim of this research project is to synthesise and validate a dual modal PET/fluorescence zinc sensing probe that can bind zinc in prostate cells. This work will further the studies performed by Dr Stasiuk and co-workers (Firth, 2016) firstly by synthesising a fluorinated analogue of the probe used in the previous experiments. This probe, termed AQA-F (**Figure 9**), contains a fluorine atom which will function as a cold analogue of the PET component of the probe. The quinoline group will represent the fluorescent component, allowing this probe to function as a dual modal diagnostic tool.

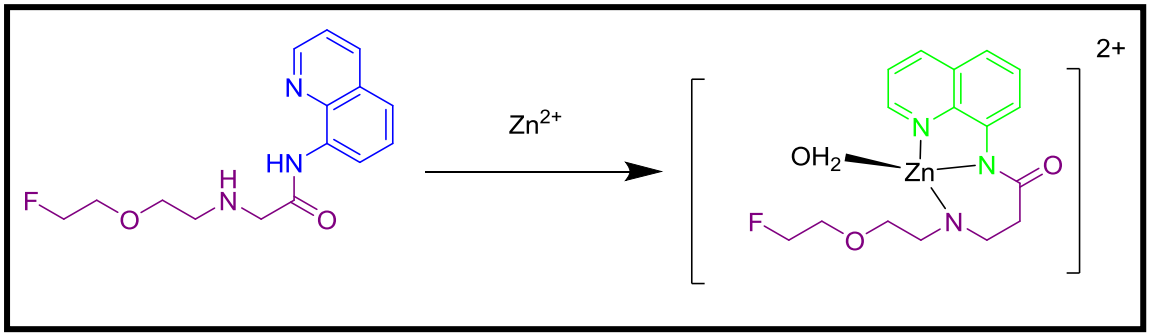

Figure 9: A diagram illustrating the proposed structure of AQF, how it binds zinc and the fluorescent colour change that is observed.

A synthetic pathway will be developed with the overall goal of producing the target probe with a reproducible yield. Previous work has shown that direct fluorination is unsuccessful (Kinnon *et al*, 2016) the proposed route involves synthesising 2-(2-fluoroethyl)ethanolamine and reacting this with the quinoline unit.

It is important that there is a fluorescence response with Zn^{2+}, this will be tested through absorbance and especially fluorescence studies. Specificity is also of

importance and will be established by testing other metals with AQA-F and determining the association constants and fluorescence response.

The non-radioactive analogue of the probe will then be investigated *in vitro* to determine if the fluorinated imaging agent is effective at being taken up by healthy prostate and prostate cancer cells with a focus on its localisation within the cell. The localization of AQA-F bound and not bound to Zn^{2+} will be investigated to understand the role of zinc in prostate cells. A 3D model will then be utilized to investigate how AQA-F behaves with a tissue-like structure.

2.0. MATERIALS AND METHOD

2.1. Chemical reagents

Solvents were purchased from VWR (Leicestershire, UK) and were either laboratory or analytical grade. Deuterated solvents were purchased from Sigma-Aldrich (Dorset, UK).

A 0.1 M stock of AQA-F was prepared which could be diluted to form the concentrations required for biological assays.

Stock A [1 mM] was made taking 50 µl of the 0.1 M drug stock and was added to 4950 µl of DDH_2O.

Stock B [0.1 mM] was made taking 50 µl of stock A and adding it to 4950 µl of DDH_2O.

Stock C [1 µM] was made taking 50 µl of stock B and adding it to 4950 µl of DDH_2O.

Krebs Hepes buffer was made using: 4.060 g NaCl (140.0 mM), 0.133 mg KCl (3.6 mM), 0.012 mg $MgSO_4$ (0.2 mM), 0.030 mg NaH_2PO_4 (0.5 mM), 0.084 g $NaHCO_3$ (2.0 mM), 1.190 g HEPES (10 mM) and is made up to 500 ml with deionised water in a 500 ml Duran bottle.

A 1mM zinc chloride ($ZnCl_2$) solution was made by adding 0.017 g $ZnCl_2$ to 125 ml of Krebs Hepes Buffer.

2.2. General methods

2.2.1. Column Chromatography

Column chromatography was performed using Merck silica gel (0.040-0.063 mm) mesh to separate the desired product from other impurities. A column was cleaned with the solvent of choice and was held in place by a clamp stand. Cotton wool was then placed at the bottom of the column followed by a layer of sand. A slurry of silica in the initial eluent is then added to the column. Two column volumes of solvent were eluted to produce a tightly packed stationary phase. A second layer of sand was then added followed by the compound dissolved in the relevant solvent. Solvent was then added and elution fractions were collected in test tubes which were later analysed using a variety of methods (UV, iodine). To increase the rate of elution, pressure was applied using a hand bellow. A diagram of the experimental set up can be seen in **Figure 10.**

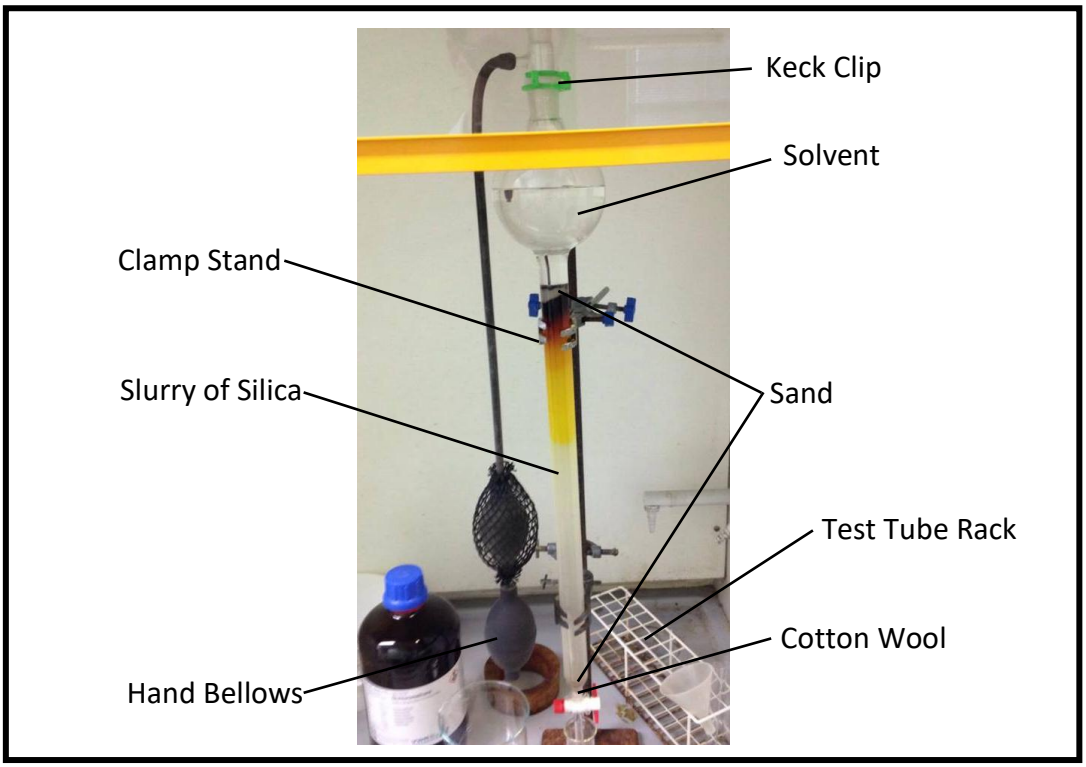

Figure 10: A diagram to highlight the experimental set up for column chromatography.

2.2.1. Spectroscopy

Nuclear magnetic resonance (NMR) spectroscopy was performed using a Jeol JNM-LA400 spectrometer at 400 MHz (^{1}H NMR), 100 MHz (^{13}C NMR) and 376 MHz (^{19}F NMR). The spectra were analysed using Mestrenova software, giving chemical shifts in parts per million (ppm) and coupling constants (*J*) in Hz. The samples were dissolved in deuterated chloroform ($CDCl_3$) and were referenced to the solvents chemical shift of 7.26 ppm.

Low resolution MS was performed using an Advion MS SOP electrospray ionisation (ESI) spectrometer using 79.5% MeOH, 20% H_2O and 0.5% formic acid as the solvent. High resolution MS was achieved using a Bruker Reflex IV MALDI-TOF MS courtesy of Dr Kevin Whelam. Infrared spectroscopy was performed using a PIKE GladiATR cell.

2.2.2. Luminescence

Luminescence results were recorded using a FluoroMax spectrometer and analysed using FluorEssence software. Samples were pipetted into a 10x10 mm quartz cuvette and a cut-off filter (typically 375 nm) was implemented to avoid second-order diffraction effects. Excitation and emission slits were 1 nm for emission spectra with a 0.1 s integration time.

Fluorescence quantum yields were determined by measuring the absorbance and emission of AQA-F at various concentrations. AQA-F was diluted until the peak absorption was <0.012, then this was plotted against the integrated fluorescence intensity and a linear regression was fitted. The gradient of this line was then entered into an equation, shown in **figure 11**, along with values obtained using quinine

sulphate in 0.1 M HEPES (ϕ = 0.50) as the reference. One equivalent of a 1 mM zinc chloride solution was added to AQA-F and the quantum yield was recorded to determine the quantum yield when the AQA-F-Zn^{2+} complex is formed.

$$\boldsymbol{\phi_x = \phi_{ST}\left(\frac{Grad_x}{Grad_{ST}}\right)\left(\frac{\eta_x^2}{\eta_{ST}^2}\right)}$$

Figure 11: Equation to calculate quantum yield where Φ is the fluorescence quantum yield, x is the sample, ST is the standard, Grad is the gradient from the plot of absorbance vs. integrated fluorescence intensity and η is the refractive index of the solvent (Laverdant *et al*, 2011).

2.2.3. pH Titrations

pH titrations were recorded using a Jenway 3520 digital pH meter with a glass electrode which was calibrated at pH 4, 7 and 10. A 0.1 mM solution of AQA-F in 0.1 M KCl was prepared and then added to a 10 mm quartz cuvette. The pH was then measured and adjusted using small aliquots of 0.1 M HCl and 0.1 M NaOH. Fluorescence emission spectra was taken at various pH with a 1 nm excitation slit width, 1 nm emission slit and 0.1 s integration time.

2.3. Probe Synthesis

*2.3.1. Synthesis: 2-chloro-N-(quinolin-8-yl)acetamide **(2)***

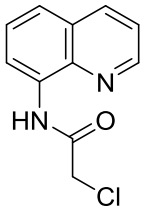

Figure 12: Chemical structure for (2).

2-chloroacetyl chloride (1.3 mL, 16.6 mmol) dissolved in chloroform (30 mL) was added dropwise to a cooled solution of 8-aminoquinoline (2.056 g, 14.3 mmol), pyridine (1.6 mL, 19.4 mmol) and chloroform (90 mL) over a period of 1 hour. After stirring for 2 hours, the solvent was removed under reduced pressure. The resulting product was dissolved in DCM (50 mL), extracted with water (3 x 50 mL) and dried over $MgSO_4$ to yield crude product as an oil. The crude product was then purified by column chromatography (silica, DCM) to yield an off white solid **(2)** (1.405 g, 6.4 mmol, 45%).

^{1}H NMR [400 MHz, $CDCl_3$, 289 K] δ: 10.91 (s, 1 H; ~N***H***~), 8.87 (dd, $^{3}J_{HH}$ = 4.2 Hz, $^{4}J_{HH}$ = 1.7 Hz, 1H; ~NHCCHCHC***H***~), 8.76 (dd, $^{3}J_{HH}$ = 6.4, 2.6 Hz, 1H; ~NCHCHC***H***~), 8.18 (dd, $^{3}J_{HH}$ = 8.3 Hz, $^{4}J_{HH}$ = 1.7 Hz, 1H; ~NHCC***H***CHCH~), 7.59 (m, 2 H; ~NHCCHC***H***CH~ ~NCHC***H***CH~), 7.49 (q, $^{3}J_{HH}$ = 4.2 Hz, 1H; ~NC***H***CHCH~), 4.32 (s, 2 H; ~NC(=O)C***H$_2$***Cl). ^{13}C NMR [100 MHz, $CDCl_3$, 289 K] δ: 164.48 (**C**=O), 148.79 (~NH***C***CHCHCH~), 136.39 (~N***C***HCHCH~), 128.05 (~NHCCH***C***HCH~), 127.27 (~NCH***C***HCH~), 122.65 (~NHCCHCH***C***H~), 121.91 (~NCHCH***C***H~), 116.74 (~NHC***C***HCHCH~), 43.45 (~***C***H_2Cl). FTIR: $\tilde{\nu}$= 3322 (NH stretch), 1668 (C=O), 1589 (NH bend), 1328 (C=N), 826 cm^{-1} (C-Cl). MS (ESI) m/z: 220.6 (75%, [*M*(^{35}Cl)+H]$^{+}$), 222.6 (25%, [*M*(^{37}Cl)+H]$^{+}$).

2.3.2. *Synthesis: 2-((2-hydroxyethoxy)ethylamino)-N-(quinolin-8-yl)acetamide* **(3)**

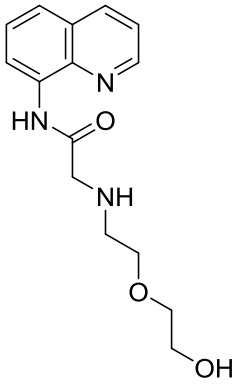

Figure 13: Chemical structure for (3).

(2) (0.498 g, 2.3 mmol), 2-(2-aminoethoxy)ethanol) (0.280 g, 2.7 mmol), DIPEA (0.346 g, 2.7 mmol) and a catalytic amount of KI were heated together under reflux in acetonitrile (18 mL). After 17 hours the mixture was cooled to room temperature and concentrated under pressure to give a dark yellow oil. Column chromatography (Silica, DCM/ 0-5% MeOH) was performed to isolate the product as a dark yellow solid **(3)** (0.495 g, 1.7 mmol, 76%).

^{1}H NMR [400 MHz, $CDCl_3$, 289 K] δ: 8.86 (dd, $^{3}J_{HH}$ = 4.2, 1.7 Hz, 1H; ~NHCC***H***CHCH~), 8.81 (dd, $^{3}J_{HH}$ = 7.0, 2.0 Hz, 1H; ~NC***H***CHCH~), 8.16 (dd, $^{3}J_{HH}$ = 8.3, 1.7 Hz, 1H; ~NHCCHC***H***CH~), 7.54 (m, 2H; ~NHCCHCHC***H***~, ~NCHCHC***H***~), 7.45 (m, 1H; ~NCHC***H***CH~), 3.74 (m, 4H; ~HNC***H*****$_2$**C***H*****$_2$**O~), 3.59 (m, 4H; ~OC***H*****$_2$**C***H*****$_2$**OH), 2.97 (t, $^{3}J_{HH}$ = 4.9 Hz, 2 H; ~NC(=O)C***H*****$_2$**NH~). ^{13}C NMR [100 MHz, $CDCl_3$, 289 K] δ: 170.57 (***C***=O), 148.66 (~NH***C***CHCHCH~), 138.99 (~NHC***C***N~), 136.42 (N***C***HCHCH), 134.23 (~NHCC***C***CH~) 128.18 (~NHCCH***C***HCH~), 127.43 (~NCH***C***HCH~), 121.96 (~NHCCHCH***C***H~), 121.67 (~NCHCH***C***H~) 116.82 (~NHC***C***HCHCH~), 72.39 (~CO***C***H_2NH~), 70.60 (~OCH_2***C***H_2OH), 61.92 (~O***C***H_2CH_2OH), 53.72 (~NHCH_2***C***H_2O~), 49.47 (NH***C***H_2CH_2O~). FTIR: $\tilde{\nu}$= 3182 (OH and NH stretch), 1678 (C=O), 1598 (NH bend), 1332 (C=N), 1123 (C=O), 1072 (C-O). MS (ESI): 289.9 $[M+H]^+$

*2.3.3. Synthesis: 1-((3-fluoropropyl)sulfonyl)-4-methylbenzene **(4)***

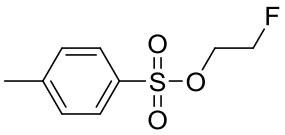

Figure 14: Chemical structure for (4).

2-fluoroethanol (1.8 mL, 31 mmol) was dissolved in chloroform (30 mL) and cooled to 0 ^{o}C, pyridine (5 mL, 62 mmol) was added followed by the addition of *p*-toluenesulfonyl chloride (6 mL, 46.5 mmol) dropwise. The reaction was stirred at 0 ^{o}C for 2.5 hours. The chloroform was removed under reduced pressure and the resulting solution was taken up in DCM (100 mL) and washed with 1 M HCl (60 mL) and then with 1 M K_2CO_3 (100 mL) and DCM (100 mL). The combined organic extracts were dried over magnesium sulfate and the solvent was removed to give a colourless oil (8.434 g). This oil was then purified by column chromatography (silica, 20% EtOAc/80% hexane) to yield a colourless oil **(10)** (5.772 g, 26.4 mmol, 85%). This was stored under inert gas in a freezer at -4 ^{o}C, forming a solid on cooling.

^{1}H NMR [400 MHz, $CDCl_3$, 289 K] δ: 7.81 (d, $^{4}J_{HH}$ = 8.3 Hz, 2H; $CH_3CCHC\boldsymbol{H}CC\boldsymbol{H}CH$~), 7.36 (d, $^{4}J_{HH}$ = 7.5 Hz, 2H, $CH_3CC\boldsymbol{H}CHCCHC\boldsymbol{H}$), 4.57 (dm, 2H; ~$OCH_2C\boldsymbol{H_2}F$~), 4.26 (dm, 2H; ~$OC\boldsymbol{H_2}CH_2F$~), 2.45 (s, 3H; $C\boldsymbol{H_3}$~). ^{13}C NMR [100 MHz, $CDCl_3$, 289 K] δ: 145.24 ($CH_3CCHCH\boldsymbol{C}SO_3$~), 132.73 ($CH_3\boldsymbol{C}CHCHCSO_3$~), 130.03 ($CH_3CCH\boldsymbol{C}HCSO_3$~), 128.08 ($CH_3C\boldsymbol{C}HCHCSO_3$~), 80.63 (d, ~$OCH_2\boldsymbol{C}H_2F$, $^{1}J_{CF}$ = 173.8 Hz), 68.53 (d, ~$O\boldsymbol{C}H_2CH_2F$, $^{2}J_{CF}$ = 21 Hz), 21.76 (~$\boldsymbol{C}H_3$). ^{19}F NMR [376 MHz, $CDCl_3$, 289 K] δ: -224.51 (tt, $^{2}J_{HF}$ = 47 Hz, $^{3}J_{HF}$ = 27 Hz). FTIR: $\tilde{\nu}$= 1458 (C-F). MS (ESI): 240.5 $[M+Na]^{+}$

*2.3.4. Synthesis: tert-butyl (2-hydroxyethyl)carbamate **(5)***

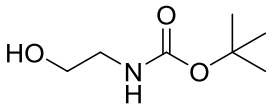

Figure 15: Chemical structure for (5).

Ethanolamine (9.9 mL, 81.9 mmol), triethylamine (27.4 mL, 98.3 mmol), di-*tert*-butyl dicarbonate (21.375 g, 98.4 mmol) in DCM (250 mL) were stirred for 12 hours. The reaction mixture was then concentrated under reduced pressure and was extracted using EtOAc (50 mL) and water (50 mL). The organic layer was collected, dried over sodium sulfate and then concentrated under reduced pressure to give a colourless oil **(12)** (10.008 g, 62 mmol, 75%).

^{1}H NMR [400 MHz, $CDCl_3$, 289 K] δ: 5.04 (s, 1 H; $OHCH_2CH_2N\boldsymbol{H}$~), 3.67 (t, 2 H; $OHCH_2C\boldsymbol{H_2}NH$~), 3.26 (d, $^{2}J_{HH}$ = 4.9 Hz, 2H; $OHC\boldsymbol{H_2}CH_2NH$~), 2.82 (s, 1H; ~O***H***), 1.44 (s, 9H; ~$OC(C\boldsymbol{H_3})_3$~). ^{13}C NMR [100 MHz, $CDCl_3$, 289 K] δ: 157.01 (***C***=O), 79.83 (~$NHCH_2\boldsymbol{C}H_2OH$), 62.92 (~$NH\boldsymbol{C}H_2CH_2OH$), 43.27 (~$O\boldsymbol{C}(CH_3)_3$), 28.45 (~$OC(\boldsymbol{C}H_3)_3$). FTIR: $\tilde{\nu}$ = 3325 (OH and NH stretch), 1689 (C=O) 1525 (N-H bending), 1071 (C-O). MS (ESI): 183.6 $[M+Na]^+$

*2.3.5. Synthesis: tert-butyl (2-(2-fluoroethoxy)ethyl)carbamate **(6)***

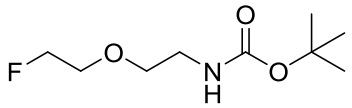

Figure 16: Chemical structure for (6).

To a solution of *tert*-butyl (2-hydroxyethyl)carbamate **(5)** (2.38 mL, 14 mmol), 1-((3-fluoropropyl)sulfonyl)-4-methylbenzene **(4)** (3.00 g, 13.3 mmol) in anhydrous DMF (30 mL), NaH (0.33 g, 13.8 mol) was added in portions. The reaction was left to stir overnight under argon. After 18 hours, the reaction mixture was diluted with EtOAc (30 mL) and water (30 mL) was slowly added. The organic phase was collected and dried using sodium sulfate. The resultant solution was then concentrated under reduced pressure to yield a crude oil, which was purified *via* column chromatography (silica, 10% EtOAc/90% hexane – 40% EtOAc/60% hexane) to yield a colourless oil **(6)** (0.602 g, 2.9 mmol, 22%).

^{1}H NMR [400 MHz, $CDCl_3$, 289 K] δ: 4.89 (s, 1H; ~N***H***~), 4.60-4.48 (m, 2H; FC***H$_2$***CH_2O~), 3.65 (m, 2H; ~OC***H$_2$***CH_2NH~), 3.56 (t, $^{3}J_{HF}$ = 5.1 Hz, 2H; FCH_2C***H$_2$***O~), 3.32 (dd, *J* = 10.5, 5.3 Hz, 2H; ~NHC***H$_2$***CH_2O~), 1.43 (s, 9H; ~OC(C***H$_3$***)$_3$). ^{13}C NMR [100 MHz, $CDCl_3$, 289 K] δ: 156.05 (***C***=O), 83.07 (d, $^{1}J_{CF}$ = 169 Hz), 79.41, 70.54, 70.18 (d, $^{2}J_{CF}$ = 19.6 Hz), 28.47 (~OC(***C***H_3)$_3$). ^{19}F NMR [376 MHz, $CDCl_3$, 289 K] δ: -222.99 (tt, $^{2}J_{HF}$ = 47.5 Hz, $^{3}J_{HF}$ = 29 Hz). FTIR: $\tilde{\nu}$= 1695 (NH scondary amide stretch), 1455 (C-F), 1168 (C-O), 1129 (C-O). MS (ESI): 229.7 [*M*+Na]$^{+}$, 245.6 [*M*+K]$^{+}$

2.3.6. Synthesis: *2-(2-fluoroethoxy)ethan-1-amine* ***(7)***

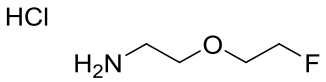

Figure 17: Chemical structure for (7).

To a solution of **6** (0.602 g, 2.9 mmol) in DCM (4 mL), TFA (4 mL) was added. After 1 hour of stirring, the reaction mixture was concentrated under reduced pressure to yield a crude oil. The crude product precipitated as an amine hydrochloride salt upon addition of 1 M solution of HCl in diethyl ether (6 mL), which was filtered and obtained as a white powder (0.397 g, 95%).

^{1}H NMR [400 MHz, $CDCl_3$, 289 K] δ: 8.38 (s, 2H; N***H₂***~), 4.72 – 4.49 (m, 2H; ~OCH_2C***H₂***F), 3.90 – 3.72 (m, 4H; NH_2CH_2C***H₂***O***H₂***~), 3.23 (t, 2H; NH_2C***H₂***CH_2O~). ^{13}C NMR [100 MHz, $CDCl_3$, 289 K] δ: 77.42, 77.30, 76.93, 76.78. ^{19}F NMR [376 MHz, $CDCl_3$, 289 K] δ: -222.71, (tt, $^{2}J_{HF}$ = 47.7 Hz, $^{3}J_{HF}$ = 30.3 Hz). FTIR: $\tilde{\nu}$= 2890 (N-H salt stretch), 1456 (C-F), 1120 (C-O). MS (ESI): 108.2 [*M*+H]$^{+}$

2.3.7. Synthesis: *2-((2-(2-fluoroethoxy)ethyl)amino)-N-(quinolin-8-yl)acetamide* ***(8)***

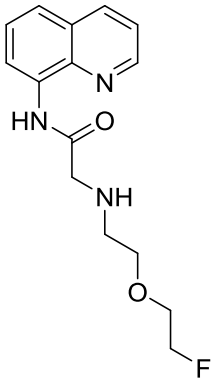

Figure 18: Chemical structure for (8).

(7) (0.350 g, 2.4 mmol), **(2)** (0.108 g, 0.5 mmol), DIPEA (1.28 mL, 7.32 mmol) and a catalytic amount of KI were heated together under reflux in acetonitrile (30 mL). After 18 hours, the reaction was cooled to room temperature and concentrated under reduced pressure to yield an orange oil (0.9805 g). The crude product was purified *via* column chromatography (silica, DCM/1% MeOH) to yield an orange oil (0.123 g, 87%).

^{1}H NMR [400 MHz, $CDCl_3$, 289K] δ: 11.39 (s, 1H), 8.85 (dd, *J* = 4.2, 1.7 Hz, 1H; ~NHCC***H***CHCH~), 8.82 (dd, *J* = 7.0, 1.9 Hz, 1H; ~NC***H***CHCH~), 8.16 (dd, *J* = 8.3, 1.7 Hz, 1H; ~NHCCHC***H***CH~), 7.58 – 7.50 (m, 2H, ~NHCCHCHC***H***~, ~NCHCHC***H***~), 7.44 (s, 1H; ~NCHC***H***CH~), 4.65 – 4.50 (m, 2H; ~OCH_2C***H_2***F), 3.81 – 3.78 (t, 1H;), 3.78 – 3.75 (t, 2H;), 3.73-3.71 (t, 1H;) 3.58 (s, 2H;), 2.98 – 2.95 (m, 2H; ~C***H_2***NH~). ^{13}C NMR [100 MHz, $CDCl_3$, 289 K] δ: 170.46 (***C***=O), 148.60 (~NH***C***CHCHCH~), 139.07 (~NHC***C***N~), 136.33 (N***C***HCHCH), 134.36 (~NHCC***C***CH~), 128.16 (~NHCCH***C***HCH~), 127.42 (~NCH***C***HCH~), 121.85 (~NHCCHCH***C***H~), 121.64 (~NCHCH***C***H~), 116.66 (~NHC***C***HCHCH~), 72.66 (~CO***C***H_2NH~), 70.80 (~OCH_2***C***H_2F), 61.58 (~O***C***H_2CH_2F), 53.54 (~$NHCH_2$***C***H_2O~), 49.43 (NH***C***H_2CH_2O~).^{19}F NMR [376 MHz, $CDCl_3$, 289 K] δ: -222.75 (tt, , $^{2}J_{HF}$ = 47.7, $^{3}J_{HF}$ = 29.7

Hz). FTIR: $\tilde{\nu}$= 1683 (C=O), 1324 (aromatic amine stretch), 1595 (N-H bending), 1456 (C-F), 1126 (C-O). MS (ESI): 292.1 $[M+H]^+$, 314.2 $[M+Na]^+$

2.4. Tissue Culture

2.4.1. Use of the Class II Biosafety Hood

All biological procedures were performed in a biological safety cabinet to minimise contamination, with the operator's gloved hands being sprayed with 70% ethanol before entering the safety hood. Any equipment, reagents and objects were also sprayed with 70% ethanol to sterilise them A waste pot containing 2% Virkon solution was used to dispose hazardous material.

The class II biological safety hood was turned on when the sash was raised to the slide marker and the fan was turned on. The fan then warmed up over 3 minutes allowing for adequate air filtration. The surfaces inside were cleaned before use from the back of the hood to the front using 70% ethanol, blue roll and a disinfectant cleaner, such as trigene.

Once the experimental procedure was finished, all equipment and waste were removed and disposed of prior to the cleaning process. The biosafety hood was then cleaned once more, the window was lowered to the arm rest and the UV light was turned on.

2.4.2. Use of the Bench Top Autoclave

An autoclave was used to sterilise equipment such as pipette tips and forceps for experimental use. The lid from the empty autoclave was removed and the autoclave

was filled to the indicated line with distilled water. The objects that required sterilising were then wrapped in tin foil with the ends sealed using autoclave tape and were placed into the autoclave. The lid was placed back on and the autoclave was turned on. After 40 minutes, the objects were removed and were ready for use. Autoclave tape was used as this turns from green to black after sterilisation.

2.4.3. Cell Lines and Cell Culture

The human embryonic kidney cells (HEK293), RWPE-1, RWPE-2 and PC-3 cells were purchased from ATCC. The HEK293 and PC-3 cells were cultured using Dulbecco's modified Eagle Medium (DMEM) (500 ml) (Lonza) supplemented with 50 ml 10% Fetal Bovine Serum (FBS) (Lonza) and 5 ml 1% PenStrep (P/S) (Lonza). The RWPE-1 and RWPE-2 cells were grown in Keratinocyte Serum Free Medium (K-SFM) (Fisher) supplemented with 25 mg bovine pituitary extract (BPE) (Fisher) and 2.5 μg human recombinant epidermal growth factor (EGF) (Fisher). All of these cell types were grown in T75 culture flasks and were incubated at 37^{O}C 5% CO_2.

2.4.4. Preparing the growth medium

The media (500 ml) and associated supplements were heated to 37^{O}C using a water bath. These, along with syringes and filters, were sprayed into the class II biosafety hood. A 20ml syringe and filter was then used to filter the supplements into the media bottle. Any empty containers and equipment were disposed of appropriately and the media was labelled and placed in the fridge at 4^{O}C until required.

2.4.5. Subcultivating Cells

The relevant media and trypsin (with 0.05% EDTA) was heated to 37 ^{o}C using a water bath. The confluency of the cells was examined under a light microscope as the cells must be subcultured once they reach 80% confluency. Once transferred in to the biosafety hood, the old media present in the flasks was disposed into Virkon using a 25 ml pipette. The T-75 flask containing cells was then washed twice with 5 ml phosphate-buffered saline (PBS) and 3 ml of trypsin (with EDTA) was added. The T-75 flask was then placed into an incubator at 37 ^{o}C 5% CO_2 for 5-10 minutes or until the cells had detached from the base of the flask. After incubation, 3 ml of the corresponding media was added to inhibit further action of trypsin and the contents of the flask were centrifuged at 1500 rpm 20 ^{o}C for 3 minutes in a 50 ml falcon tube. The media was then removed without disturbing the pellet and the pellet was re-suspended in media. Once the cells were re-suspended, 1 ml of this was added to a T-75 culture flask containing 17 ml of the corresponding media. The flask was then verified for the presence of cells using a light microscope before being placed into the incubator at 37 ^{o}C 5% CO_2 until confluent or required for assays. Each cell line was subcultured depending on growth efficiency, therefore different subcultivation ratios were applied (consult **Table 4** below).

Table 4: The optimal subcultivation ratios and typical incubation times for each cell line.

Cell Line	Subcultivation ratio (cell suspension : media)	Incubation Times (days)
RWPE-1	1:6	3-4
RWPE-2	1:5	4
PC-3	1:4	5
HEK293 (Control)	1:4	5

2.4.6. Counting Cells

A haemocytometer was cleaned using 70% ethanol and blue roll. A cover slip was then heated up by exhaling on to it and was placed on to the haemocytometer chamber. 10 µl of cell suspension was added to 10 µl of 0.2% Trypan blue in an Eppendorf tube. 10 µl of the solution was then placed underneath the cover slip using a Gilson pipette. The prepared haemocytometer was then placed under a light microscope at x20 magnification and all of the cells present in each of the four corners were counted (16 squares per corner). An average of the viable cells was then determined by adding up all of the four corner counts and dividing by 4. This figure was then multiplied by two to account for the Trypan blue dilution factor thus giving a value of cells $x10^4$/ml. This value was then used to determine the dilution required to achieve a certain number of cells for an experiment. The cell suspension was diluted 1 ml at a time to produce a sample that was small enough to count. The layout of a haemocytometer chamber is shown in **Figure 19**.

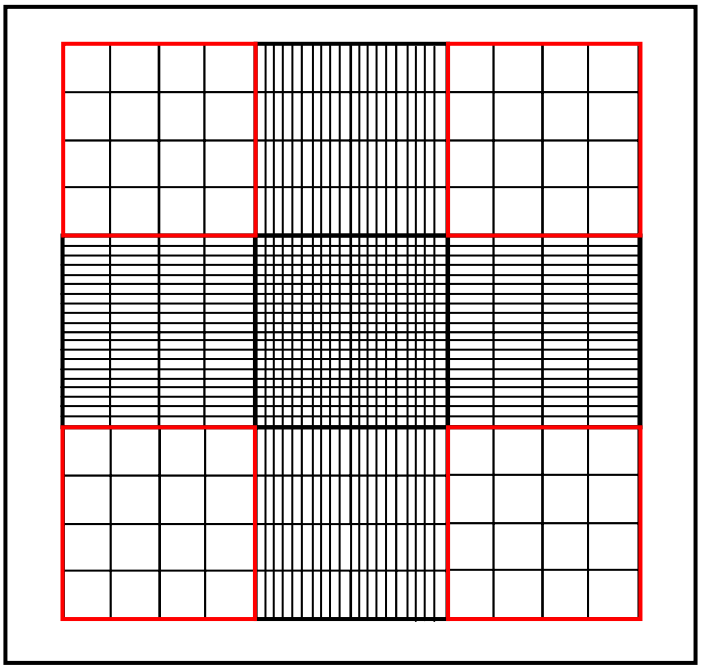

Figure 19: This illustration depicts the layout of a haemocytometer chamber. All the cells found in all four corners are counted. A dilution is then determined to dilute a cell suspension to achieve a specific number of cells /ml.

2.4.7. Freezing Cells

Cells that need preserving are subcultured as normal following the protocol described in *chapter 2.4.5*. However once the pellet was formed 10 ml of freezing media (9 ml FBS and 1 ml DMSO) was added and the pellet was re-suspended using a pipette. 1 ml of this solution was then added into each of the cryogenic vials. These cryogenic vials were then placed in the freezing container containing isopropanol at -80 °C. After a week, these could then be transferred to the large storage units containing liquid nitrogen at -196 °C.

2.5. *In Vitro* Validation

2.5.1. MTS Assay

Firstly, the class II biosafety hood was set up according to the protocol discussed in *chapter 2.4.1.* The cells were then subcultured and counted (as seen in *chapter 2.4.5.* and *2.4.6.*) in order to be diluted to achieve 105,000 cells/ml. 190 µl of the cell suspension was then added, as well as 190 µl of PBS, to three 96 well flat bottomed plates distributed according to **Figure 20**. These plates were then placed in the incubator at 37 ^{o}C 5% CO_2 for 24 hours to allow the cells to settle to the base of the wells.

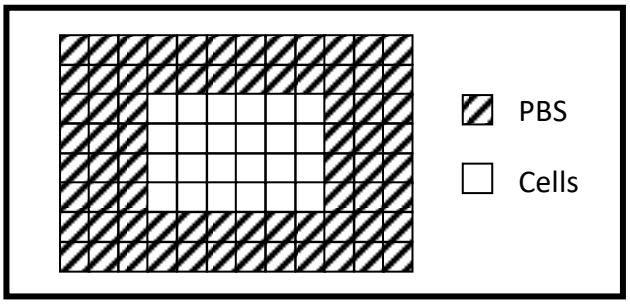

Figure 20: Experimental layout of the 96 well plates when performing an MTS assay.

Following the incubation period, the media was removed and the corresponding treatments were applied. The treatment schedule is shown in **table 5**. After the treatments were added under sterile conditions, the plates were then placed back in to the incubator for a further 24 hours.

A falcon tube containing an MTS solution was defrosted at 37 ^{o}C in the water bath 1 hour before it was required. After the 24 hour incubation period, the plates were removed and placed into the biosafety cabinet. All of the solution (media and probe) was removed from the wells and 180 µl of PBS was added. 20 µl of MTS was then added directly to all the wells and the plates were then incubated at 37 ^{o}C for 2 hours. Following this, the plates were recorded by a BIO-TEK Synergy HT plate reader at 490 nm giving the data in a maximum optical density (MAX OD) form.

Table 5: Different treatments that were applied to each MTS plate. The concentrations were: Stock A [0.1 M], Stock B [10 mM] and Stock C [10 µM].

STOCK A [0.1 M]					
1	**2**	**3**	**4**	**5**	**6**
100 µl Stock A	50 µl Stock A	25 µl Stock A	10 µl Stock A	5 µl Stock A	2 µl Stock A
100 µl Media	150 µl Media	175 µl Media	190 µl Media	195 µl Media	198 µl Media
50 mM	**25 mM**	**12.5 mM**	**6.25 mM**	**3.125 mM**	**1.5625 mM**
STOCK B [10 mM]					
100 µl Stock B	50 µl Stock B	25 µl Stock B	10 µl Stock B	5 µl Stock B	2 µl Stock B
100 µl Media	150 µl Media	175 µl Media	190 µl Media	195 µl Media	198 µl Media
5 mM	**2.5 mM**	**1.25 mM**	**0.625 mM**	**0.3125 mM**	**0.15625 mM**
STOCK C [10 µM]					
100 µl Stock C	50 µl Stock C	25 µl Stock C	10 µl Stock C	5 µl Stock C	2 µl Stock C
100 µl Media	150 µl Media	175 µl Media	190 µl Media	195 µl Media	198 µl Media
0.05 mM	**0.025 mM**	**0.0125 mM**	**0.00625 mM**	**0.003125 mM**	**0.0015625 mM**
CONTROL					
No Stock	No Stock	100 µl Stock B	100 µl Stock B	No cells	No cells
			No Media	No stock	No stock
200 µl Media	200 µl Media	No Media		200 µl Media	200 µl Media
0 mM	**0 mM**	**10mM**	**10mM**	**0 mM**	**0 mM**

2.5.2. Dose Response Fluorescence

A dose response fluorescence experiment was performed to determine the optimal concentration of probe to incubate with during fluorescence experiments. RWPE-1 cells were grown to allow $1x10^5$ cells/ml for each well and were counted and split according to *chapter 2.4.5.* and *2.4.6*. The 24-well poly-lysine coated plates were seeded with $2x10^4$ cells per well and were incubated at 37 ^oC 5% CO_2 overnight. After incubation, the media was removed from all of the wells using a Gilson pipette and each well was washed twice with 200 μl PBS. The probe was then added along with Krebs buffer to create set concentrations in each well (see **Table 6**). The plate was then placed into the incubator for 30 minutes. After this time, the plate was placed back into the hood and the probe/buffer was removed using a pipette. The wells were then washed twice with 200 μl PBS and were fixed using 200 μl of 4% paraformaldehyde (PFA). After 10 minutes, the PFA was removed and the cells were washed once again with 200 μl PBS. The fixed cells were then stored in 200 μl PBS in the fridge until they were required for imaging on the high throughput fluorescence microscope.

All fluorescence imaging was viewed using an ImageXpress Micro 4 high throughput fluorescence microscope. Micrographs were then produced using the MetaXpress imaging software, were analysed using MetaXpress and ImageJ software and were plotted using the GraphPad Prism 6.0 software.

Table 6: Contents of each well for the dose fluorescence experiment. AQA-F was pipetted from a 1mM stock concentration.

	1	2	3	4	5	6	7	8
A		Cell Control 100 µl Krebs Buffer				1 µl AQA-F 99 µl Krebs Buffer		
B		2 µl AQA-F 100 µl Krebs Buffer				5 µl AQA-F 95 µl Krebs Buffer		
C		10 µl AQA-F 90 µl Krebs Buffer				20 µl AQA-F 80 µl Krebs Buffer		
D		30 µl AQA-F 70 µl Krebs Buffer				40 µl AQA-F 60 µl Krebs Buffer		
E		50 µl AQA-F 50 µl Krebs Buffer				60 µl AQA-F 40 µl Krebs Buffer		
F		70 µl AQA-F 30 µl Krebs Buffer				80 µl AQA-F 20 µl Krebs Buffer		
G		90 µl AQA-F 10 µl Krebs Buffer				100 µl AQA-F		
H		250 µl AQA-F						

2.5.3. Time Response Fluorescence

A time response fluorescence experiment was performed to determine the optimum incubation time to apply the probe for. The protocol was similar to that described in *chapter 2.5.2.* however the amount of time that AQA-F was applied for differed with a concentration at 100 μM. The cells were incubated overnight at 37 ^{o}C 5% CO_2 until the cells had adhered to the base of the 96 well plate. AQA-F was incubated with cells for 0-500 minutes according to **Table 7**. After the final addition, all of the solution was removed from each well, whereby they were washed twice with 200 μl PBS. After the cells were fixed using 200 μl of 4% PFA, the cells were then viewed using the high throughput fluorescence microscope.

Table 7: Incubation times of AQA-F (100 μM) used for each well during the time response fluorescence experiment.

	1	2	3	4	5	6	7	8	9	10	11	12
A	0 min				5 min				10 min			
B	15 min				20 min				30 min			
C	40 min				50 min				60 min			
D	75 min				90 min				105 min			
E	120 min				180 min				300 min			
F	500 min											

2.5.4. Co-localisation

A co-localisation experiment was performed to determine the intracellular location of AQA-F. Commercial dyes such as Rhodamine Concanavalin A (cell membrane stain), Lysotracker red (lysosomal stain) and Mitotracker red (mitochondrial stain) were implemented as the sites where they accumulate were known. This information could then be used to determine the location of the probe once it was incorporated into the cell. The 96 well plate was seeded following the protocol from *2.5.3*. however 6 wells were also incubated with 20 µl of a zinc chloride solution (1 mM) overnight. A different combination of dyes was applied to each well which are conveyed in **Table 8**.

Table 8: The combination of dyes used in each well during the 2D co-localisation experiment.

	1	2	3	4	5	6	7	8	9	10	11	12
A	Control						Probe					
B	Rhodamine Concanavalin A						Mitotracker Red					
C	Lysotracker Red						Probe + Rhodamine Concanavalin A					
D	Probe + Mitotracker Red						Probe + Lysotracker Red					
E	Control + Zn^{2+}						Probe + Zn^{2+}					
F	Rhodamine Concanavalin A + Zn^{2+}						Mitotracker Red + Zn^{2+}					
G	Lysotracker Red + Zn^{2+}						Probe + Rhodamine Concanavalin A + Zn^{2+}					
H	Probe + Mitotracker Red + Zn^{2+}						Probe + Lysotracker Red + Zn^{2+}					

2.5.5. 3D Cell Models

Basement membrane (BM) matrix was thawed by incubating at 4 ^{o}C on ice for 16 hours. 96-well plates were placed on top of ice to maintain a temperature of 4 ^{o}C during the coating procedure. The dispensing end of a pipette was then cut off, cooled to 4 ^{o}C and used to coat the wells with 20 μl of BM matrix, taking care to avoid pipetting air in to the gel. The plates were then incubated at 37 ^{o}C for 30 minutes to promote polymerisation of the BM matrix. Following the incubation period, the wells were washed twice with 200 μl of PBS and were seeded with RWPE-1 and PC-3 cells at a density of $2x10^{3}$. The media for the cells was supplemented with 2% BM matrix and was changed every two days during acini growth. Images were taken using a brightfield microscope each day to record acini growth. After 6 days, the cells were washed and stained using a variety of dyes (dye combinations seen in **Table 9**) as described in *section 2.5.4.* Fluorescence images were then taken using the high throughput fluorescence microscope and the confocal microscope.

Table 9: The combination of dyes used in each well during the 3D co-localisation experiment.

	1	2	3	4	5	6
Native rBM	Control	Probe	CONO	DAPI	Probe + CONO	Probe + DAPI
Native rBM	Control + Zn^{2+}	Probe + Zn^{2+}	CONO + Zn^{2+}	DAPI + Zn^{2+}	Probe + CONO + Zn^{2+}	Probe + DAPI + Zn^{2+}
Stiff rBM	Control	Probe	CONO	DAPI	Probe + CONO	Probe + DAPI
Stiff rBM	Control + Zn^{2+}	Probe + Zn^{2+}	CONO + Zn^{2+}	DAPI + Zn^{2+}	Probe + CONO + Zn^{2+}	Probe + DAPI + Zn^{2+}

3.0. RESULTS AND DISCUSSION

3.1. Probe Synthesis

AQA-F (**8**) provides the motifs for both Zn coordination through the amidoquinoline unit and a terminal fluorine for future radiolabelling for PET imaging. Previous attempts to synthesise **8** by substitution of the terminal alcohol in **3** (**Figure 21**) have proved unsuccessful (Kinnon *et al*, 2016). Stasiuk *et al.* 2015 suggests that the basic conditions required for the substitution reaction results in intramolecular cyclisation. Herein, we propose the synthesis of the chain **7**, as reported by Bernard-Gauthier *et al.* 2015, which will then be used to form **8** directly from **2** (**Figure 22**).

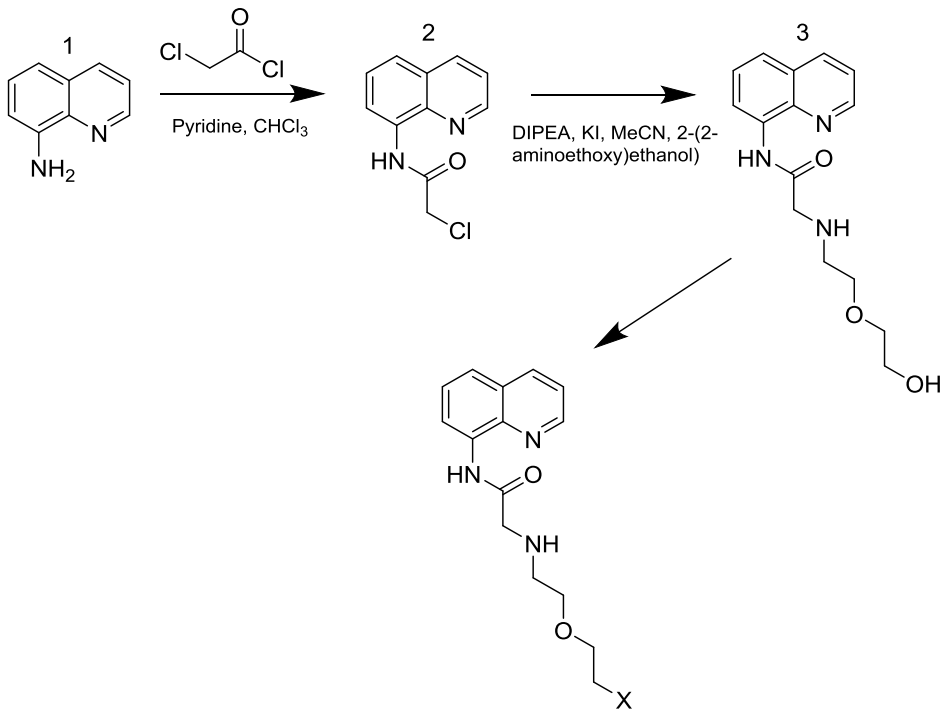

Figure 21: A schematic representing the proposed synthetic pathway used to produce the target probe, where X is chlorine, fluorine or mesyl.

This method of synthesis (**Figure 22**) involved generating the fluorinated side chain first by reacting Boc protected ethanolamine with tosylated 2-fluoroethanol. After deprotection, this side chain was then reacted with **2** to yield **8**. This synthesis route may not be practical for radiochemistry but does provide the pathway to a cold analogue for *in vitro* analysis.

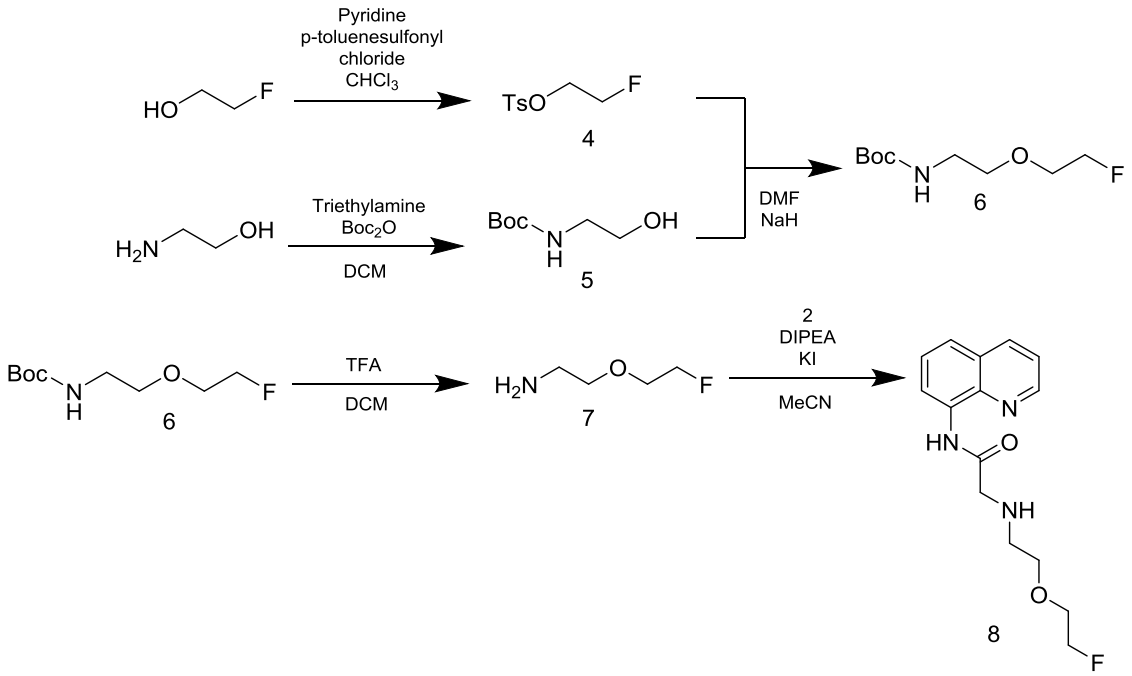

Figure 22: A schematic representing the modified synthetic pathway used to produce the target probe.

*3.1.1. Synthesis: 2-chloro-N-(quinolin-8-yl)acetamide **(2)***

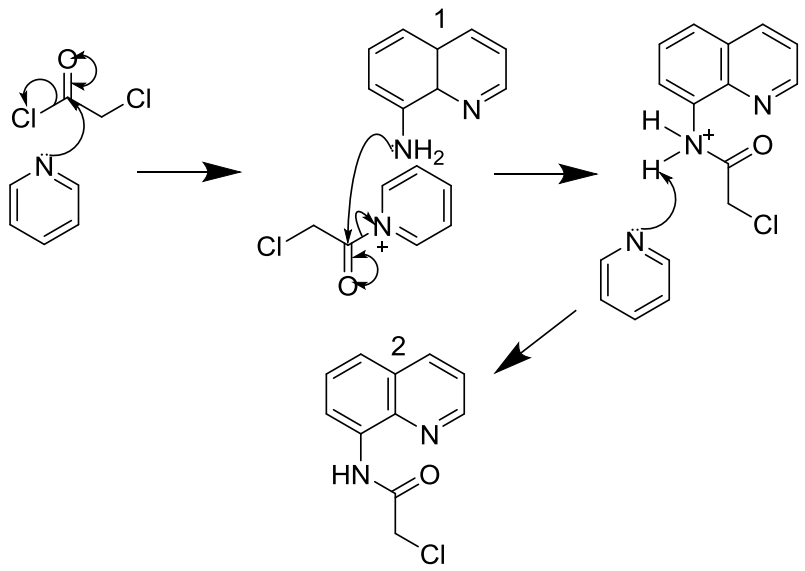

Figure 23: Proposed reaction mechanism for the synthesis of (2) from (1).

The synthesis of **2** involved a nucleophilic substitution (S_N2) reaction where the lone pair of the amine of pyridine attacks the δ+ carbon of the carbonyl group of chloroacetyl chloride. A lone pair from the amine of 8-aminoquinoline then attacks this pyridinium intermediate to yield the protonated amine intermediate. Pyridine then acts as a base to remove a proton to yield **2**. The yield for this reaction was 45% which was lower than expected when compared with the yield obtained by Stasiuk *et al,* 2015, however sufficient material was produced for all future work.

The product was confirmed by mass spectrometry (MS) showing the isotopic pattern for chlorine. The peak at m/z 220.6 represents $[M+H]^+$ with the Cl isotope at mass 35 whereas 222.6 corresponds to Cl with a mass of 37. This is also further confirmed by the intensity of the two peaks, with a ratio of 3:1 which reflects the abundance of both isotopes. Further analysis was undertaken utilising ^1H nuclear magnetic resonance

(NMR) (**Figure 24**). The data was consistent with that found in Stasiuk *et al,* 2015 excluding minor solvent peaks. The peak at 4.25 which integrates to 2 protons corresponds to the CH_2 group of the acetyl chloride, whereas the highlighted peaks found between 7-9 ppm correspond to the 6 protons found on the aromatic ring. The peak found at around 11 ppm may correspond to the amine found on **2**. The IR spectra of **2** shows a sharp absorbance peak at 1589 cm^{-1} corresponding to the newly formed amide bond.

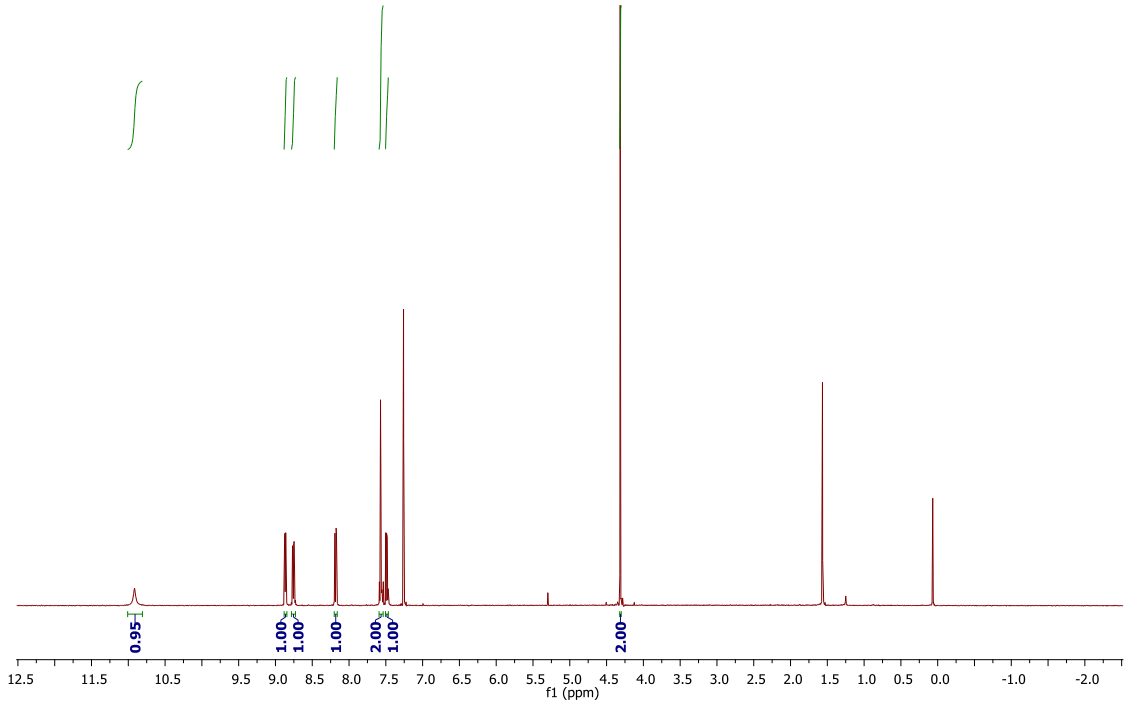

Figure 24: ^{1}H NMR spectra for compound 2.

*3.1.2. Synthesis: 2-((2-hydroxyethoxy)ethylamino)-N-(quinolin-8-yl)acetamide **(3)***

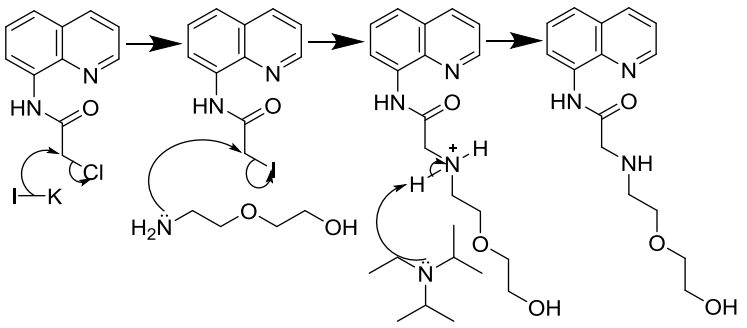

Figure 25: Reaction mechanism for (3).

The synthesis of **3** first involved a halogen exchange with potassium iodide (KI). The iodide anion acts as a better leaving group than the chloride anion. The lone pair of the amine of 2-(2-aminoethoxy)ethanol attacks the secondary carbon of the intermediate in an S_N2 reaction. N-N-diisopropylethylamine (DIPEA) then deprotonates the quaternary amine cation to yield **3** as reported by Stasiuk *et al*, 2015.

MS highlighted peaks at m/z 289.2 $[M+H]^+$ and 311.6 $[M+Na]^+$ which both could correspond to **3**. The peak at m/z 129.8 matches that of DIPEA which was later removed *via* column chromatography. Post-column chromatography NMR peaks (**Figure 26**) correspond to those published by Stasiuk *et al*, 2015.

The aromatic and amine protons found between 7-12 ppm have remained similar compared to **2**. Some additional peaks found between 3.5-4 ppm integrate to a total of 8 protons corresponding to the four CH_2 groups of the chain. The 2 protons seen at around 4.3 ppm in **2** have shifted slightly to around 3 ppm in **3**.

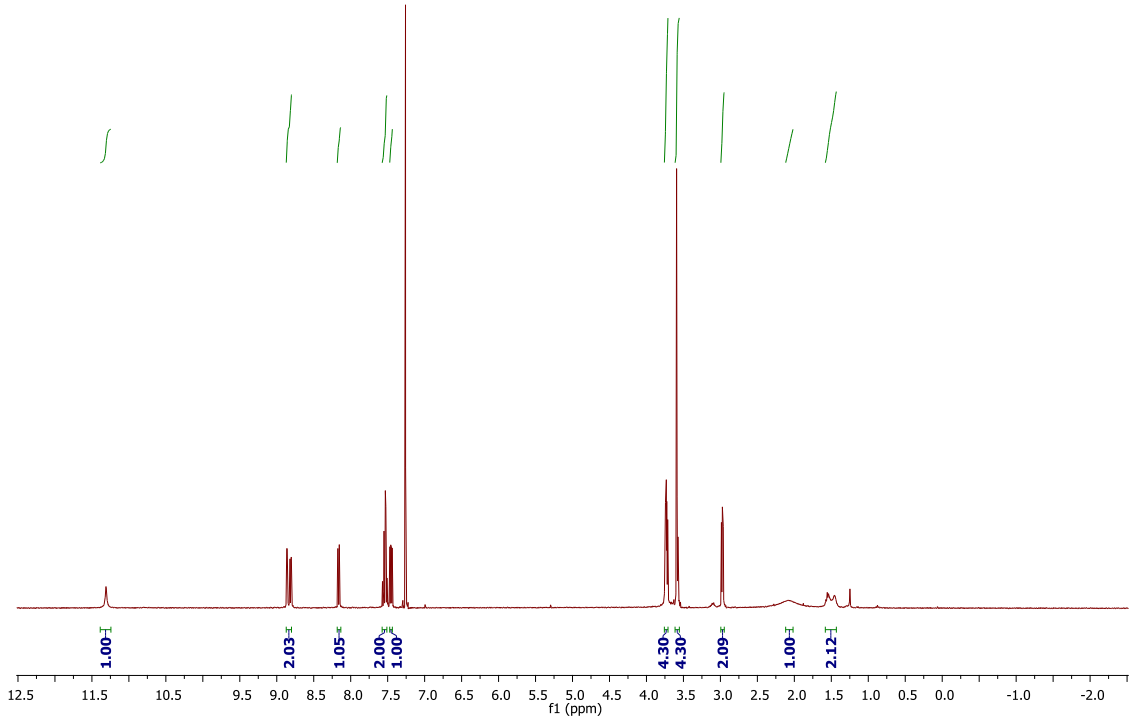

Figure 26: ^{1}H NMR spectra for compound **3**.

Whilst these preliminary steps were successful, as discussed in S*ection 3.1*, this synthetic route to a fluorinated compound (AQA-F) is not practical, so a new synthetic route to **8** was developed (**Figure 22**).

*3.1.3. Synthesis: 1-((3-fluoropropyl)sulfonyl)-4-methylbenzene **(4)***

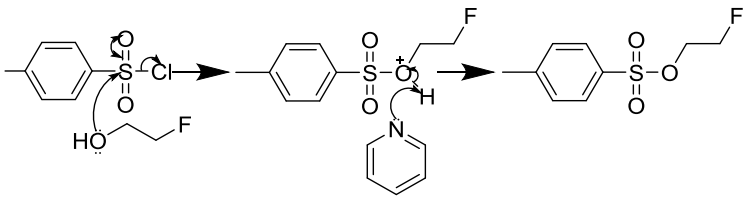

Figure 27: Reaction mechanism for (4).

The synthesis of **4** involved a S_N2 reaction where the lone pair on the oxygen attacks the electrophillic centre, the sulphur, of *p*-toluenesulfonyl chloride displacing the chloride ion. Pyridine then deprotonated the oxygen to yield **4** (85%) as outlined by Kabalka *et al*, 1986. The goal of this reaction was to increase the reactivity of the starting material. This was required as alcohols are poor leaving groups for substitution reactions so a tosyl group was utilised instead.

MS showed the m/z peak for $[M+Na]^+$ at 240.5 and the NMR data (**Figure 28**) was consistent with that reported in Kabalka *et al,* 1986 excluding minor solvent peaks. A singlet peak seen at 2.5 ppm with an integration of 3 corresponds to the CH_3 of **4**. Two peaks with a total integration of 4 seen in the aromatic region correspond to the 4 protons on the benzene ring. A doublet of triplets seen at 4.5 ppm corresponds to the CH_2 next to the fluorine. These two protons have a greater chemical shift compared to the other doublet of triplets seen at 4.25 ppm as fluorine is more electronegative than oxygen.

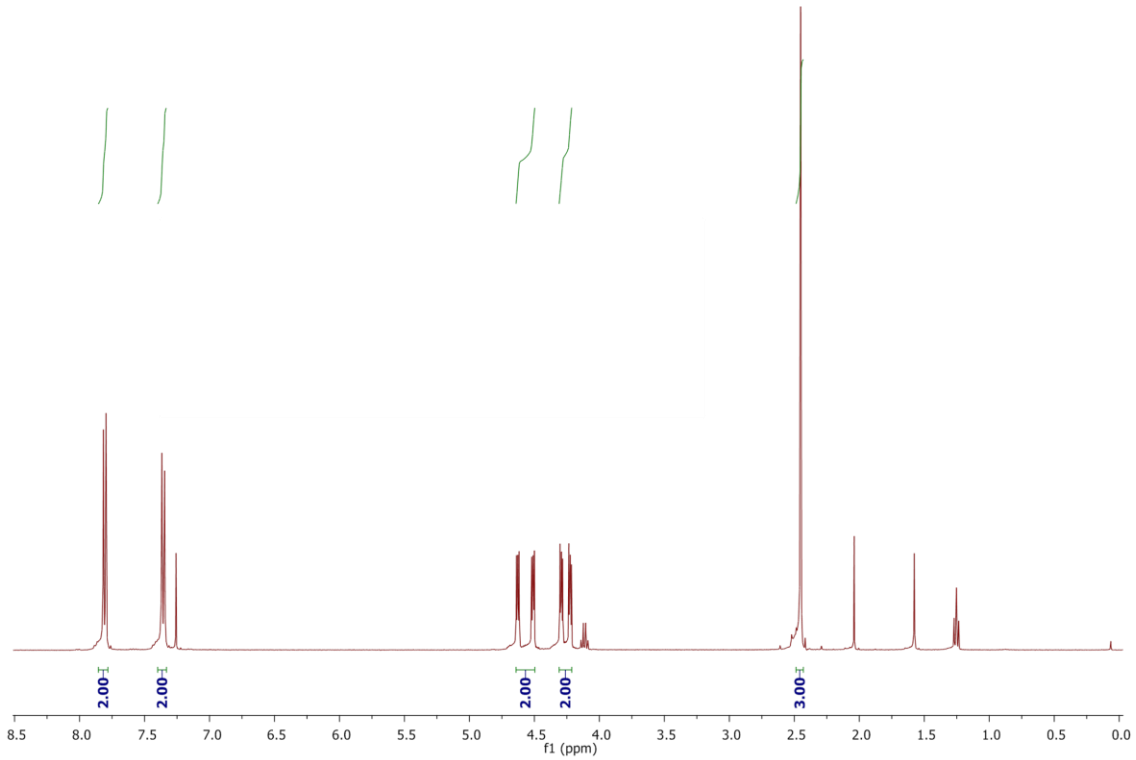

Figure 28: ^{1}H NMR spectra for compound **4**.

*3.1.4. Synthesis: tert-butyl (2-hydroxyethyl)carbamate **(5)***

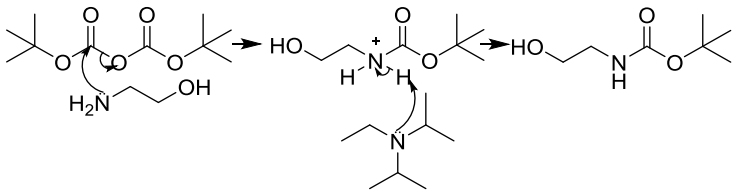

Figure 29: Reaction mechanism for (5).

The synthesis of **5** involved an S_N2 reaction whereby the lone pair on the primary amine attacks the carbon of the acetyl group on di-*tert*-butyl dicarbonate (Boc_2O). DIPEA, acting as a base, then deprotonates the quaternary amine to yield **5** as outlined in Debaene *et al*, 2007. The amine protecting group Boc was applied for the future side chain reaction. This was necessary to control how the following reaction would take place as the lone pair of the amine could also react. The protecting group pushes the reaction to favour the lone pair of the oxygen attacking **4** as desired. This reaction was executed in an open system as carbon dioxide is formed as a by-product.

Spectroscopy data was consistent with that reported in Debaene *et al,* 2007. NMR (**Figure 30**) highlighted a large singlet peak at 1.42 ppm with an integration of 9 corresponding to the 9 protons associated with the Boc protecting group. This is promising as it suggests compound **5** has been successfully protected.

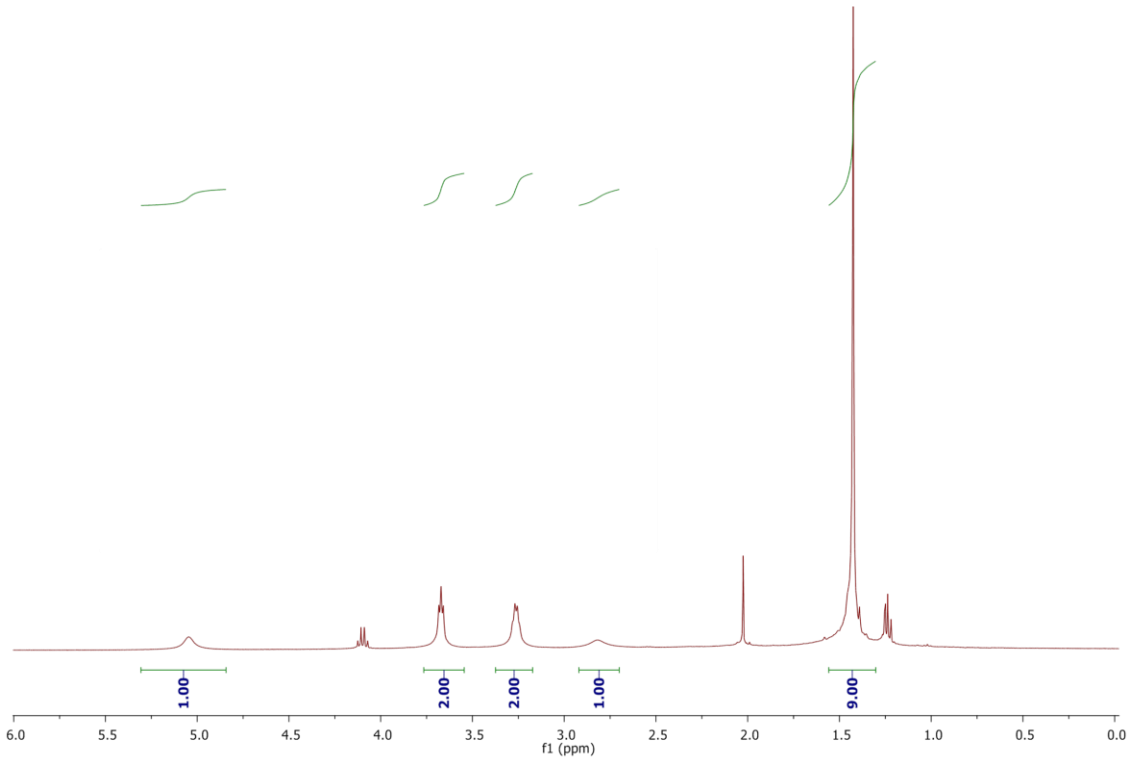

Figure 30: ^{1}H NMR spectra for compound **5**.

*3.1.5. Synthesis: tert-butyl (2-(2-fluoroethoxy)ethyl)carbamate **(6)***

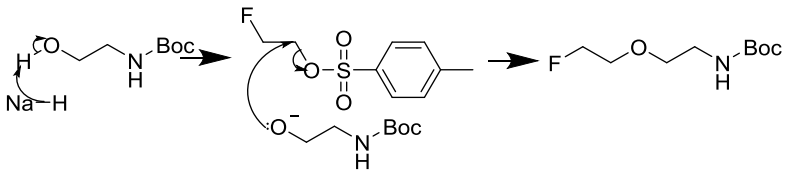

Figure 31: Reaction mechanism for (6).

The synthesis of **6** involved a coupling reaction with compounds **4** and **5** . This reaction was taken from Bernard-Gauthier *et al*, 2015. NaH was chosen as a base during this reaction instead of other bases such as pyridine due to it being a better nucleophile with O^-. Weaker bases such as pyridine (pK_a = 5.2) would not deprotonate the alcohol group (pK_a = 9.4) as readily as NaH (pK_a = 35) therefore NaH was utilised. This reaction is highly moisture sensitive and a number of side products (such as BocNHCCOCCNHBoc and FCCOCCF) could be formed. A low yield of 22% was obtained in comparison to reported yields (54%), likely due to the aforementioned moisture sensitivity. Possible evidence for the formation of BocNHCCOCCNHBoc was seen through MS (m/z = 157) however this was readily removed through column chromatography.

MS highlighted a peak at m/z 229.8 corresponding to $[M+Na]^+$. The NMR spectrum (**Figure 32**) agrees well with that reported by Bernard-Gauthier *et al,* 2015, with additional peaks between 3-5 ppm compared to **5**. These alkyl protons have a greater chemical shift due to being situated next to electronegative groups such as F and N.

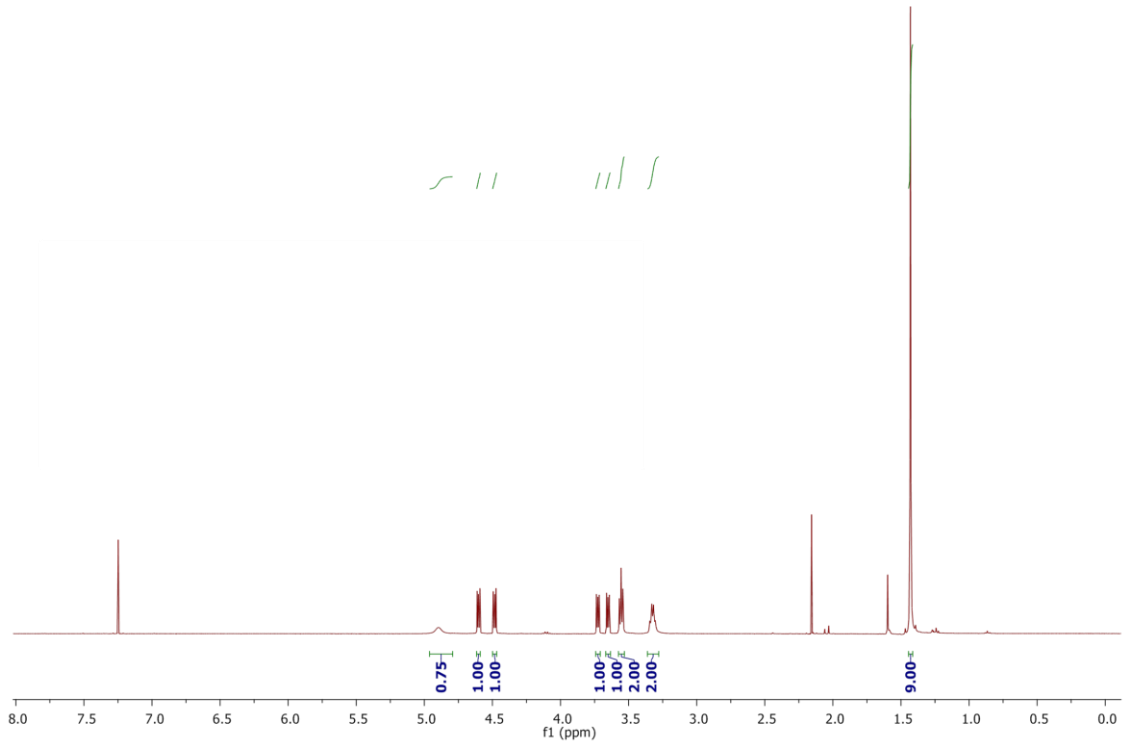

Figure 32: ^{1}H NMR spectra for compound **6**.

*3.1.6. Synthesis: 2-(2-fluoroethoxy)ethan-1-amine **(7)***

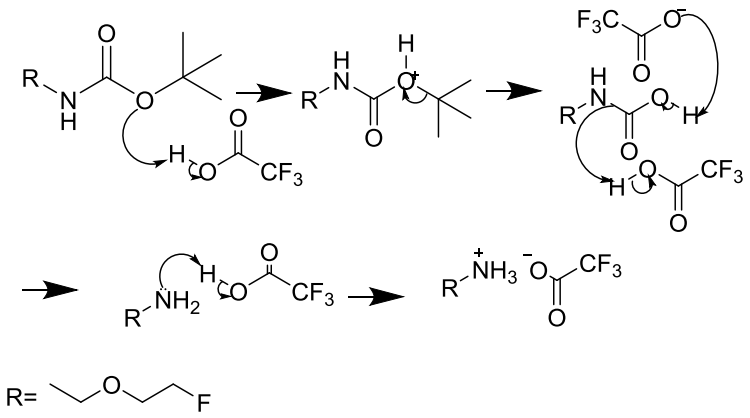

Figure 33: Reaction mechanism for (7).

This deprotection step was undertaken using TFA which protonates the *tert*-butyl carbamate group, and through carbo cation removal, a carbamic acid is formed. Decarboxylation then occurs leaving a primary amine group which is then protonated due to acidic conditions. HCl in diethyl ether was then utilised to form an amine hydrochloride salt which could be filtered to yield **7**, as TFA is soluble in diethyl ether and the hydrochloride salt is less soluble than the triflate salt. A yield of 95.2% was obtained which was comparable to reported yields.

MS highlighted a significant peak at m/z 108.2 which corresponds to **7** without the Cl^- counterion as the compound dissociates within the solution. As expected, the NMR (**Figure 34**) is similar to that of **6** however there is no large singlet peak at 1.42 suggesting the removal of the Boc group.

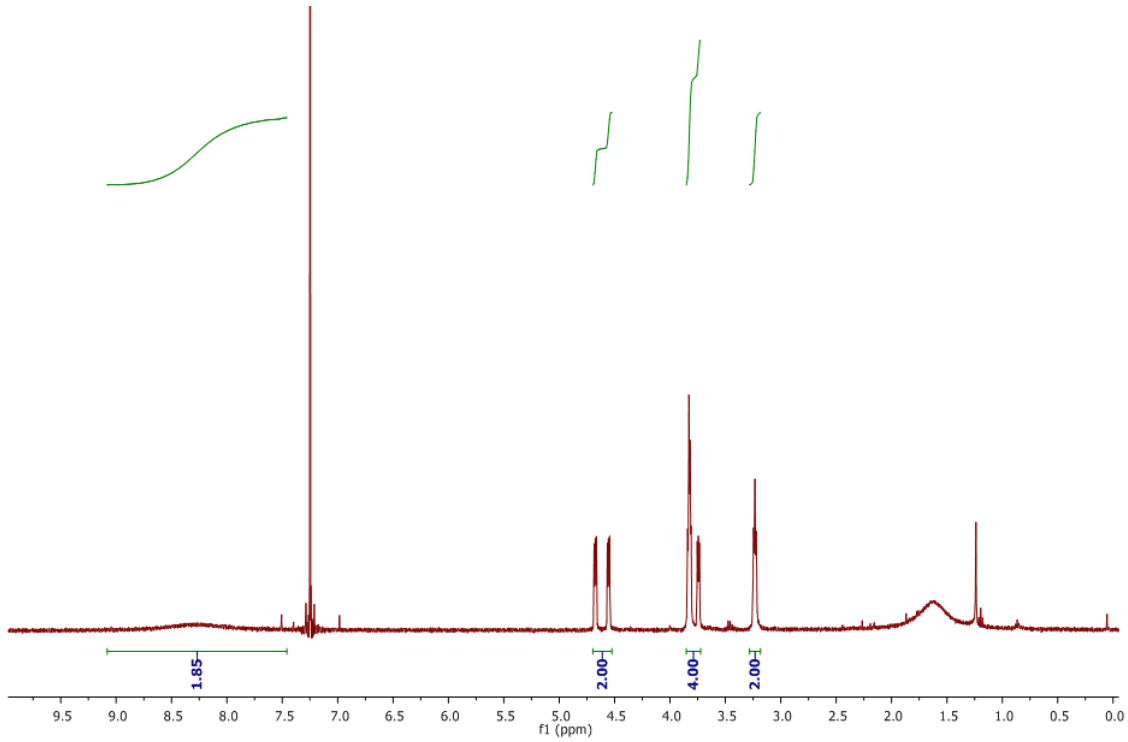

Figure 34: ^{1}H NMR for compound **7**.

*3.1.7. Synthesis: 2-((2-(2-fluoroethoxy)ethyl)amino)-N-(quinolin-8-yl)acetamide **(8)***

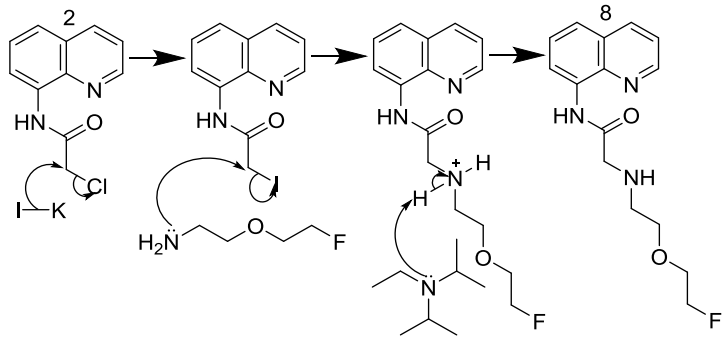

Figure 35: Reaction mechanism for (8).

The synthesis of AQA-F (**8**) was completed using the same method as **3.** A halogen exchange with KI provided a better leaving group for the side chain to react with through nucleophilic substitution. An S_N2 reaction takes place where the lone pair of the amine of 2-(2-aminoethoxy)ethanol attacks the secondary carbon of the intermediate. DIPEA then deprotonates the quaternary amine cation to yield **8**.

MS highlighted peaks at m/z 292.1 $[M+H]^+$ and 314.2 $[M+Na]^+$ all could correspond to **8**. A peak at m/z 293.1 was also observed which could correspond to **8** with ^{13}C isotopes. In this reaction there is a lack of a peak at m/z 129.8 suggesting that that the DIPEA was successfully removed during purification. Post-column chromatography NMR (**Figure 36**) peaks correspond to those of **3**, with some minor differences. For example, the doublet of triplet peaks seen at 4.5 ppm correspond to the 2 protons next to the fluorine. This resonance occurs at a higher chemical shift than the equivalent environment in **3** (4 ppm) due to the greater electronegativity of F compared to OH resulting in the adjacent protons being more deshielded. The large coupling of this doublet ($^2J_{HF}$ = 47.7 Hz) is characteristic of a $^2J_{HF}$ splitting further confirming the identity of this proton environment.

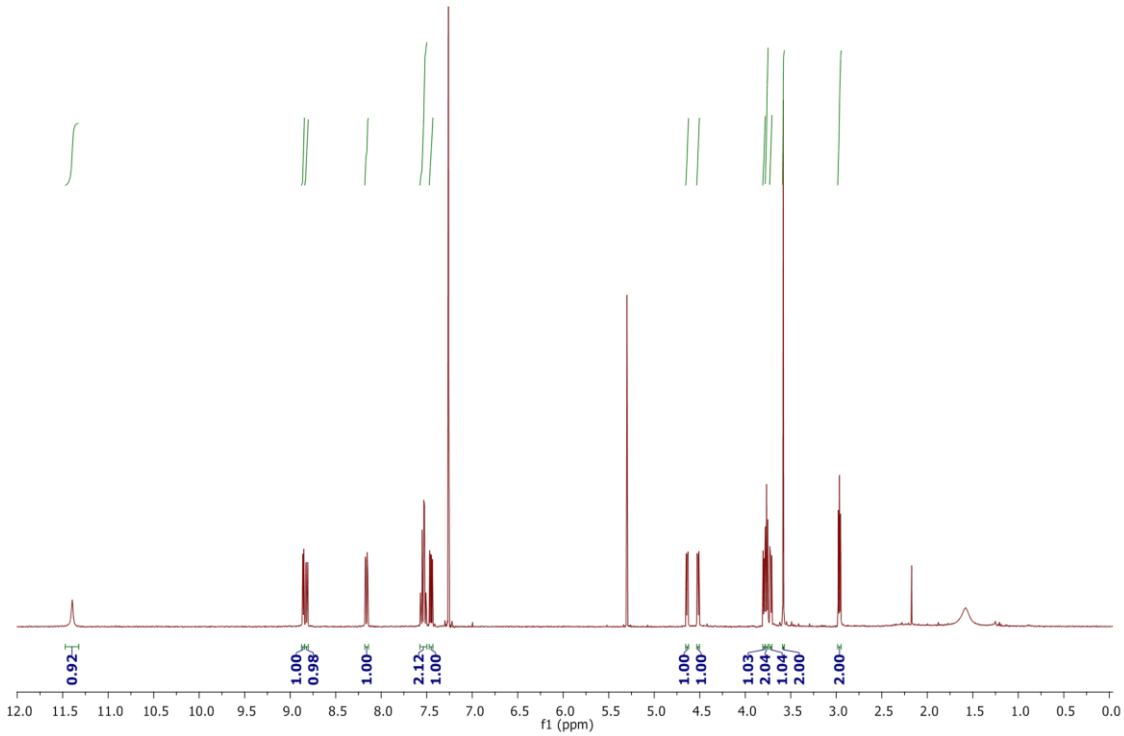

Figure 36: ^{1}H NMR for compound **8**.

3.2. Physical Studies

3.2.1 Photoluminescence

After successfully synthesising the probe, it was important to measure the physical properties to determine if AQA-F **(8)** would function as a Zn^{2+} sensor. In particular, the fluorescence of the probe was assessed as this is one of the imaging modalities. The excitation and emission spectra were determined using a fluoromax-4 spectrofluorometer and are both shown in **Figure 37**. A maximum excitation peak was observed at 320 nm for AQA-F which will be utilised during future experiments for maximum fluorescence intensity. Upon the addition of 1 equivalent of Zn^{2+}, no change in the excitation maxima was observed. This is contrasted in the emission spectra where a significant increase in fluorescence intensity is seen with a bathochromic shift of 80 nm. It was found that exciting the probe at 320 nm produced a peak fluorescence emission at 420 nm in the absence of zinc. However, upon addition of one equivalent of zinc a red shift was observed, producing an emission maximum at 500 nm.

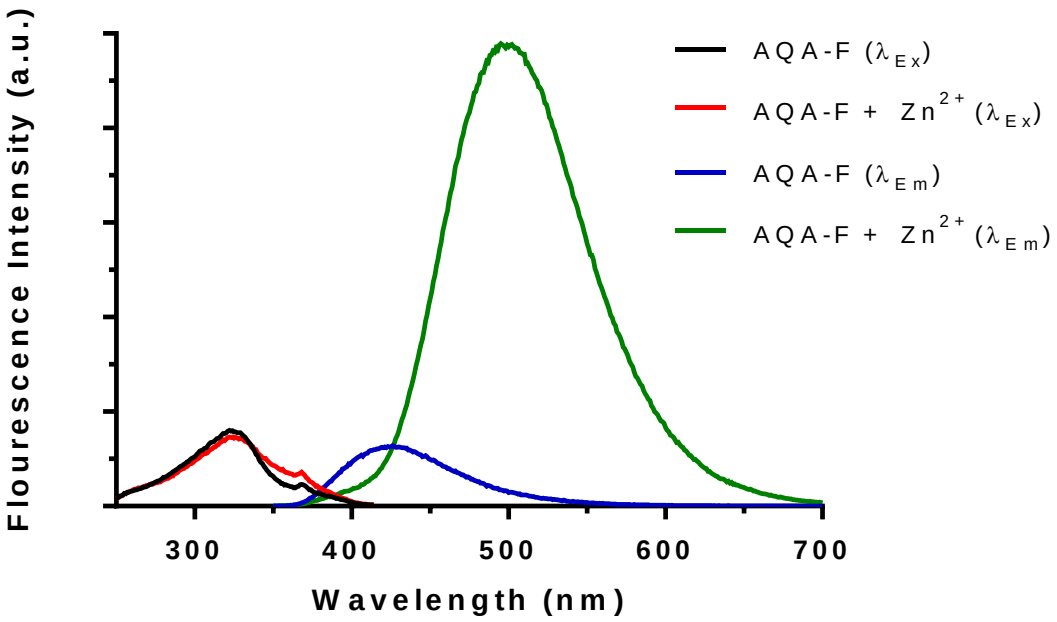

Figure 37: Excitation and emission spectra for AQA-F (0.1 mM) in HEPES buffer (10 mM, pH = 7.68) in the absence and presence of one equivalent of zinc.

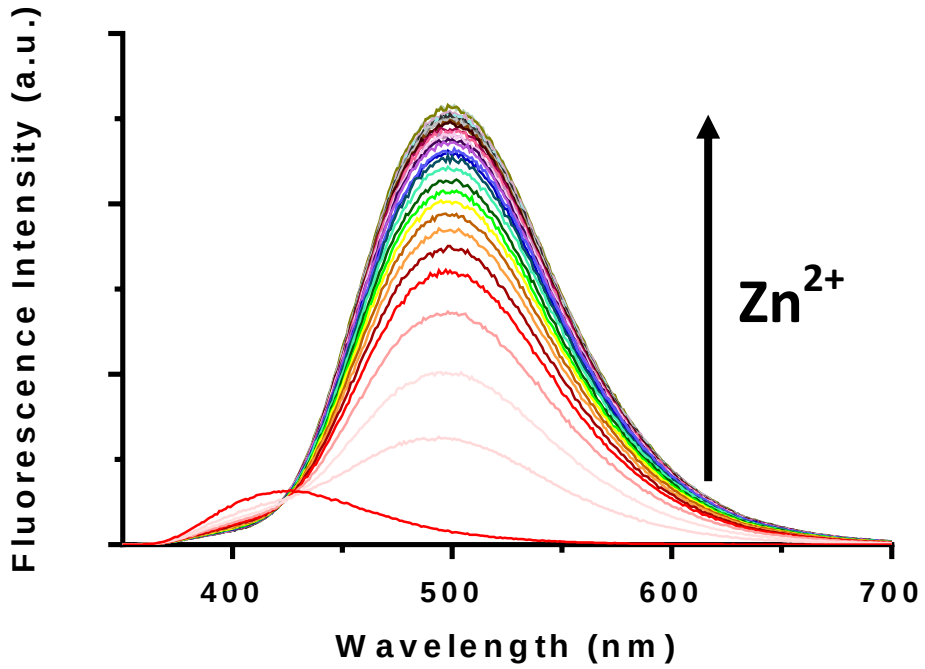

Figure 38: Fluorescence spectra for AQA-F (0.1 mM) in HEPES buffer (10 mM, pH = 7.68) with increasing concentrations of zinc (0-3 equivalences).

The bathochromic shift observed with AQA-F is similar to the OH analogue reported by Zhang *et al,* 2008. This emission profile will be beneficial when utilising the probe during *in vitro* studies as there will be a clear distinction between free probe and Zn^{2+} bound probe. AQA-F that is not bound to zinc should emit at 420 nm in the blue range, whereas probe that is bound to zinc should emit at 500 nm in the green range. This in principle can be applied to diagnosing prostate cancer by monitoring endogenous Zn^{2+} as Zn^{2+} levels in prostate cancer are significantly reduced (Costello and Franklin, 2009). Therefore, weaker green fluorescence should be observed when compared to healthy prostate tissue. The intensity of fluorescence drastically increased after the addition of zinc, showing a 6-fold increase upon addition of one equivalent of zinc. The 8-aminoquinoline unit of the probe acts as a cation receptor, which upon zinc chelation, donates electrons from the carboxyamido group to form a metal complex. Following the deprotonation of the carboxyamido group, the intramolecular hydrogen bond of 8-aminoquinoline is prevented from forming, thus inhibiting the intramolecular electron-transfer process. In the absence of zinc, this process would quench the fluorescence of quinoline (Xu *et al*, 2010).

Figure 39 corresponds to the maximum fluorescence intensity at 500 nm with increasing concentrations of zinc. This graph supports previous findings that the AQA based probe binds in a 1:1 molar ratio with zinc as it reaches maximum intensity after one equivalent of zinc. This graph was utilised to determine the equilibrium disassociation constant (K_d) which signifies the likelihood a complex will disassociate into its smaller components. The K_d was calculated to be $14x10^{-6}$ M at pH 7.68 using a one site – total non-linear regression fit which is comparable to the K_d of the Gd(III) probe reported by Stasiuk *et al,* 2015. However, this is significantly different than the

OH probe. These differences may be due to the non-linear regression fit that was chosen or may be due to the sensitivity of the instrument used.

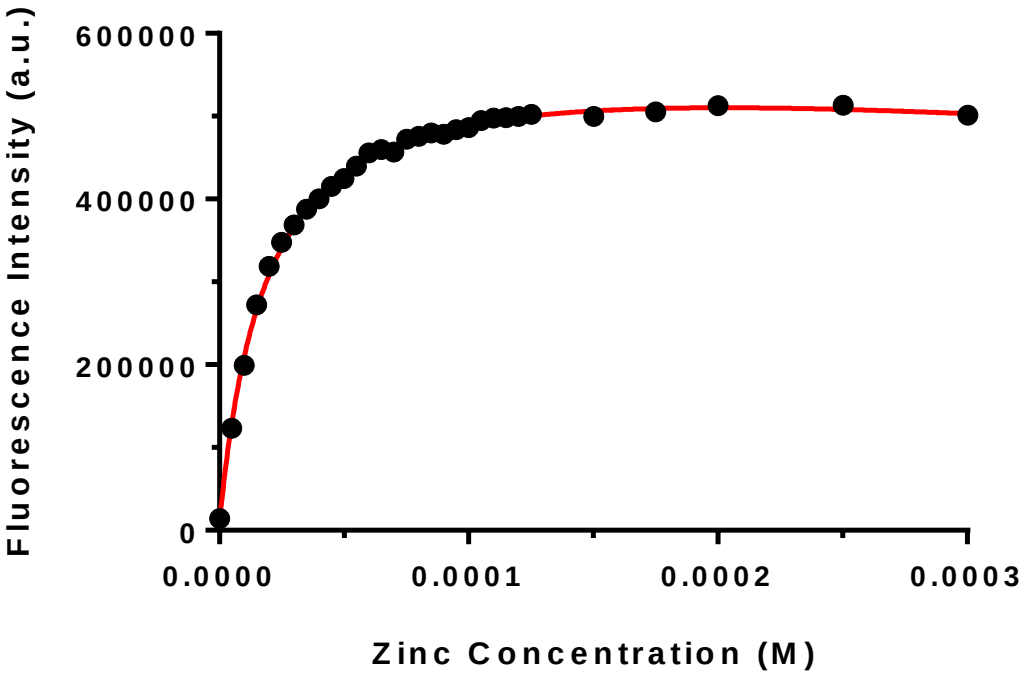

Figure 39: Fluorescence intensity at 500 nm for the AQA-F probe (0.1 mM) in HEPES buffer (10 mM, pH = 7.68) with increasing concentrations of zinc (0-3 equivalences).

3.2.2 Absorbance

The zinc binding was also investigated using a UV-Vis spectrophotometer and is highlighted in **Figure 40**. The graph shows how the absorbance of the probe changes with increasing zinc concentration. The results obtained are as expected, as it suggests the probe is binding the zinc as there is a decrease in intensity and a shift to a higher wavelength. Looking at **Figure 40**, three isosbestic points can be seen at 243, 280 and 323 nm. This matches results from the OH analogue probe reported by Zhang *et al*, 2008 whereby they witnessed three isosbestic points at 242, 280 and 324 nm. This similarity is expected due to the minor changes from OH and F as this region is distant from the fluorescent quinoline unit.

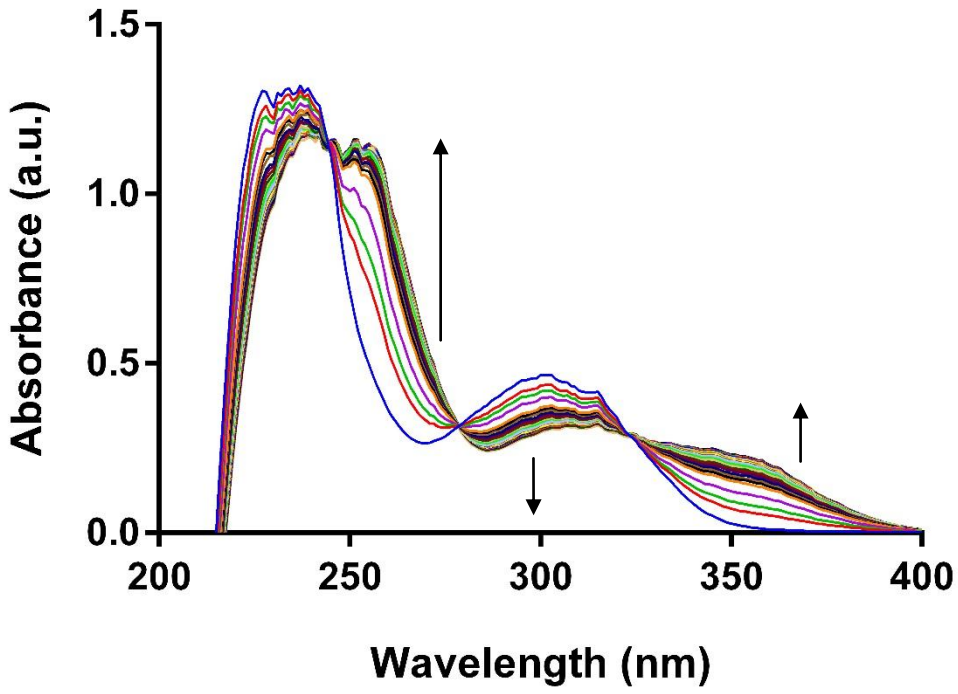

Figure 40: Absorption spectra for AQA-F (0.1 mM) in HEPES buffer (10 mM, pH = 7.68) that changes with increasing concentrations of zinc.

Figure 41 shows the absorbance ratio obtained by dividing the absorbance at 350 nm with the absorbance at 300nm. This graph highlights how the ratio increases with increasing concentrations of zinc up to 1 equivalent and then plateaus off. From this it can be determined that the probe binds zinc in a one to one molar ratio, suggesting that a complex is formed between the ligand and the metal ion. This graph allowed for the determination of the association constant (K_a) which was calculated to be 5.6×10^5 M^{-1}. Surprisingly, this value is significantly lower than that reported by Zhang *et al, 2008* ($K_a = 6.7 \times 10^6$ M^{-1}). The fit used by Zhang *et* al, 2008 is not well described – as such this may be a source of this difference. However, a number of fits were used to calculate the value for AQA-F all giving values in a similar range. Zhang *et* al performed their titration at 10 μM ligand concentration, whereas the titration of AQA-F was performed at 0.1 mM. Their first addition of zinc was around 1 μM, here we added 10 μM in accordance with Stasiuk *et* al, 2015. This may affect the fit in such a way as to prevent the lower limit from being accurately determined.

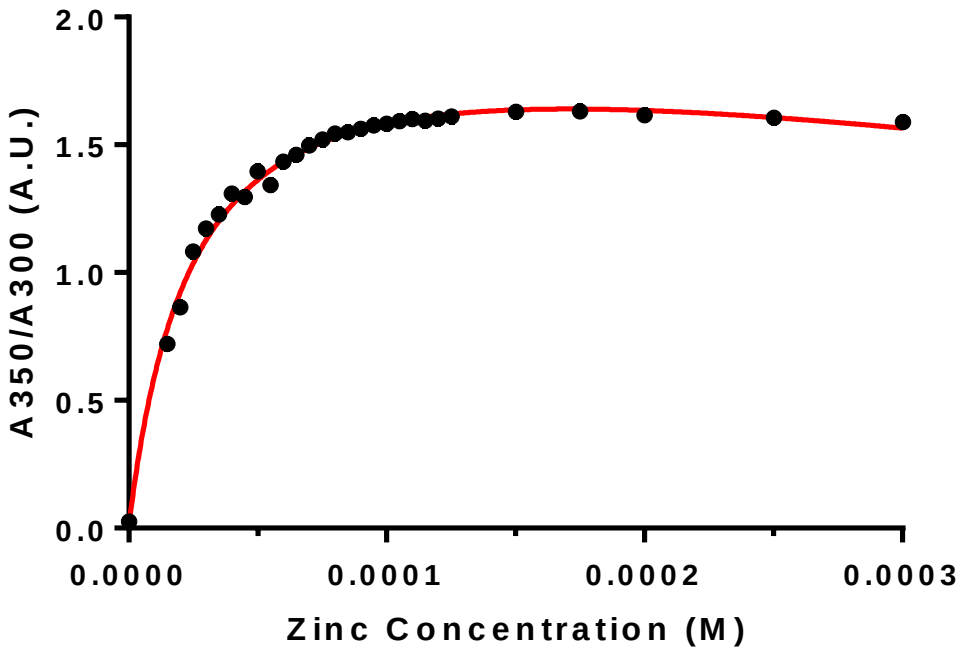

Figure 41: Ratiometric curve of A350/A300 with increasing concentrations of zinc.

There are many metal ions present in the body that could interfere when using this probe as a medical imaging tool, therefore the binding capabilities of AQA-F were also investigated with various metals. This metal binding study would also determine if the probes fluorescence response was specific for zinc. The binding affinities are summarised in **Table 10**.

The binding dissociation constants were determined for various metals by plotting the absorbance intensity ratio (A350/A300) with increasing concentrations of metal, shown in **Appendix 1**. A one site – total nonlinear regression was then plotted using graphpad software which was then used to determine the K_d. A list of various metal ions and the corresponding K_d for AQA-F can be seen in **Table 10**. The binding dissociation constant for Zn^{2+} was determined to be the lowest at 14 μM, therefore suggesting the interaction between AQA-F and Zn^{2+} is stronger than the other metals tested. Mn^{2+} also had a low K_d however looking at the absorption spectra, as seen in **Appendix 1F**, it is evident that AQA-F is not binding to Mn^{2+} as little change in the absorbance is seen upon addition of the metal. This suggests that in this case the fitting is poor for this titration.

Copper(II), cobalt(II) and cadmium(II) (see **Appendix 1D, 1C, 1B** respectively) all appear to reach a maximum absorbance at approximately half an equivalent of metal. This suggests that the complex formed between AQA-F and these metals is in a 2:1 ratio of ligand:metal. The ligand AQA-F is expected to be tridentate – this suggests that in the case of these three metals the coordination geometry is octahedral, whereas in the case of other metals (in particular zinc(II)) the geometry is tetrahedral. This is expected for cobalt(II) (Carabineiro *et al*, 2007) and cadmium(II) (Pons *et al*, 2007), whilst both

tetrahedral and octahedral complexes of copper(II) are prevalent in the literature (see Cu-EDTA, Cu-DTPA, Cu-NOTA) (Wadas *et al*, 2010).

Table 10: A table summarising the binding disassociation constants in μM for AQA-F with various metals.

Metal Ion	Binding dissociation constant, K_d (μM)
Ca^{2+}	128
Cd^{2+}	77
Co^{2+}	25
Cu^{2+}	77
Fe^{2+}	140
Hg^{2+}	51
Mn^{2+}	-
Ni^{2+}	69
Zn^{2+}	14

3.2.1 Fluorescence Response with Various Metals

The fluorescence intensity of AQA-F was investigated with various metals to establish the response that they may have. The emission of the probe (λ_{ex} = 320 nm) was recorded and then one equivalent of metal was added to the solution. **Figure 42** shows the fluorescence intensity when AQA-F binds various metals. As the fluorescent response will be used for the determination of zinc concentration, a high specificity in the response for zinc over other metals is desired. In particular, biologically relevant metals such as copper, calcium and iron.

A slight reduction in fluorescence intensity was observed with Fe^{2+}, Co^{2+} and Hg^{2+}, as opposed to Ca^{2+}, Cu^{2+}, and Mn^{2+} where a small increase was seen. These results are promising as there isn't a significant increase in fluorescence intensity with these

metal ions. Therefore, if this probe was used as a zinc sensor the majority of the fluorescence would come from zinc-bound probe.

A significant increase in fluorescence intensity at 500 nm was observed with both Cd^{2+} and Zn^{2+}. As Cd^{2+} is in the same group as Zn^{2+} it is expected that a similar response would occur due to their similar electronic configuration. However, low concentrations of Cd^{2+} are present in the body due to it being toxic (Brzóska and Moniuszko-Jakoniuk, 2001), this would therefore not be a problem for *in vivo* applications. The increase for zinc-bound probe is 20-fold greater than free probe. This suggests that the majority of the fluorescence observed at 500 nm will be probe that is bound to zinc instead of the other metal ions tested. This is important for *in vitro* and *in vivo* applications as there are many metal ions present within cells that the probe could bind to; however these results suggest that the significant increase in fluorescence intensity at 500 nm is specific for zinc.

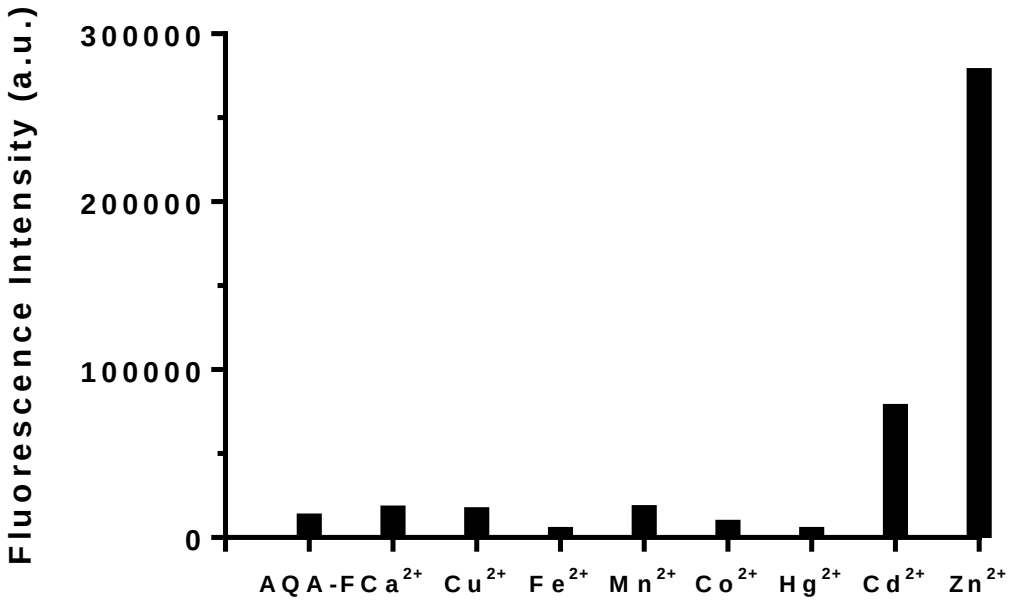

Figure 42: Metal binding assay showing the fluorescence response of AQA-F (0.1 mM) in HEPES buffer (10 mM, pH = 7.68) upon addition of 1 equivalent of metal chloride.

3.2.4. Quantum Yield and Lifetime

The fluorescence quantum yield was determined by measuring the absorbance and emission of AQA-F at various concentrations. The peak absorption was plotted against the integrated fluorescence intensity and a linear regression was fitted. The gradient of this line was then entered into an equation, shown in **figure 43**, along with values obtained from plotting a standard compound. Quinine sulfate was used as a standard as it absorbs and emits in a similar wavelength region as AQA-F. The results and the corresponding quantum yields for AQA-F, AQA-F with Zn^{2+} and quinine sulfate are highlighted in **Figure 44** and **Table 11** respectively**.**

$$\boldsymbol{\phi_x = \phi_{ST}\left(\frac{Grad_x}{Grad_{ST}}\right)\left(\frac{\eta_x^2}{\eta_{ST}^2}\right)}$$

Figure 43: Equation to calculate quantum yield where Φ is the fluorescence quantum yield, x is the sample, ST is the standard, Grad is the gradient from the plot of absorbance vs integrated fluorescence intensity and η is the refractive index of the solvent (Williams *et al*, 1983).

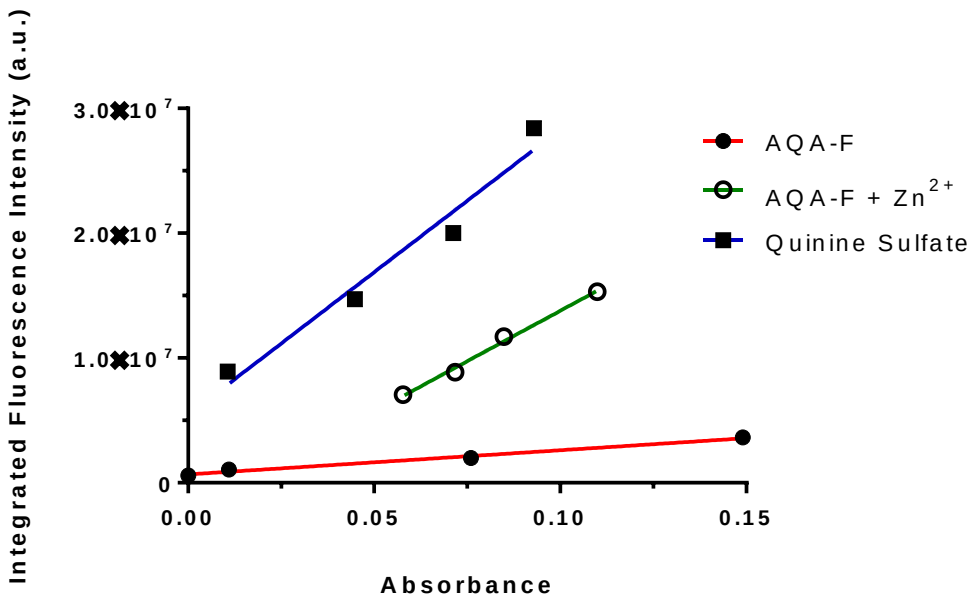

Figure 44: Plot of absorbance against integrated fluorescence intensity for AQA-F, AQA-F + Zn^{2+} and quinine sulfate (λ_{ex}=320 nm).

Table 11: Quantum yields for AQA-F in the absence and presence of one equivalent of Zn^{2+} compared to quinine sulfate as standard.

Compound	Gradient of linear regression	Φ_f
AQA-F	$1.938x10^7$	0.042 (4.2%)
AQA-F and Zn^{2+}	$1.617x10^8$	0.35 (35%)
Quinine Sulfate	$2.289x10^8$	0.5 (50%)

The calculated quantum yields for AQA-F, as shown in Table x, were significantly higher than expected. AQA-F in the absence of Zn^{2+} had a fluorescence quantum yield of 0.042 (4.2%), significantly lower compared to the quinine sulfate at 0.5 (50%). However, upon addition of one equivalent of Zn^{2+} the quantum yield of AQA-F increased 8 fold giving a value of 0.35 (35%). This increase in quantum yield was expected as there is a significant increase in fluorescence intensity when the probe binds Zn^{2+} (**Figure 38**). When comparing this value to the quantum yield of AQA-Gd, Stasiuk *et al*, 2015 reported quantum yields of 0.000018 and 0.00236 for their AQA derivative, in the absence and presence of Zn^{2+} respectively. This significant difference in quantum yield values may be a as a result of the lanthanide quenching the fluorescence of the quinoline unit. However, Zhang *et al*, 2008 also reported an 8-fold increase in quantum yield for AQA-OH.

3.2.5. pH Titration

A pH titration was performed to investigate the fluorescence response of AQA-F at different proton concentrations, and the effect of pH on the response to zinc. It was hypothesised that the fluorescence intensity would be decreased at acidic pH as the zinc binding capabilities would be hindered. This phenomenon has previously been seen in AQA-OH and AQA-Gd (Zhang *et al*, 2008, Stasiuk *et al*, 2015). The data obtained for AQA-F and the AQA-F-Zn^{2+} complex is shown in **Figure 45** and **Figure 46** respectively.

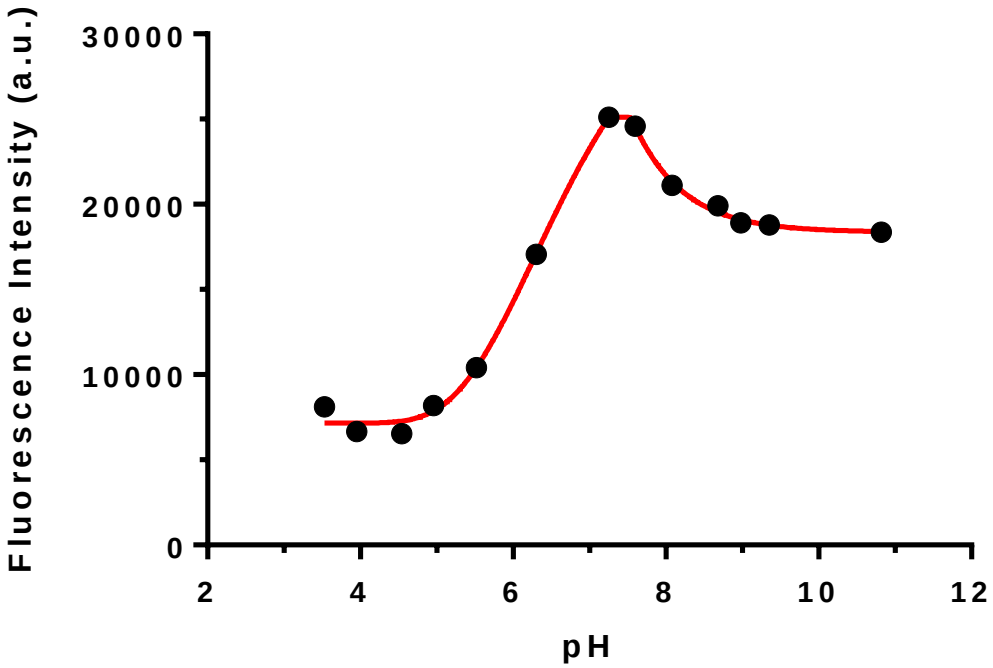

Figure 45: Fluorescence intensity at 500 nm for the AQA-F probe (0.1 mM) in KCl solution (0.1 M, pH = 7.68) at various pH. pH was adjusted using HCl (0.1 M) and NaOH (0.1 M).

It is important to note that the probe was diluted in HEPES buffer to maintain a physiological pH as Zhang *et al*, 2008 has reported that the OH probe does not form a complex with zinc in acidic conditions. This is as a result of the protonation of the amine groups which prevents the Zn^{2+} from binding; therefore an increase in fluorescence intensity is not seen.

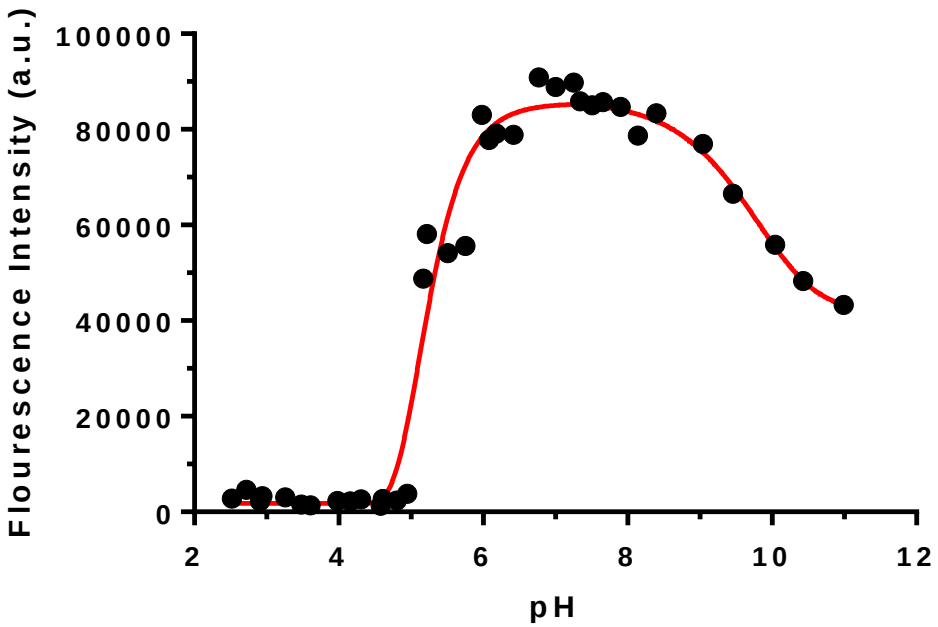

Figure 46: Fluorescence intensity at 500 nm for the AQA-F probe (0.1 mM) with one equivalent of zinc in KCl solution (0.1 M, pH = 7.68) at various pH. pH was adjusted using HCl (0.1 M) and NaOH (0.1 M).

An asymmetric sigmoidal line was plotted for the data in **Figure 45** and **Figure 46** and was utilised to determine the pK_a values for AQA-F. The pK_a values for AQA-F-Zn^{2+} were determined to be 5.25 and 9.65. A decrease in fluorescence intensity was observed for both the ligand and the complex at acidic pH which was expected to be attributed to the protonation of the amino group on the side chain. This protonation is thought to limit zinc binding causing the reduction in fluorescence intensity observed. This could cause problems when transitioning the probe into *in vitro* studies as lysosomal pH is thought to be 4.5-5 (Mindell, 2012). Therefore, if this probe did localise to the lysosomes a very weak fluorescence emission would be observed. Due to the large endogenous concentrations of zinc in the mitochondria, it is more likely that this probe binds zinc in the mitochondria however fluorescence co-localisation studies must be performed to confirm this. The pH of the cytosol of the mitochondria is reported to be around 7 (Alberts *et al*, 2002) so this shouldn't impede the fluorescence of AQA-F.

The fluorescence intensity begins to increase at pH 5, with the maximum intensity observed in the physiological pH window which is promising for *in vivo* applications. If the probe were to be implemented as an imaging agent, the fluorescence intensity would not be compromised as physiological pH is estimated to be 7.4, with tumour tissue being slightly acidic at pH 6-7.2 (Li *et al,* 2015). Therefore, the fluorescence intensity of AQA-F would not be significantly affected at this pH.

As the pH rises above 9, this results in a reduction in fluorescence intensity, however this decrease was not as significant as that observed at acidic pH. This fluorescence quenching could be attributed to the deprotonation of H_2O which is thought to be incorporated into the AQA-F complex when binding zinc, as seen in Stasiuk, 2010. Another possible explanation involves the formation of zinc hydroxide which would reduce the amount of available zinc for the probe to bind and would therefore impact the intensity of the fluorescence recorded.

Similar observations at low and high pH were also reported by Zhang *et al,* 2008 where they measured the response of the OH analogue at various pH. This is expected as the halogen should not have a significant effect on the pK_a of the probe as it is a significant distance away from the zinc binding and fluorescence moieties.

3.3. in vitro Validation

3.3.1. Probe Toxicity

Although fluorescent imaging probes can be implemented in diagnosing disease, they can also be toxic to healthy cells. Therefore, it is important to assess the affect the probe will have on cell viability. AQA-F was incubated overnight in four different cell types and the absorbance of MTS at 490 nm was recorded the following day. The results were then normalised and are shown in **Figure 47, 48** and **49** for RWPE-1, HEK293, RWPE-2 and PC-3 cells respectively.

RWPE-1 cells represent normal prostate epithelial cells that should contain high levels of zinc in comparison to the negative control cell type HEK293. RWPE-2 cells will be utilised as they possess a ras mutation which makes this cell type cancer-like. This will therefore act as an intermediate between healthy prostate (RWPE-1 cells) and cancerous prostate (PC-3). It is proposed that PC-3 cells should possess significantly reduced endogenous zinc concentrations in comparison to healthy prostate, therefore it is hypothesised that there should be a significant difference between each of these cell types when treated with AQA-F.

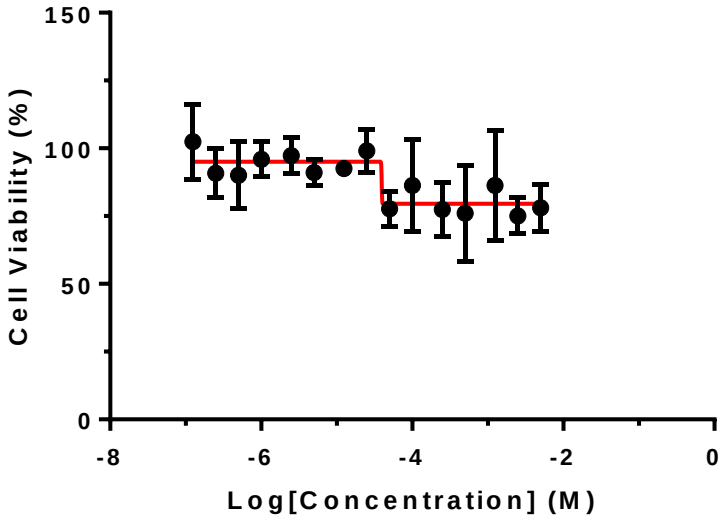

Figure 47: A graph showing the cell viability of RWPE-1 cells after overnight incubation with various concentrations of AQA-F.

At the concentrations used, minor changes were observed when AQA-F was incubated with RWPE-1 cells as seen in **Figure 47**. Cell viability decreased following concentrations greater than 250 μM to 75%, however this remained constant for the following concentrations that were applied. This suggests that the probe would be safe to use as micromolar concentrations are commonly applied during *in vitro* fluorescence experiments. This can also be used to estimate the potential affect the probe may have during *in vivo* applications as PET tracers are often injected at nanomolar concentrations. Therefore, this data suggests that AQA-F would be safe for concentrations in the micromolar range, however it is assumed that concentrations lower than this will have a reduced affect.

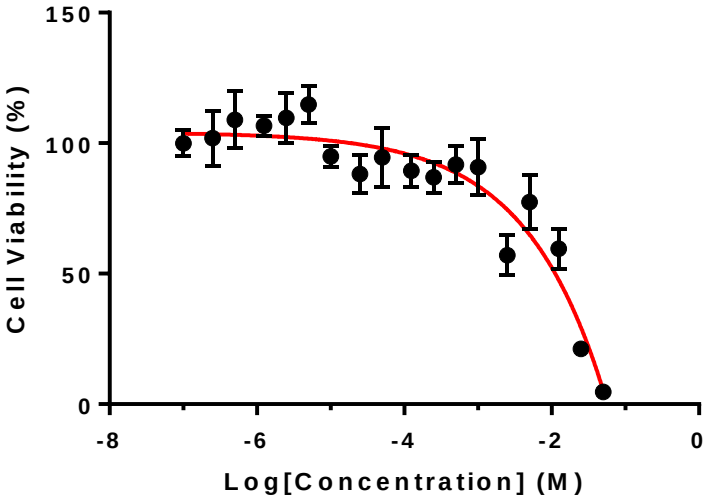

Figure 48: A graph showing the cell viability of HEK293 cells after overnight incubation with various concentrations of AQA-F.

HEK293 cells were implemented as a control cell type during this experiment to see how the probe would behave with other tissue types outside of the prostate. **Figure 48** suggests that at mM concentrations the cell viability is hindered by AQA-F, showing that the probe is toxic to this kidney cell line at these concentrations. Unlike the RWPE-1 cells, the cell viability of the HEK293 cells appears to decrease severely at concentrations greater than 1 mM. The IC_{50} for this cell type was determined to be 0.85 M, therefore incubating the probe at concentrations below this will have a negligible effect on cell viability. This IC_{50} is higher than the concentrations tested and is as a result of a lack of data points in the mM range. The non-linear regression that was fitted using graphpad is therefore poorly fitted to concentrations greater than 1 mM. This could be rectified in the future by incubating HEK293 cells with mM concentrations of AQA-F, however it was determined that this would be a waste of limited imaging agent as it was already found that AQA-F is not toxic at concentrations relevant for imaging.

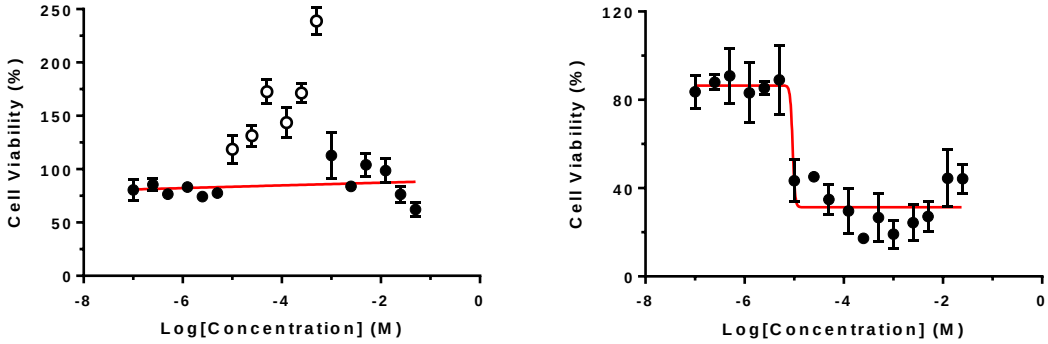

Figure 49: Two graphs showing the cell viability of RWPE-2 and PC3 cells respectively after overnight incubation with various concentrations of AQA-F.

The probes toxicity was also tested in two cell lines that represented prostate cancer, shown in **Figure 49**. RWPE-2 being a k-ras mutated prostate cell that is cancer-like and PC-3, a cell line which was derived from grade IV prostate adenocarcinoma cells which had metastasised to the bone. The graph that represents the results from the MTS assay for the RWPE-2 cell line appears to have some errors. The 6 data points between $x10^{-5}$ and $x10^{-3}$ M are significantly greater than the other concentrations used and have therefore been omitted as anomalies when plotting the fit. This is most likely as a result of a contaminated stock solution as the bacteria would reduce the MTS solution creating a darker solution and therefore a higher absorbance reading. When this is normalised to the controls, it gives a cell viability value significantly greater than 100%. If these data points are excluded as anomalies, then a similar pattern would be seen like in **Figure 48** where the cell viability remains relatively constant until mM concentrations.

The data obtained from the PC-3 cells during the MTS experiment is highlighted in **Figure 49** and shows a typical sigmoidal fit. However, this fit is shifted further left compared to those seen in **Figure 47** and **Figure 48**. An IC_{50} value of 9.3 μM suggests

that the probe is more toxic to the PC-3 cell line as oppose to the others used during this collection of experiments. The two data points at the greatest concentration suggest an increase in cell viability despite the cells being incubated with the greatest concentrations of probe. This was not seen in the other MTS assays and may be specific to the PC-3 cell lines; however it is more likely that these are anomalous results due to a greater cell density when seeding. A repeat of this experiment with the same concentrations and cell type would identify the validity of these points.

For further *in vitro* experiments, it has been shown that incubating AQA-F at micromolar or lower concentrations has no significant impact on cell viability in RWPE-1, HEK293, RWPE-2, and PC-3 cells. It is also worth noting that the incubation period used during this experiment was overnight, however for fluorescence experiments a much shorter time period will be used. As AQA-F will be incubated for short periods, it is assumed this will have less of an effect on cell viability when compared to overnight incubations.

3.3.2. Dose Response Fluorescence

Following the cell viability assays, it was concluded that the probe could be incubated with various cell types at micromolar concentrations without hindering cell viability. The next step to validating AQA-F was by performing a dose response fluorescence experiment. This experiment was implemented to identify the optimum concentration of probe to incubate the cells with to generate a fluorescence response with the greatest intensity. In order to achieve this, the cells were incubated for 30 minutes with various concentrations of AQA-F, fixed with 4% PFA and imaged using the high throughput fluorescence microscope. The micrographs were then analysed using

imageJ to identify the mean fluorescence intensity, with the results being displayed as a graph in **Figure 50** and as a collection of micrographs in **Appendix 2**.

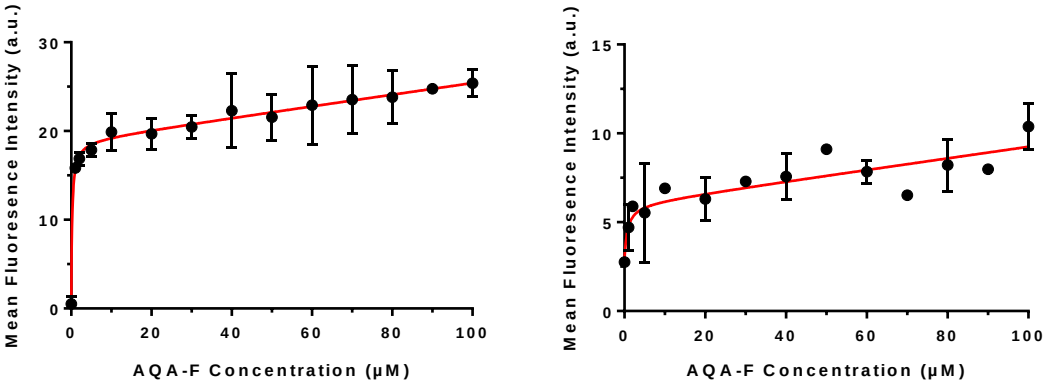

Figure 50: Mean fluorescence intensity as a function of probe concentration in RWPE-1 cells. The left graph corresponds to the blue fluorescence and the right graph shows the green fluorescence.

The mean blue fluorescence intensity appears to increase linearly up to a concentration of 100 µM where it begins to plateau. This would suggest that incubating with concentrations at 100 µM would produce the greatest fluorescence intensity. A linear relationship between fluorescence intensity and concentration is expect, as the greater the concentration of probe, the more fluorescence will be emitted. A plateau then may indicate that the RWPE-1 cells become saturated with AQA-F and can no longer internalise more probe, resulting in similar fluorescence intensity despite increasing probe concentration greater than 100 µM. Upon closer inspection of the micrographs, the average fluorescence intensity appears to increase with probe concentration supporting the evidence from the calculated mean fluorescence intensity. This suggests that calculating the mean fluorescence intensity using ImageJ was representative of the results obtained; however it is worth noting that cell viability can vary between images which results in a varied mean fluorescence

intensity. This was overcome by completing the experiment with an n=4 to obtain an average.

The mean fluorescence intensity of the green fluorescence was recorded and plotted in **Figure 50**. The data presented in a similar manner as the blue fluorescence, as a plateau which was expected. For example, there is a limited amount of intracellular Zn^{2+} therefore it is expected that the amount of green fluorescence would reach a maximum once all the free Zn^{2+} was chelated. This is suggested as at concentrations greater than 10 μM, the mean fluorescence intensity remains relatively constant.

This experiment also showed that the probe enters the cell and binds endogenous zinc as fluorescence both in the blue and green ranges can be seen (**Appendix 2**). When consulting the micrographs, it appears that the probe localises to the organelles present in the cytosol, with little fluorescence being emitted from the nucleus. Furthermore, the free and zinc-bound probe appear to localise to different parts of the cell. This will be investigated further through co-localisation experiments which will help to identify the specific endogenous localisation of AQA-F. As AQA-F at a concentration of 100 μM produced fluorescence with the greatest intensity out of the concentrations which were applied, this will be used for future experiments.

3.3.3. Time Response Fluorescence

The optimum dose for AQA-F was established in the previous experiment, however the optimum period of incubation can vary depending on the uptake of the probe and the time it takes to be internalised. Therefore, a time response fluorescence experiment was executed to determine the optimum incubation time. To achieve this, 100 μM of AQA-F was incubated for 0-500 minutes in RWPE-1 cells and the mean fluorescence

intensity was recorded similar to *chapter 3.3.2.* The results are represented in **Figure 51** and displayed as micrographs in **Appendix 3**.

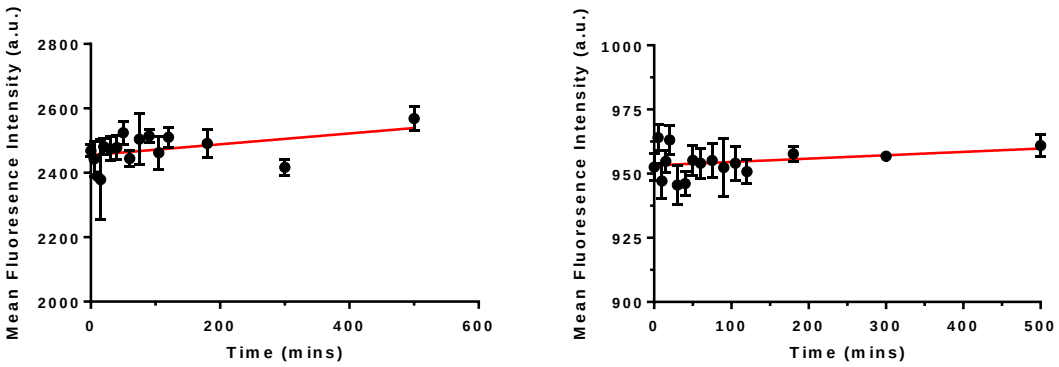

Figure 51: Mean fluorescence intensity with various AQA-F (100 μM) incubation times in RWPE-1 cells. The left graph corresponds to the blue fluorescence and the right graph shows the green fluorescence.

The data suggests that the mean fluorescence intensity for both wavelength ranges doesn't change significantly over a 500 minute incubation period. It was postulated that upon internalisation, AQA-F would bind a metal ion and would become charged. This would then prevent the probe from being removed by the cell. The graphs in **Figure 51** suggest that the probe remains internalised and fluorescent for all the incubation times tested during this experiment. This suggests that over the incubation time periods that were tested, the probe remained within the cell and was not removed. For future experiments an incubation time of 30 minutes will be implemented as incubating for longer periods of time would result in similar fluorescence intensity. Therefore, 30 minutes will be used to provide the optimal incubation time versus signal intensity.

3.3.4. Co-localisation

The localisation of AQA-F was important to determine as this would provide important information in how the probe behaves once internalised by the cell. The optimum dose and incubation times had previously been determined, and were therefore implemented during this experiment to achieve the optimum fluorescence intensity. AQA-F was incubated in combination with commercial dyes to investigate where the probe accumulates within a cell. This can be determined as the localisation of commercial dyes is already known, so if the probe co-localises with a commercial dye for a specific organelle, the localisation of AQA-F will be found. The following dyes were implemented: AQA-F, Rhodamine Concanavalin A (red cell membrane stain), Lysotracker (red lysosomal stain) and Mitotracker (deep red mitochondrial stain). Healthy prostate and prostate cancer cells, RWPE-1 and PC-3 respectively, will be implemented during this experiment. As the zinc concentrations are expected to vary between these two cell lines, it is hypothesised that more green fluorescence will be present in the RWPE-1 cells when compared to the PC-3 cells. The micrographs obtained for the various dyes incubated with RWPE-1 and PC-3 cells are shown in **Figure 52** and **Figure 53** respectively.

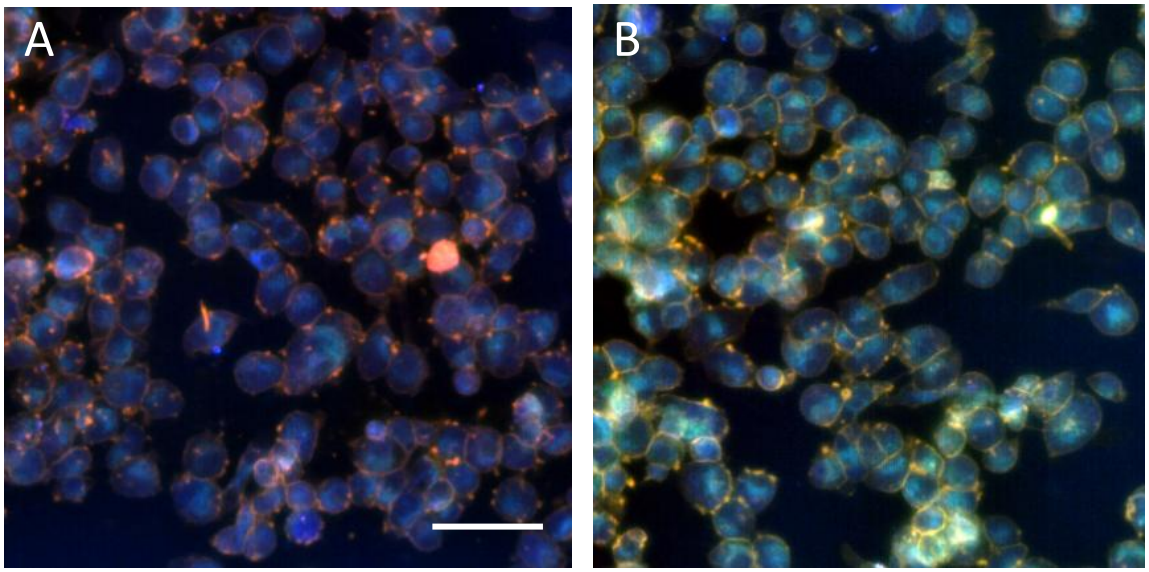

Figure 52: Two collections of micrographs that show RWPE-1 cells that have been incubated with Rhodamine Concanavalin A corresponding to the red channel and AQA-F which is represented by the blue channel for total probe and the green channel for AQA-F bound to Zn^{2+}. The cells present in (B) have been incubated overnight with a zinc chloride solution (1 mM). Scale bar = 50 μM.

Figure 52 shows RWPE-1 cells that have been incubated with AQA-F and Rhodamine Concanavalin A. Rhodamine Concanavalin A is a cell membrane dye that has a maximum excitation of 550 nm and an emission maximum at 575 nm, therefore we expect this dye to be visible in the red channel. Looking at these images, the Rhodamine-based dye has localised to the cell membrane of the RWPE-1 cells as expected. Blue and green fluorescence can also be seen from within the cell suggesting the intracellular presence of AQA-F. When consulting **Figure 52B**, a greater amount of intracellular green fluorescence can be seen compared to **Figure 52A**. This is as expected as the right hand image contains RWPE-1 cells that have been incubated overnight with a 1 mM zinc chloride solution before the addition of the two dyes. This was implemented in an attempt to increase the levels of endogenous Zn^{2+} to investigate if the probe could detect this change. As expected the amount of green fluorescence in the cells incubated with zinc is greater than those that did not. The

green channel upon closer inspection, seen in **Appendix 4**, appears to partially resemble the red channel. This could suggest that the probe which has bound Zn^{2+} is localising to the cell membrane as reported by Ghosh *et al*, 2010. Another possible explanation could be as a result of bleed through from the red channel which upon generating the overlay produces a cell membrane that appears orange-yellow as oppose to red. Due to minimal amounts of red fluorescence from within the cell, this does not hinder the cytosolic fluorescence which is seen with AQA-F.

Other dyes were implemented as well as Rhodamine Concanavalin A to investigate AQA-F localisation. Both Mitotracker red and Lysotracker red were implemented to determine mitochondrial and lysosomal localisation respectively. Due to a large amount of similarity between the red and green channel (seen in **Appendix 8** and **9** for RPWE-1 and PC-3 cells respectively), it is almost impossible to determine the localisation of AQA-F within the cell. It is worth noting that this similarity could be co-localisation and not bleed through, however upon consulting the images it is clear the red channel dyes when incubated in isolation possess some fluorescence in the green channel. In order to overcome this, it was determined that assessing co-localisation of AQA-F would have to be performed using confocal microscopy. Using confocal microscopy would allow the optimisation of exciting the dyes at specific wavelengths and collecting a specific fluorescence emission range. This would result in a reduction of cross over between fluorescence and improve the quality of the image.

The excitation of AQA-F had already been determined (**Figure 37**), therefore a laser that excited at a similar wavelength was required to receive the greatest fluorescence intensity. However, due to limited equipment the lowest laser available for confocal microscopy excited at 405 nm. When consulting the excitation of AQA-F, it is evident

that exciting at 405 nm would produce little to no emission. Rhodamine Concanavalin A was excited at a higher wavelength and the emission was visible suggesting that confocal microscopy could be used in the future. However, due to limited equipment confocal microscopy could not be used for AQA-F at this given time. Therefore, it was suggested that the high throughput microscope could be used for analysing cells that have been stained with AQA-F and the cell membrane dye. Confocal microscopy could be used to ascertain structural information which could become useful for future 3D cell cultures.

The PC-3 cells were treated with the same dyes as the RWPE-1 cell line to investigate how AQA-F would interact with a prostate cancer cell line. Due to the significantly lower endogenous Zn^{2+} concentration when compared to RWPE-1 cells (Costello and Franklin, 2009), it was hypothesised that less green fluorescence should be seen in PC-3 cells compared to RWPE-1 cells. It was also expected that upon incubation with a 1 mM zinc chloride solution, the green fluorescence intensity would be weaker than that seen with RWPE-1 treated with the same solution. This was hypothesised because, as discussed in *section 1.2.3.,* the transport of zinc is disrupted in prostate cancer cells therefore despite extracellular Zn^{2+} concentrations being high, only small amounts of Zn^{2+} are expected to be internalised. **Figure 53** shows two images of PC-3 cells that have been incubated with AQA-F, Rhodamine Concanavalin A in the absence and presence of a 1 mM zinc chloride solution.

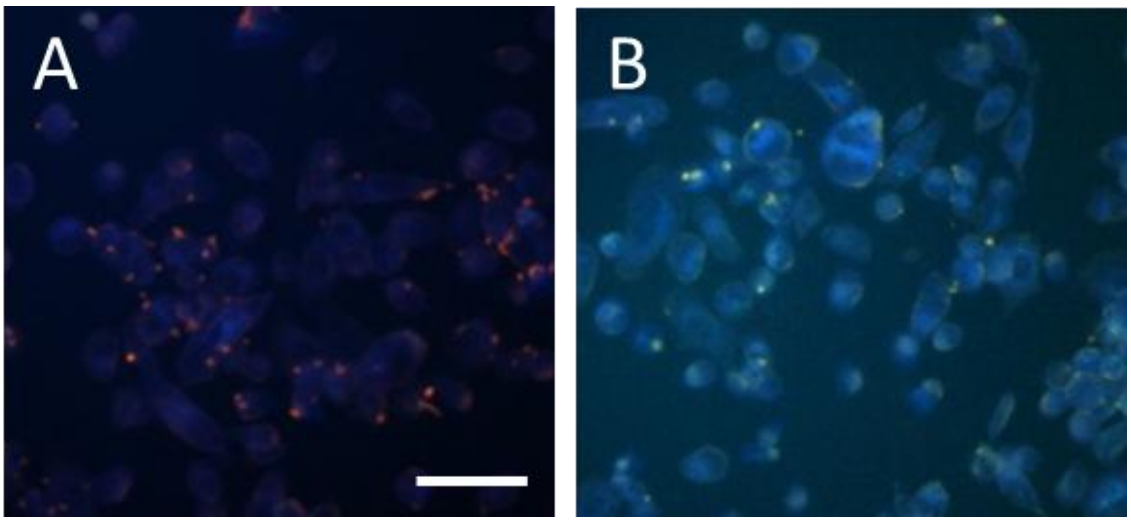

Figure 53: Two collections of micrographs that show PC-3 cells that have been incubated with Rhodamine Concanavalin A corresponding to the red channel and AQA-F which is represented by the blue channel for total probe and the green channel for AQA-F bound to Zn^{2+}. The cells present in (B) have been incubated overnight with a zinc chloride solution (1 mM). Scale bar = 50 µM.

As expected, there is little green fluorescence seen in **Figure 53A** compared to **Figure 53B** suggesting the intracellular concentration of Zn^{2+} is low. When this is compared with the micrographs obtained from RWPE-1 cells (**Figure 52A**), it is evident that there is a significant decrease in green fluorescence present in PC-3 cells. This was expected and suggests that AQA-F in principle could be used to determine intracellular concentrations of Zn^{2+} in healthy prostate and prostate cancer. This could improve prostate cancer diagnosis as AQA-F could be incubated with excised prostate tissue and image using fluorescence microscopy. This in theory would act as a test to determine zinc concentrations which could be combined with PSA and Gleason score to indicate the presence of prostate cancer.

In order to assess how AQA-F interacts with prostate tissue, a 3D model known as acini will be implemented. This model will act as a tissue-like structure for the investigation of AQA-F localisation.

3.3.5. 3D Cell Models

RWPE-1 and PC-3 cells were cultured on a reconstituted basement membrane (matrigel) to generate a 3D cell structure known as an acini. These acini could then be utilised to investigate how the probe interacts and functions with a small tissue-like structure. A stiffness model was also incorporated through glycoaldehyde treatment, as documented by Rodriguez-Teja *et al,* 2016, which should prevent the proper formation of acini. It was hypothesised that the endogenous levels of zinc vary between both basement membrane states; therefore AQA-F was also used to investigate this. The progression of these cell structures was imaged using a brightfield microscope at x40 and are shown in **Figure 54** and **Figure 55** for RWPE-1 and PC-3 cells respectively.

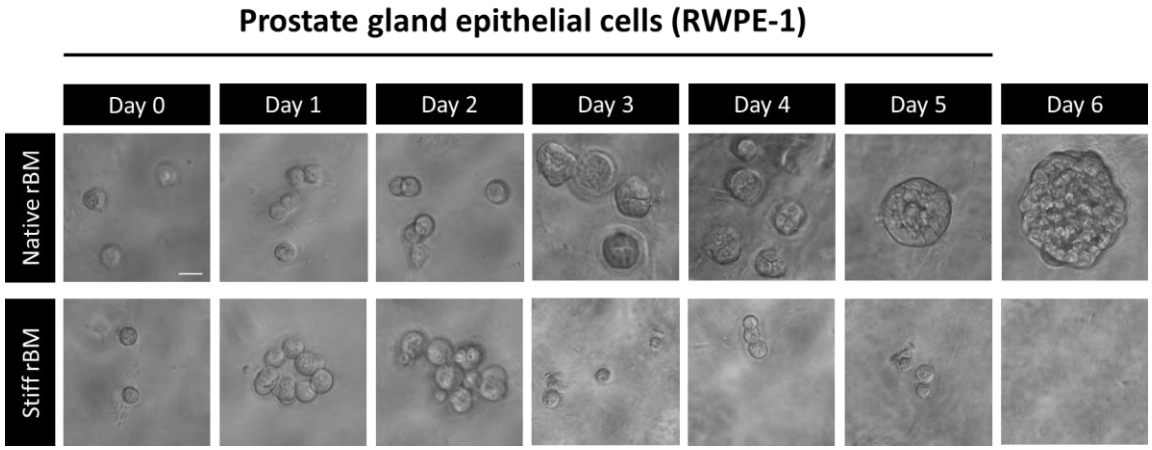

Figure 54: A collection of micrographs that show RWPE-1 cells cultured on native reconstituted basement membrane and a stiff version of the membrane. These images were taken using a brightfield microscope at x40, scale bar = 20 μM.

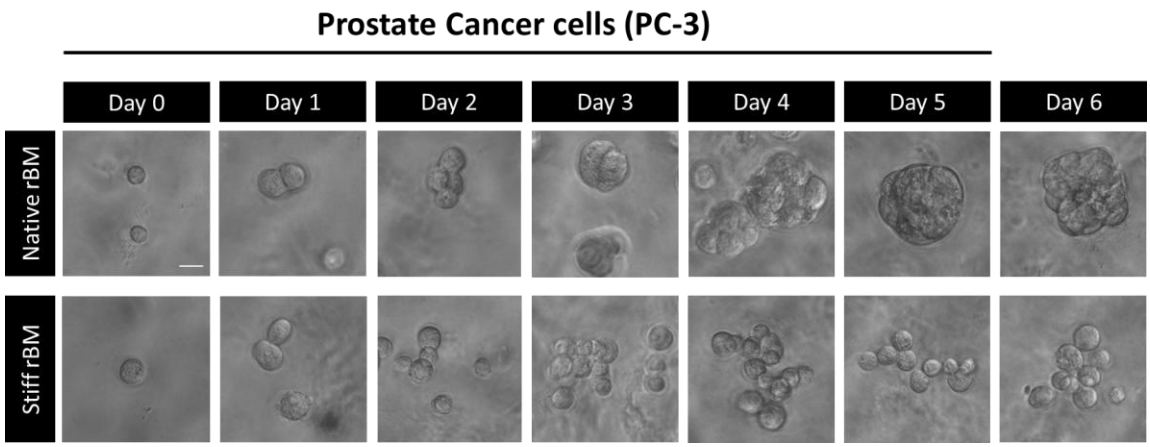

Figure 55: A collection of micrographs that show PC-3 cells cultured on native reconstituted basement membrane and a stiff version of the membrane. These images were taken using a brightfield microscope at x40, scale bar = 20 μM.

Healthy prostate cells derived from prostate tissue (RWPE-1) grown on the native reconstituted membrane (rBM) began to divide and organise into small clusters from day 0-3. From day 3, small uniform spheroids around 20 μM begin to form. After 6 days of growth, these RWPE-1 cells form uniform and highly organised acini. These tight symmetric structures were not replicated during PC-3 3D cultures. PC-3 cells (**Figure 55**) over the same time period formed irregular aggregates which consisted of a cluster of PC-3 cells.

This process of acini formation in both cell lines differed when applying the stiffness model. After 1 day, the RWPE-1 cells begin to form asymmetric clusters. After day 2, these cells are reported to have a polygonal shape, as appose to the spheroidal shape seen with RWPE-1 cells cultured on native rBM. Some cells as part of this disrupted structure have been shown to migrate into the stiff rBM (Rodriguez-Teja *et al,* 2016), however when consulting the images from day 3 for the stiff model this is not the case for this experiment. A lack of cell density was apparent when imaging the cells from day 3 which most likely occurred when the media was changed. These stiff acini are

associated with a loss of apical-to-basal polarity (Rodriguez-Teja *et al,* 2015), therefore it can be speculated that these cells are more fragile so can be dislodged from the stiff rBM more easily than the native rBM. Due to time constraints, this stiff model wasn't repeated however for future experiments, it is advised to pipette new additions of media very gently whilst leaving some of the old media behind, ensuring the cells will not become detached. The stiffness model was replicated better in the PC-3 cell line as a difference between native and stiff is clearly evident. PC-3 cells began to grow in lines and cluster together; however they could not form proper cell-cell junctions as seen in the native model.

Figure 54 and **Figure 55** show the progression of RWPE-1 and PC-3 cells in a native and stiff rBM and is evidence that acini can be successfully grown following the protocol described by Rodriguez-Teja *et al,* 2016. These acini were then stained using AQA-F, DAPI and Rhodamine Concanavalin A, fixed using 4% PFA and were imaged using both the high throughput fluorescence microscope and the confocal microscope.

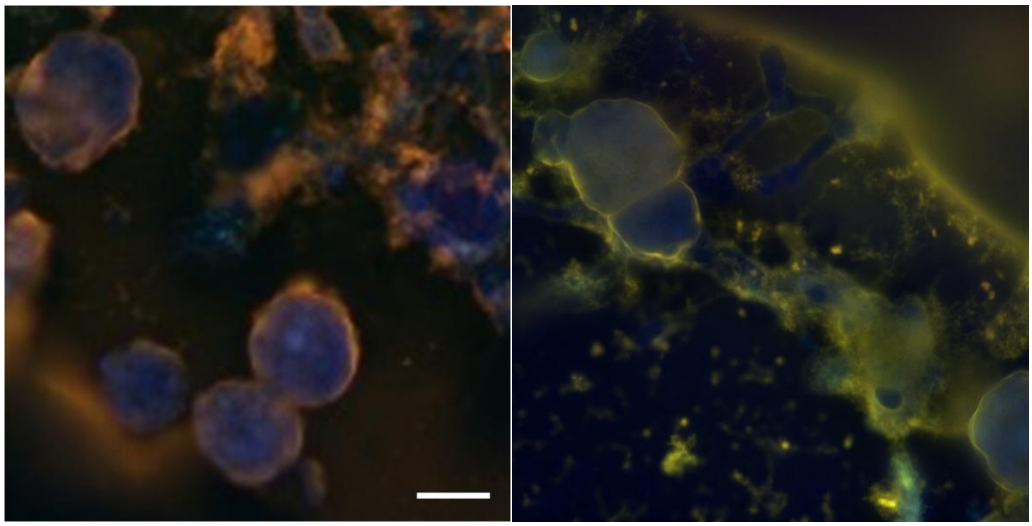

Figure 56: Micrographs of RWPE-1 grown on native reconstituted basement membrane (rBM) incubated with Rhodamine Concanavalin A (red channel) and AQA-F (blue channel for total probe and green channel for Zn^{2+}-bound probe). Scale bar = 50 µM.

AQA-F was shown to be internalised by native 3D RWPE-1 cultures, evidenced by the presence of intracellular blue fluorescence seen in **Figure 56**. Upon closer inspection, it was difficult to determine the intracellular concentrations of Zn^{2+} due to a lack of visible green fluorescence in the overlay image of all the channels. When consulting the green channel in isolation, the green fluorescence was more distinguished. However, the bleed through between the red and green channels was present in the same manner as the 2D models further supporting the limitations of the high throughput microscope with this probe. Upon incubation with a 1 mM zinc chloride solution, a similar phenomenon was expected as the 2D model whereby incubating with zinc increased the intracellular concentrations of Zn^{2+} allowing for a greater amount of green emission. **Figure 56B** however appears to possess no significant difference in green fluorescence compared to **Figure 56A**. This could suggest that the homeostasis of zinc is modified during the formation of acini or this could be a result of limitations with the microscope.

Following the co-localisation study performed on the 3D acini, it was important to gain structural information to confirm the model had worked. As discussed previously, confocal microscopy could be used to obtain this information. A z-stack of 20 slices at 2 µM thick was performed and is shown in **Figure 57**. This image shows 3D RWPE-1 cells that have been stained with Rhodamine Concanavalin A and AQA-F, with **Figure 57B** being incubated with a 1 mM zinc chloride solution. When consulting these images, it is evident that there is no fluorescence in the blue or green fluorescence channels suggesting that AQA-F had not been excited at the correct wavelength. Rhodamine Concanavalin A however had localised to the cell membrane and can be seen in the images in the red channel. The two large rings in the centre of the image represent a

cross section of the 3D structure, whereas on the left hand side and the bottom a section is observed in the z-plane. When looking at this z-plane, rings can be seen that suggest the formation of a 3D structure. Due to limitations of the microscope, only half of the acini was successfully imaged resulting in a cup-shaped structure. If these technical limitations were overcome and the overall structure of the acini was imaged as a whole, a 3D uniform spherical structure is expected.

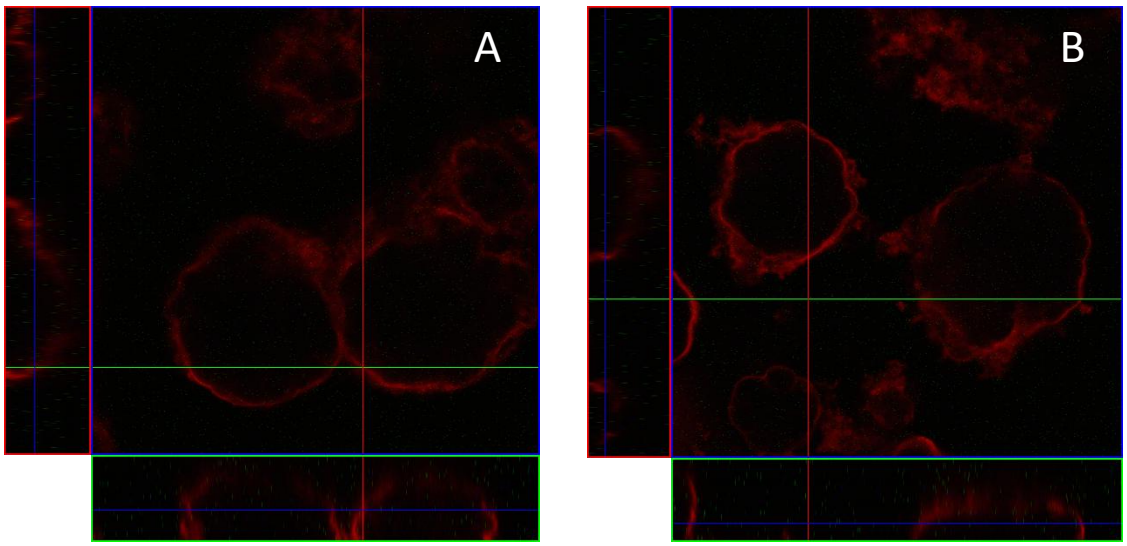

Figure 57: Two micrographs showing a z-stack of RWPE-1 acini that have been incubated with Rhodamine Concanavalin A (a red cell membrane stain). Micrograph B is taken from RWPE-1 acini that were incubated overnight with a 1 mM zinc chloride solution.

4.0. CONCLUSION

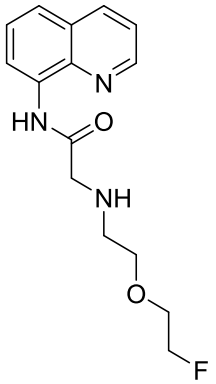

Figure 58: Chemical structure for AQA-F (8).

AQA-F (**Figure 58**), a fluorescent zinc sensing probe that shows ratiometric fluorescence upon zinc binding, has successfully been synthesised and its potential as an *in vitro* imaging probe has been validated.

A method of synthesis has been developed that yields AQA-F, an aminoquinoline-based probe, in 15% yield over 4 steps from 2-fluoroethanol. AQA-F forms a complex with zinc in a 1:1 ratio with a determined K_d of 14×10^{-6} M. Upon zinc binding a bathochromic shift of 80 nm and a 6 fold increase in fluorescence intensity is observed. This will allow for the *in vitro* differentiation of zinc bound and free probe. This fluorescence response appears to be specific for zinc, as other biologically relevant metals tested did not have a significant fluorescence response and therefore allows the probe to be translated into *in vitro* studies where the localisation and uptake of the probe can be assessed. Furthermore, this probe has a greater affinity for zinc binding than other metals, in contrast to the previously reported AQA-OH.

The optimum dose (100 μM) and incubation times (30 minutes) of AQA-F have been determined in healthy prostate cells allowing for the greatest fluorescence intensity

during *in vitro* applications. The probe has been shown to be non-toxic at imaging concentrations in healthy prostate, prostate cancer and normal tissues over a period of 24 hours. AQA-F has been shown to be internalised by healthy prostate and prostate cancer cell lines across both 2D and 3D models. This research sets the foundation for a zinc sensing probe that has the ability to be utilised for the diagnosis of prostate cancer. Furthermore, successful radiolabelling would result in a dual modal probe for increased diagnostic potential.

5.0. LIMITATIONS AND FUTURE WORK

The *in vitro* validation of AQA-F was limited during this study due to the low excitation wavelength. This problem is commonly associated with quinoline-derivatives and will need to be addressed for potential *in vivo* applications. An optimal laser was not available to excite AQA-F during confocal microscopy for this study. This prevented in-depth co-localisation studies from being performed, therefore a high throughput fluorescence microscope was utilised which produced images with bleed through between channels. This could be overcome in the future by using a laser that excites at a lower wavelength that would be more appropriate for AQA-F. Another method involves modifying the probe to incorporate a fluorophore that can be excited at a higher wavelength. This could be achieved by implementing a fluorophore such as Rhodamine, or could be through modification of the electronics of the aminoquinoline unit to produce a higher excitation maximum.

When imaging the acini using the confocal microscope, due to technical limitations, only the lower half of the acini was imaged. This produced a z-stack which showed the formation of a cup-shape, whereas with sufficient imaging this cup could be fully

imaged which may have suggested the overall shape of a uniform spherical acini. However, due to these technical limitations the overall shape of the 3D structure could not be determined. These limitations could be rectified in the future which would allow for further validation of the zinc-sensing probe, AQA-F.

When performing *in vitro* fluorescence studies, it was important to have a healthy prostate, prostate cancer and control cell line, however the cell lines that were used were chosen based on availability. This limited the study as the cell lines intracellular Zn^{2+} concentrations were not properly quantified, instead these concentrations were just assumed as high or low based on the zinc in prostate cancer model reported by Franklin *et al*, 2005.

One possible way to improve AQA-F for *in vivo* studies is by radiolabelling it with ^{18}F. A HPLC for analysis of AQA-F was performed and is shown in **Figure 59**. The ligand was shown to elute at 11 minutes; this will allow for radiochemical yield and purity to be assessed following radiolabelling. One possible radiolabelling method involves the synthesis of AQA-OH probe which can then be mesylated as reported by Stasiuk *et al*, 2015. This AQA derivative can then be reacted with ^{18}F-kryptofix to yield the hot analogue of AQA-F.

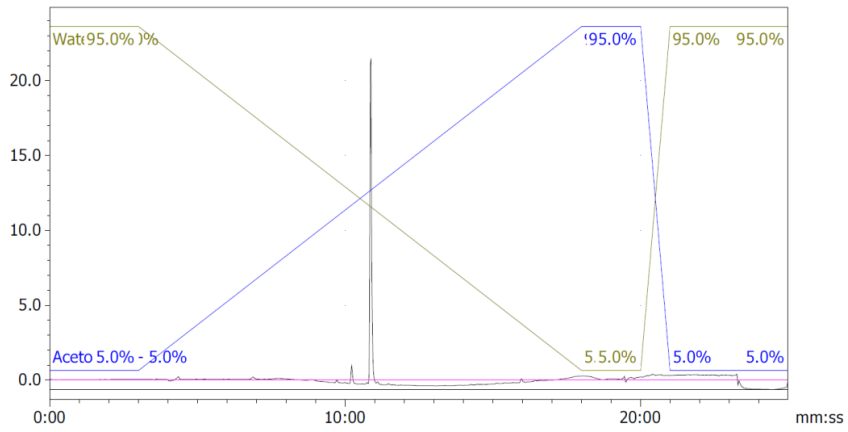

Figure 59: A HPLC for AQA-F.

6.0. REFERENCES

Afshar-Oromieh, A., Avtzi, E., Giesel, F.L., Holland-Letz, T., Linhart, H.G., Eder, M., Eisenhut, M., Boxler, S., Hadaschik, B.A., Kratochwil, C., Weichert, W., Kopka, K., Debus, J., Haberkorn, U. (2015) The diagnostic value of PET/CT imaging with the 68Ga-labelled PSMA ligand HBED-CC in the diagnosis of recurrent prostate cancer. *European Journal of Nuclear Medicine and Molecular Imaging.* **42**(2):197-209.

Afshar-Oromieh, A., Malcher, A., Eder, M., Eisenhut, M., Linhart, H.G., Hadaschik, B.A., Holland-Letz, T., Giesel, F.L., Kratochwil, C., Haufe, S., Haberkorn, U., Zechmann, C.M. (2013) PET imaging with a [68Ga]gallium-labelled PSMA ligand for the diagnosis of prostate cancer: biodistribution in humans and first evaluation of tumour legions. *European Journal of Nuclear Medicine and Molecular Imaging.* **40**(4):486-95.

Afshar-Oromieh, A., Zechmann, C.M., Malcher, A., Eder, M., Eisenhut, M., Linhart, H. G., Holland-Letz, T., Hadaschik, B.A., Giesel, F.L., Debus, J., Haberkorn, U. (2014). Comparison of PET imaging with a ^{68}Ga-labelled PSMA ligand and ^{18}F-choline-based PET/CT for the diagnosis of recurrent prostate cancer. *European Journal of Nuclear Medicine and Molecular Imaging*. **41**(1), 11–20.

Alberts, B., Johnson, A., Lewis, J., Raff, M., Roberts, K., Walter, P. (2002) Molecular biology of the cell. New York: Garland Science.

Amatemey, S.M., Honer, M., Schubiger, A.P. (2008) Molecular Imaging with PET. *Chemical Reviews.* **108**(5):1501-16.

Asabella, A.N., Cascini, G.L., Paparella, D., Notaristefano, A., Rubini, G. (2014) The copper radioisotopes: a systematic review with special interest to ^{64}Cu. *BioMed Research International.* **2014**:9.

Bernard-Gauthier, V., Bailey, J.J., Aliaga, A., Kostikov, A., Rosa-Neto, P., Wuest, M., Brodeur, G.M., Bedell, B.J., Wuest, F., Schirrmacher, R. (2015) Development of subnanomolar radiofluorinated (2-pyrrolidin-1-yl)imidazoij1,2-b]pyridazine pan-Trk inhibitors as candidate PET imaging probes†. *Med. Chem. Commun.***6**(12):2184-93.

Bertrand, G., Vladesco, R. (1921) Intervention probable du zinc dans les phénomènes de fécondation chez les animaux vertébrés. *C. R. Acad. Sci.* 173-176.

Botchorishvili, G., Matikainen, M.P., Lilja, H. (2009) Early prostate-specific antigen changes and the diagnosis and prognosis of prostate cancer. *Current Opinion in Urology.***19**(3):221-6.

Bouchelouche, K., Tagawa, S.T., Goldsmith, S.J., Turkbey, B., Capala, J., Choyke, P. (2011) PET/CT imaging and radioimmunotherapy of prostate cancer. *Seminars in Nuclear Medicine.* **41**(1):29-44.

Briganti, A., Giannarini, G., Klatte, T., Catto, J.W., Shariat, S.F. (2015) The future of prostate cancer diagnosis: biomarkers, biopsy, both or neither? *European Urology Focus.* **1**(2):97-98.

Brzóska, M.M., Moniuszko-Jakoniuk, J. (2001) Interactions between cadmium and zinc in the organism. *Food and Chemical Toxicology.* **39**(10):967-80.

Buccella, D., Horowitz, J.A., Lippard, S.J. (2011) Understanding zinc quantification with existing and advanced ditopic fluorescent zinpyr sensors. *Journal of the American Chemical Society.* **133**(11):4101-14.

Burdette, S.C., Walkup, G.K., Spingler, B., Tsien, R.Y., Lippard, S.J.J. (2001) Fluorescent sensors for Zn2+ based on a fluorescein platform: synthesis, properties and intracellular distribution. *Journal of the American Chemical Society.* **123**(32):7831-41.

Carabineiro, S.A., Silva, L.C., Gomes, P.T., Pereira, L.C.J., Veiros, L.F., Pascu, S.I., Duarte, M.T., Namorado, S., Henriques, R.T. (2007) Synthesis and characterization of tetrahedral and square planar bis(iminopyrrolyl) complexes of cobalt(II). *Inorganic Chemistry*. **46**:6880-90.

Charles-Edwards, E.M., deSouza, N.M. (2013) Diffusion-weighted Magnetic Resonance Imaging and its Application to Cancer. *Cancer Imaging.* **13**(6):135-43.

Chen, Z.-Y., Wang, Y.-X., Lin, Y., Zhang, J-S., Yang, F., Zhou, Q.-L., & Liao, Y-Y. (2014). Advance of Molecular Imaging Technology and Targeted Imaging Agent in Imaging and Therapy. *BioMed Research International*. **2014**(12):1-12.

Costello, L.C., Franklin, R.B. (2006a) Concepts of citrate production and secretion by prostate metabolic relationships. *The Prostate.* **18**(1):25-46.

Costello, L.C., Franklin, R.B. (2006b) The clinical relevance of the metabolism of prostate cancer; zinc and tumour suppression: connecting the dots. *Molecular Cancer.* **5**(17):1-13.

Costello, L.C., Franklin, R.B. (2009) Prostatic fluid electrolyte composition for the screening of prostate cancer: a potential solution to a major problem. *Prostate cancer and prostatic diseases.* **12**(1):17-24.

Costello, L.C., Franklin, R.B. (2011) Zinc is decreased in prostate cancer: an established relationship of prostate cancer! *Journal of Biological Inorganic Chemistry.* **16**(1):3-8.

Cuzick, J., Thorat M.A., Andriole, G., Brawley, O.W., Brown, P.H., Culig, Z., Eeles, R.A., Ford, L.G., Hamdy, F.C, Holmberg, L., Ilic, D., Key, T.J., Vecchia, C.L., Lilja, H., Marberger, M., Meyskens, F.L., Minasian, L.M., Parker, C., Parnes, H.L., Perner, S., Rittenhouse, H., Schalken, J., Schmid, H.-P., Schmitz-Dräger, B.J., Schröder, F.H., Stenzl, A., Tombal, B., Wilt, T.J., Wolk, A. (2014) Prevention and early detection of prostate cancer. *The Lancet Oncology.* **15**(11):484-92.

Debaene, F., Da Silva, J.A., Pianowski, Z., Durran, F.J., Winssinger, N. (2007) Expanding the scope of PNA-encoded libraries: divergent synthesis of libraries targeting cysteine, serine and metallo-proteases as well as tyrosine phosphatises. *Tetrahedron.* **63**(28):6577-86.

Dietlein, M., Kobe, C., Kuhnert, G., Stockter, S., Fischer, T., Schomäcker, K., Schmidt, M., Dietlein, F., Zlatopolskiy, B.D., Krapf, P., Richarz, R., Neubauer, S., Drzezga, A., Neumaier, B. (2015) Comparison of [^{18}F]DCFPyL and [^{68}Ga]Ga-PSMA-HBED-CC for PSMA-PET imaging in patients with relapsed prostate cancer. *Molecular Imaging in Biology.* **17**(4):575-84.

Elsinga, P.H. (2002) Radiopharmaceutical chemistry for positron emission tomography. *Methods.* **27**(3):208-17.

Eskicorapci, S.Y., Baydar, D.E., Akbal, C., Sofikerim, M., Günay, M., Ekici, S., Ozen, H. (2004) An extended 10-core transrectal ultrasonography guided prostate biopsy protocol improves the detection of prostate cancer. *European Urology.* **45**(4):444-9.

Firth, G. (2016) The Development of Multimodal PET/Fluorescence Zinc Sensors as Potential Imaging Agents for Prostate Cancer. Unpublished.

Frangioni, J.V. (2003) *In vivo* near-infrared fluorescence imaging. *Current Opinion in Chemical Biology.* **7**(5):626-34.

Franklin, R. B., Feng, P., Milon, B., Desouki, M. M., Singh, K. K., Kajdacsy-Balla, A., Costello, L. C. (2005) hZIP1 zinc uptake transporter down regulation and zinc depletion in prostate cancer. *Molecular Cancer*, **4**(32):1-13.

Franz, M.-C., Anderle, P., Bürzle, M., Suzuki, Y., Freeman, M.R., Hediger, M.A., Kovacs, G. (2013) Zinc Transporters in Prostate Cancer. *Molecular Aspects of Medicine.* **34**(2-3):735-741.

Gaffield, M.A., Betz, W.J. (2006) Imaging Synaptic Vesicle Exocytosis and Endocytosis with FM dyes. *Nature Protocols.* **1**(6):2916-21.

Ghosh, S. K., Kim, P., Zhang, X., Yun, S.-H., Moore, A., Lippard, S. J., Medarova, Z. (2010) A Novel Imaging Approach for Early Detection of Prostate Cancer Based on Endogenous Zinc Sensing. *Cancer Research,* **70**(15): 6119–6127.

Gleason, D.P., Mellinger, G.T. (1974) Prediction of Prognosis for Prostatic Adenocarcinoma by Combined Histological Grading and Clinical Staging. *The Journal of Urology.* **111**(1):58-64.

Gordetsky, J., Epstein, J. (2016) Grading of Prostatic Adenocarcinoma, Current State and Prognostic Implications. *Diagnostic Pathology.* **11**: 25.

Hanahan, D., Weinburg, R.A. (2011) Hallmarks of cancer: the next generation. *Cell.* **144**(5):646-74.

Hernandez, D.J., Nielsen, M.E., Han, M., Partin, A.W. (2007) Contemporary Evaluation of the D'Amico Risk Classification of Prostate Cancer. *Urology.* **70**(5):931-5.

Hoh, C.K. (2007) Clinical use of FDG PET. *Nuclear Medicine and Biology.* **34**(7):737-42.

Hong, S.K. (2014) Kallikreins as Biomarkers for Prostate Cancer. *BioMed Research International.* **2014**:1-10.

Huang, Z., Lippard, S.J. (2012) Illustrating mobile zinc with fluorescence: from cuvettes to live cells and tissue. *Methods in Enzymology.* **505**(1):445-68.

Humphrey, P.A. (2004) Gleason Grading and Prognostic Factors in Carcinoma of the Prostate. *Modern Pathology.* **17**(3):292-306.

Koh, D.M., Collins, D.J. (2007) Diffusion-weighted MRI in the body: applications and challenges in oncology. *American Journal of Roentgenology.* **188**(6):1622-35.

Kolenko, V., Teper, E., Kutikov, A., & Uzzo, R. (2013) Zinc and zinc transporters in prostate carcinogenesis. *Nature Reviews Urology.* **10**(4), 219–226.

Komatsu, K., Kikuchi, K., Kojima, H., Urano, Y., Nagano, T. (2005) Selective zinc sensor molecules with various affinities for Zn2+, revealing dynamics and regional distribution of synaptically released Zn2+ in hippocampal slides. *Journal of the American Chemical Society.* **127**(29):10197-204.

Kumar, V.L., Majumder, P.K. (1995) Prostate Gland: Structure, Functions and Regulation. *International Urology and Nephrology.* **27**(3):231-43.

Laverdant, J., de Marcillac, W.D., Barthous, C., Chinh, V.D., Schwob, C., Coolen, L., Benalloul, P., Nga, P.T., Maitre, A. (2011) Experimental determination of thje fluorescence quantum yield of semiconductor nanocrystals. *Materials.* **4**:1182-93.

Li, C., Conti, P.S. (2010) Radiopharmaceutical chemistry for positron emission tomography. *Advanced Drug Delivery Reviews.* **62**(11):1031-1051.

Li, D., Liu, L., Li, W-H. (2015) Genetic targeting of a small fluorescent zinc indicator to cell surface for monitoring zinc secretion. *ACS Chemical Biology.* **10**(4):1054-63.

Li, X., Yang, W., Zou, Y., Meng, F., Deng, C., Zhong, Z. (2015) Efficacious delivery of protein drugs to prostate cancer cells by PSMA-targeted pH-responsive chimaeric polymersomes. *Journal of Control Release.* **220**(Pt B):704-14.

Lilja, H., Ulmert, D., Vickers, A.J. (2008) Prostate-specific antigen and prostate cancer: prediction, detection and monitoring. *Nature Reviews Cancer.* **8**(4):268-78.

Lindenberg, L., Choyke, P., Dahut, W. (2016) Prostate cancer imaging with novel PET tracers. *Current Urology Reports.* **17**:18.

Marcu, L. (2012) Fluorescence lifetime techniques in medical applications. *Annals of Biomedical Engineering.* **40**(2):304-331.

Maurer, T., Eiber, M., Schwaiger, M., Gschwend, J.E. (2016) Current use of PSMA-PET in prostate cancer management. *Nature Reviews Urology.* **13**(4):226-35.

McNeal, J.E. (1981) The zonal anatomy of the prostate. The *Prostate.* **2**(1):35-49.

Miller, P.W., Long, N.J., Gee, A.D. (2008) Synthesis of 11C, 18F, 15O and 13N Radiolabels for Positron Emission Tomography. *Angewandte Chemie International Edition.* **47**(47):8998-9033.

Mindell, J.A. (2012) Lysosomal acidification mechanisms. *Annual Review in Physiology.* **74**:69-86.

Nash, A.F., Melezinek, I. (2000) The role of prostate specific membrane antigen measuremeint in the detection and management of prostate cancer. *Endocrine-Related Cancer,* **7**, 37-51.

Pawley, J. (2006) Handbook of Biological Confocal Microscopy. New York, NY: Springer.

Perry, J. C., Sirot, L., & Wigby, S. (2013) The seminal symphony: how to compose an ejaculate. *Trends in Ecology & Evolution*, ***28***(7), 414–22.

Pons, J., Garcia-Anton, J., Jimenez, R., Solans, X., Font-Bardia, M., Ros, J. (2007) Preparation and structural characterisation of a Cd(II) complex with unusual geometry. *Inorganic Chemistry Communications*. **10**(12):1554-6.

Potter, S.R., Partin, A.W. (2000) Hereditary and Familial Prostate Cancer: Biologic Aggressiveness and Recurrence. *Reviews in Urology.* **2**(1):35-6.

Presti, J. C. (2007) Prostate Biopsy: Current Status and Limitations. *Reviews in Urology*. ***9***(3):93–8.

Rodriguez-Teja, M., Breit, C., Clarke, M., Talar, K., Wang, K., Mohammad, M.A., Pickwell, S., Etchandy, G., Stasiuk, G.J., Sturge, J. (2016) How to Study Basement Membrane Stiffness as a Biophysical Trigger in Prostate Cancer and Other Age-related Pathologies or Metabolic Diseases. *Journal of Visualized Experiments.* (115), e54230.

Rodriguez-Teja, M., Gronau, J. H., Breit, C., Zhang, Y. Z., Minamidate, A., Caley, M. P., McCarthy, A., Cox, T. R., Erler, J. T., Gaughan, L., Darby, S., Robson, C., Mauri, F., Waxman, J. and Sturge, J. (2015) AGE-modified basement membrane cooperates with Endo180 to promote epithelial cell invasiveness and decrease prostate cancer survival. J. Pathol., **235**(4): 581–592.

Roesch, F., Riss, P.J. (2010) The renaissance of the 68Ge/68Ga radionuclide generator initiates new developments in 68Ga radiopharmaceutical chemistry. *Current Topics in Medicinal Chemistry.* **10**(16):1633-68.

Sauer, M., Hofkens, J., Enderlein, J. (2011) Handbook of Fluoroescence Spectroscopy and Imaging. From Ensemble to Single Molecules. Weinheim: Wiley-VCH.
Siegel, R., Naishadham, D., Jemel, A. (2013) Cancer statistics, 2013. *CA:A Cancer Journal for Clinicians.* **63**(1):11-30.

Sobin L.H., Gospodarowicz M.K., Wittekind C. (2010) TNM Classification of Malignant Tumors, International Union Against Cancer. 7th ed. Oxford: Wiley-Blackwell.

Standring, S., Gray, H. (2008) Gray's anatomy: the anatomical basis of clinical practice. Churchill Livingstone, Edinburgh. Xxiv, 1551 p.pp.

Stanfield, C.L. (2013) *Principles Of Human Physiology*. Boston: Pearson Education.

Stasiuk, G.J. (2010) Design and Synthesis of Novel Lanthanide Chelates for use in Magnetic Resonance Imaging (MRI).

Stasiuk, G.J., Minuzzi, F., Sae-Heng, M., Rivas, C., Juretschke, H.-p., Piemonti, L., Allegrini, P.R., Laurent, D., Duckworth, A.R., Beeby, A., Rutter, G.A., Long, N.J. (2015)

Dual-Modal Magnetic Resonance/Fluorescent Zinc Probes for Pancreatic B-Cell Mass Imaging. *Chemistry- A European Journal.* **21**(13):5023-5033.

Stricker, P.D. (2001) Prostate Cancer part 1. Issues in screening and diagnosis. *Medicine Today.* **2(**7):20-29.

Szabo, Z., Mena, E., Rowe, S.P., Plyku, D., Nidal, R., Esienberger, M.A., Antonarakis, E.S., Fan, H., Dannals, R.F., Chen, Y., Mease, R.C., Vranesic, M., Bhatnagar, A., Sgouros, G., Cho, S.Y., Pomper, M.G. (2015) Initial evaluation of [^{18}F]DCFPyL for prostate-specific membrane antigen (PMSA)-targeted PET imaging of prostate cancer. *Molecular Imaging and Biology.* **17**(4):565-74.

Tamada, T., Sone, T., Jo, Y., Yamamoto, A., Ito, K. (2013) Diffusion-weighted MRI and its Role in Prostate Cancer. *NMR in Biomedicine.* **27**(1):25-38.

Torre, L. A., Bray, F., Siegel, R. L., Ferlay, J., Lortet-Tieulent, J., Jemal, A. (2015) Global cancer statistics, 2012. CA: A Cancer Journal for Clinicians, **65**(2): 87-108.

Valuer, B. (2002) Molecular Fluorescence. Weinheim: Wiley-VCH.

Wadas, T.J., Wong, E.H., Weisman, G.R., Anderson, C.J. (2010) Coordinating radiometals of copper, gallium, indium, yttrium, and zirconium for PET and SPECT imaging of disease. *Chemical Reviews*. **110**(5):2858-902.

Walker, H.K., Hall, W.D., Hurst, J.W. (1990) Clinical Methods: The History, Physical, and Laboratory Examinations. 3rd edition. Boston: Butterworths.

Walkup, G.K., Burdette, S.C., Lippard, S.J., Tsien, R.Y. (2000) A new cell-permeable fluorescent probe for Zn^{2+}. *Journal of the American Chemical Society.* **122**(23):5644-5.

Williams, A.T.R., Winfield, S.A., Miller, J.N. (1983) Relative fluorescence quantum yields using a computer controlled luminescence spectrometer. *The Analyst*. **108**(1290):1067.

Xu, Z., Yoon, J., Spring, D.R. (2010) Fluorescent chemosensors for Zn^{2+}. *Chemical Society Reviews.* **39**: 1996-2006.

Zhang, X-A., Lovejoy, K.S., Jasanoff, A., Lippard, S.J. (2007) Water-soluble porphyrins as a dual-function molecular platform for MRI and fluorescence zinc sensing. *PNAS.* **104**(26):10780-5.

Zhang, Y., Guo, X., Si, W., Jia, L., Qian, X. (2008) Ratiometric and water-soluble fluorescent zinc sensor of carboxamidoquinoline with an alkoxyethylamino chain as receptor. *Organic Letters.* **10**(3):473-6.

Zhu, A., Marcus, D. M., Shu, H.-K. G., Shim, H. (2012) Application of Metabolic PET imaging in radiation oncology. *Radiation Research*. ***177***(4):436–48.

7.0. APPENDIX

6.1. Absorption Spectra

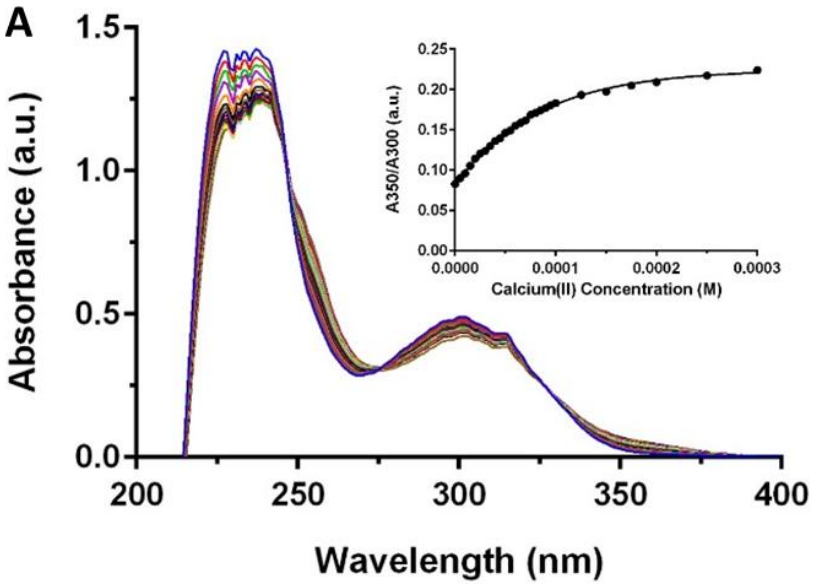

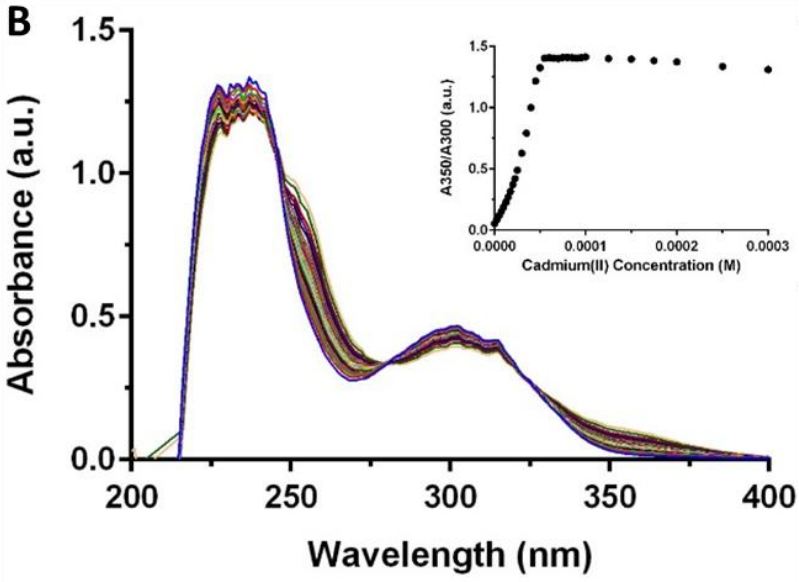

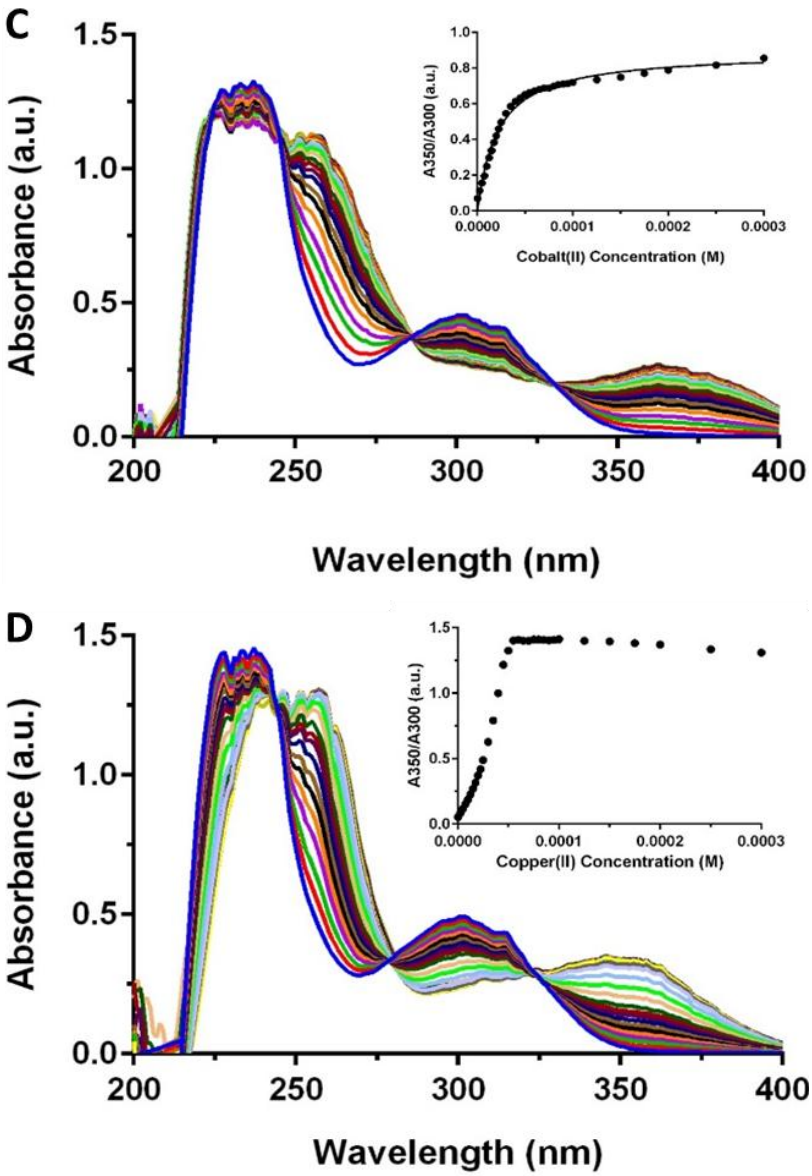
C
Absorbance (a.u.)
Wavelength (nm)
A350/A300 (a.u.)
Cobalt(II) Concentration (M)
D
Absorbance (a.u.)
Wavelength (nm)
A350/A300 (a.u.)
Copper(II) Concentration (M)

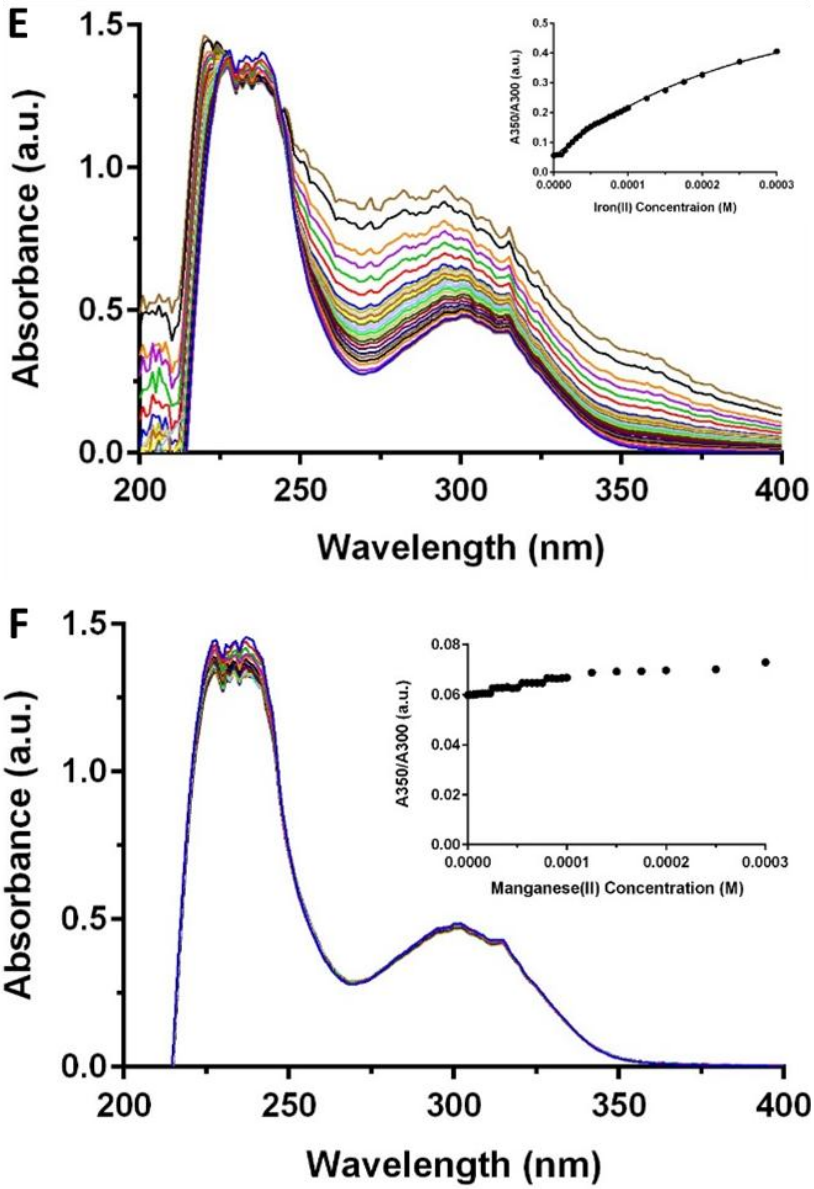
E
Absorbance (a.u.)
Wavelength (nm)
A350/A300 (a.u.)
Iron(II) Concentraion (M)
F
Absorbance (a.u.)
Wavelength (nm)
A350/A300 (a.u.)
Manganese(II) Concentration (M)

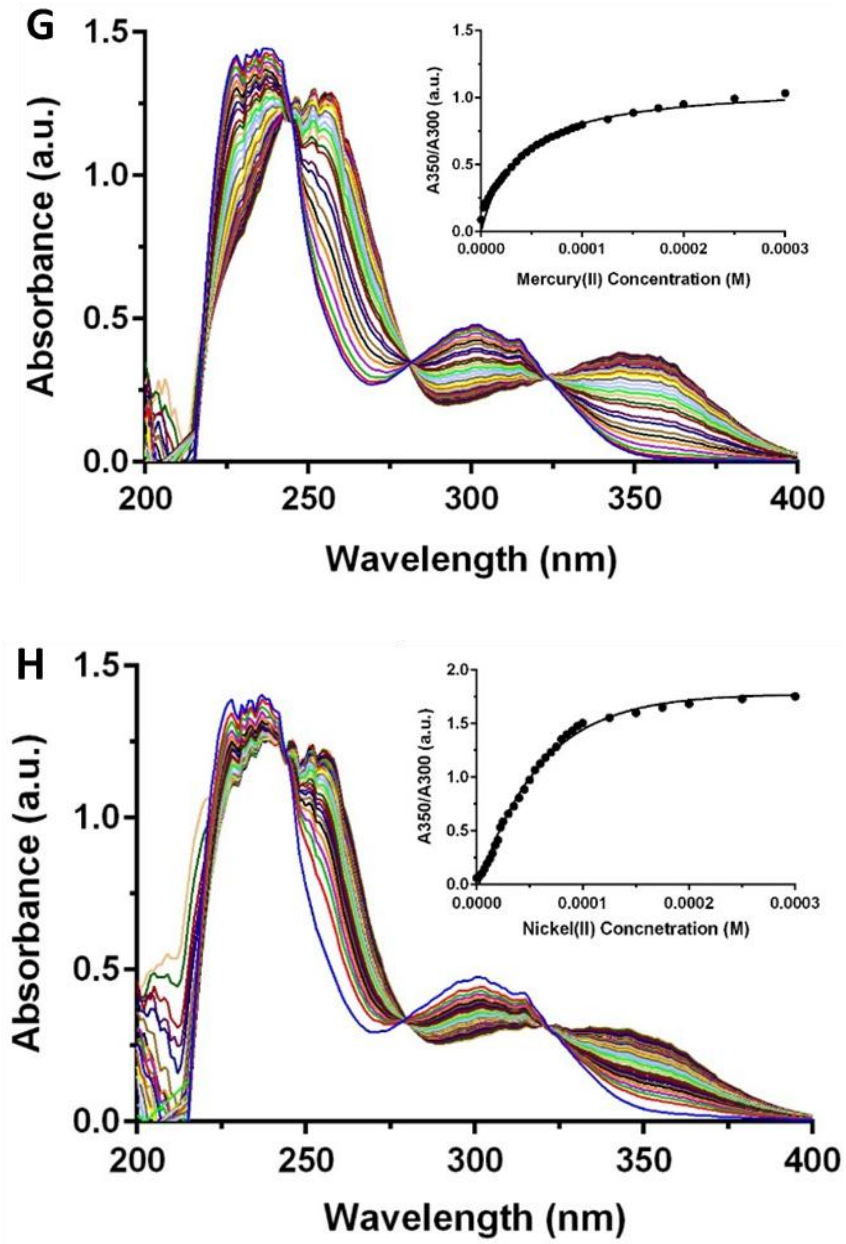

Appendix 1: Absorption spectra of AQA-F (0.1 mM) in HEPES buffer (10 mM, pH = 7.68) in the presence of different concentrations of Zn^{2+} (0-3 equiv). (Inset:) Ratiometric calibration curve A350/A300 nm as a function of metal concentration. A = Ca^{2+}, B = Cd^{2+}, C = Co^{2+}, D = Cu^{2+}, E = Fe^{2+}, F = Mn^{2+}, G = Hg^{2+}, H = Ni^{2+}.

6.2. Dose Response Fluorescence

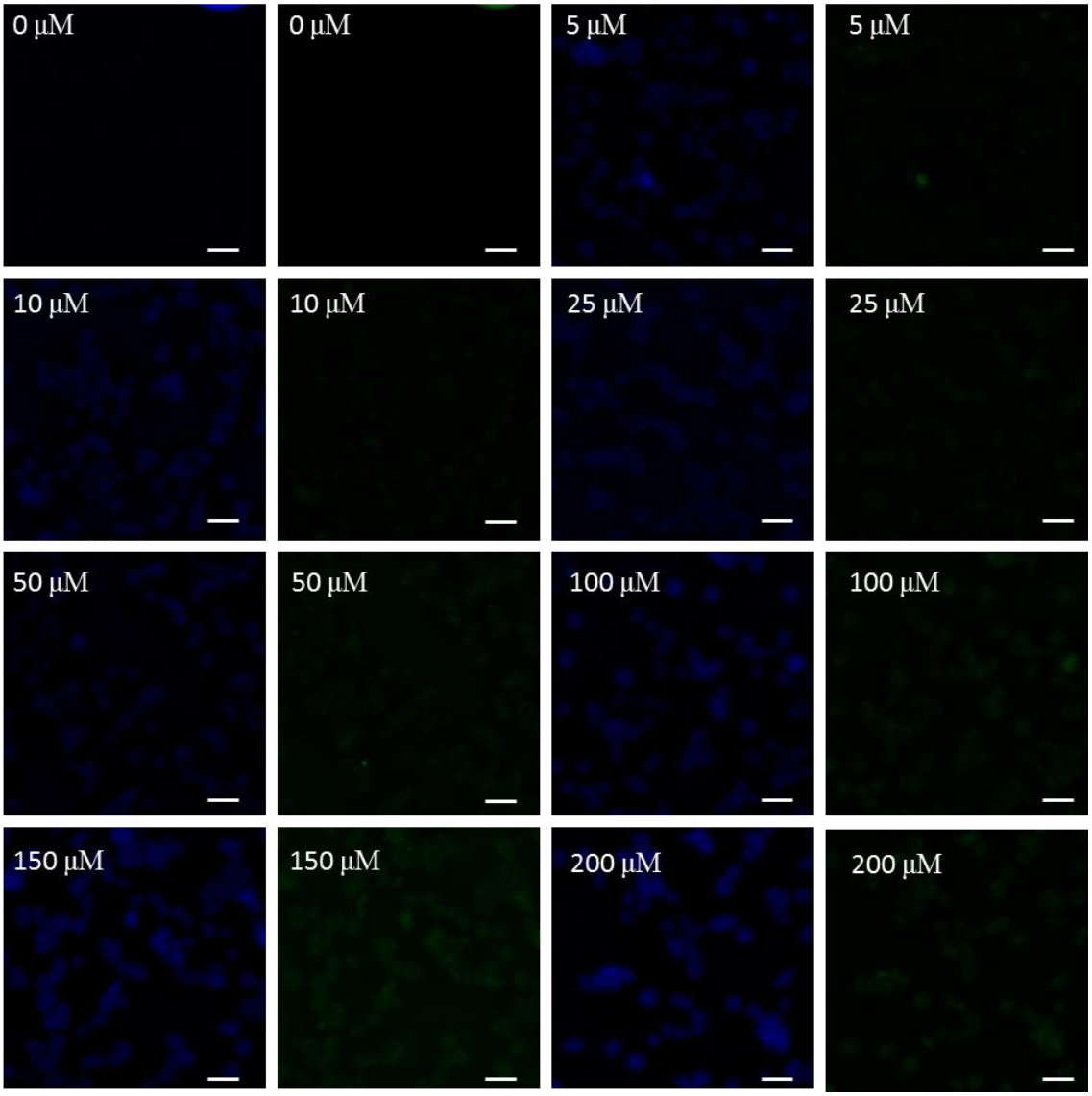

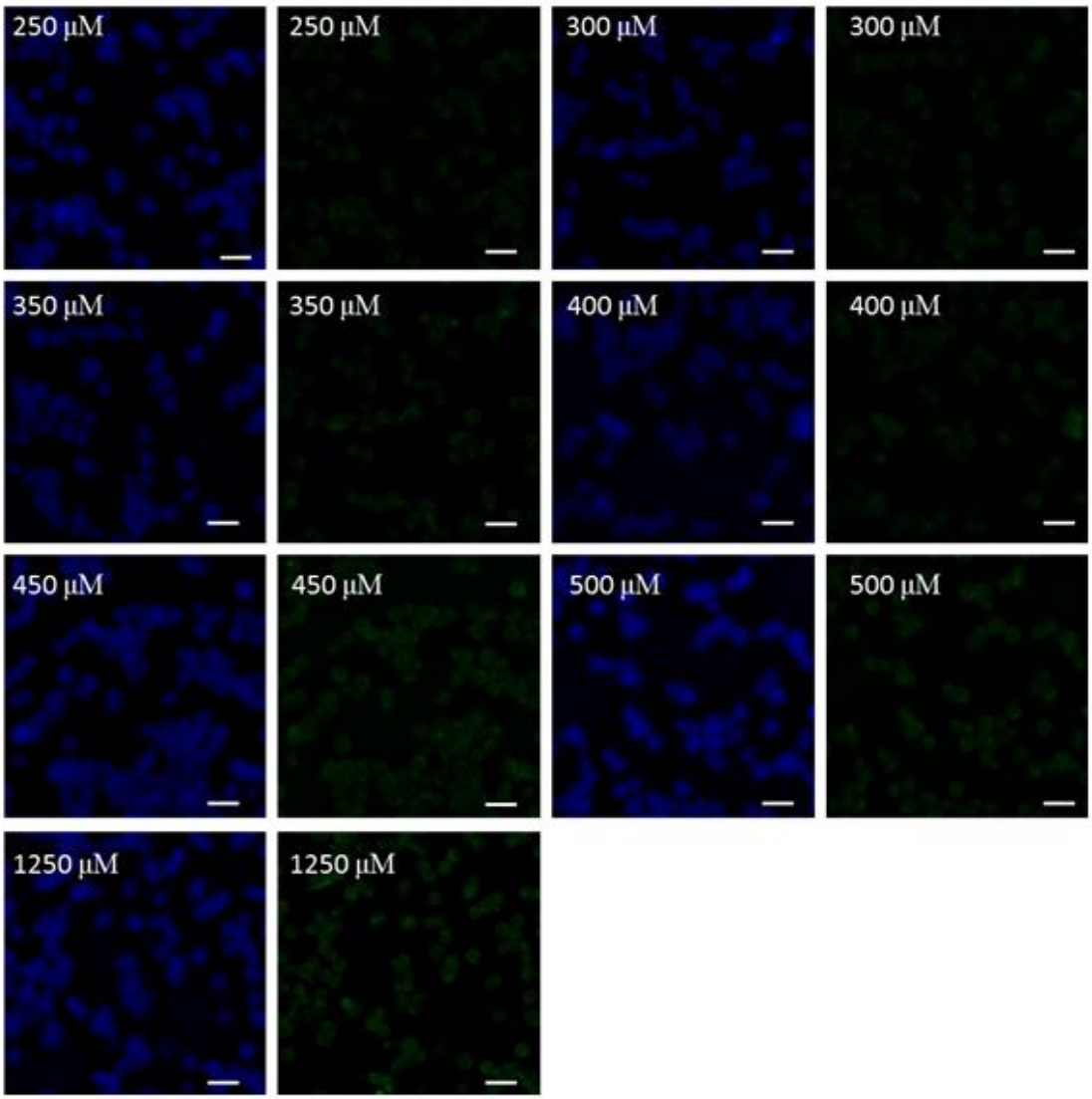

Appendix 2: A collection of micrographs obtained from incubating increasing concentrations (0-1250 µM) of AQA-F for 30 minutes with RWPE-1 cells. Scale bar = 20 µm.

6.3. Time Response Fluorescence

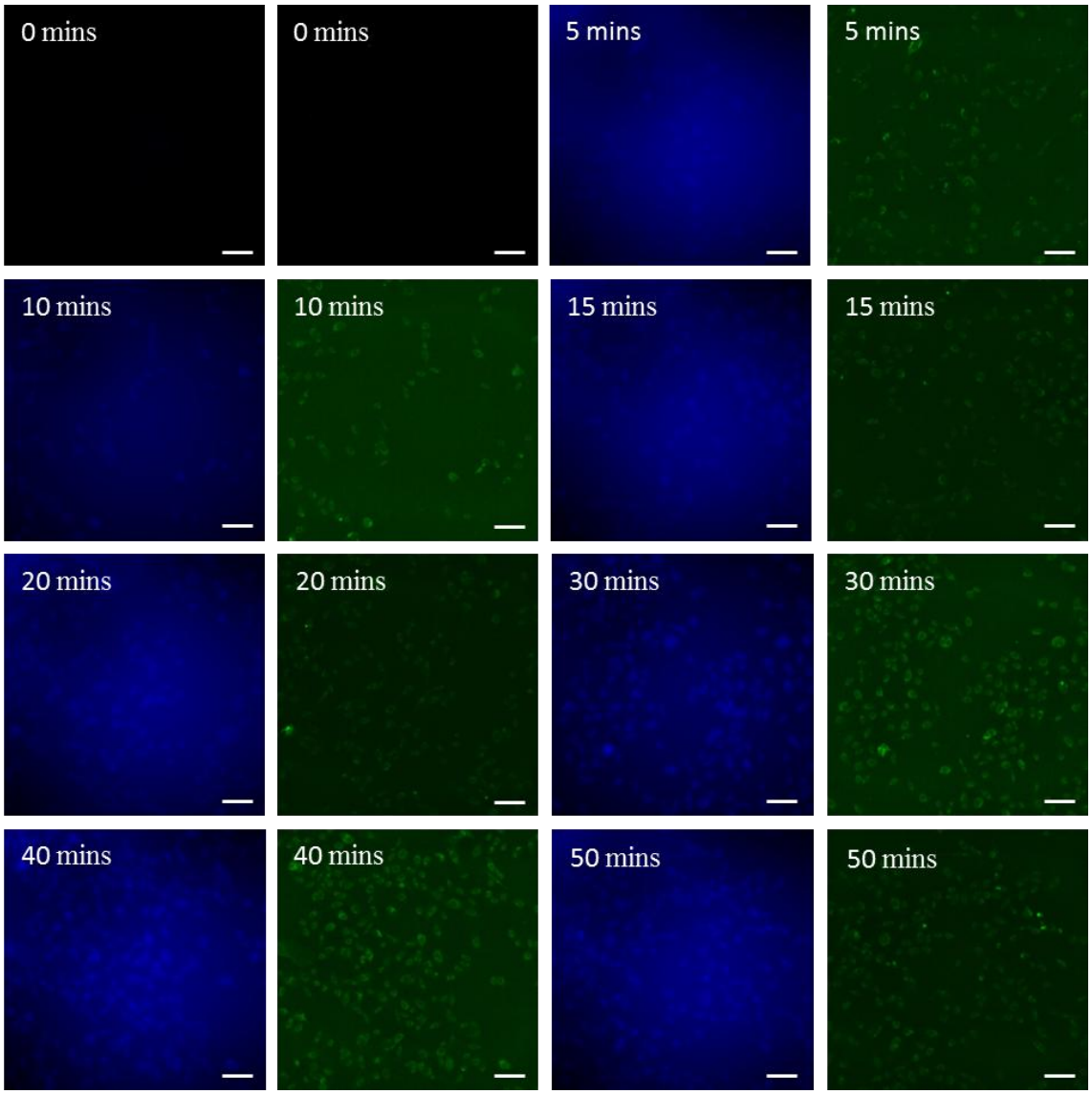

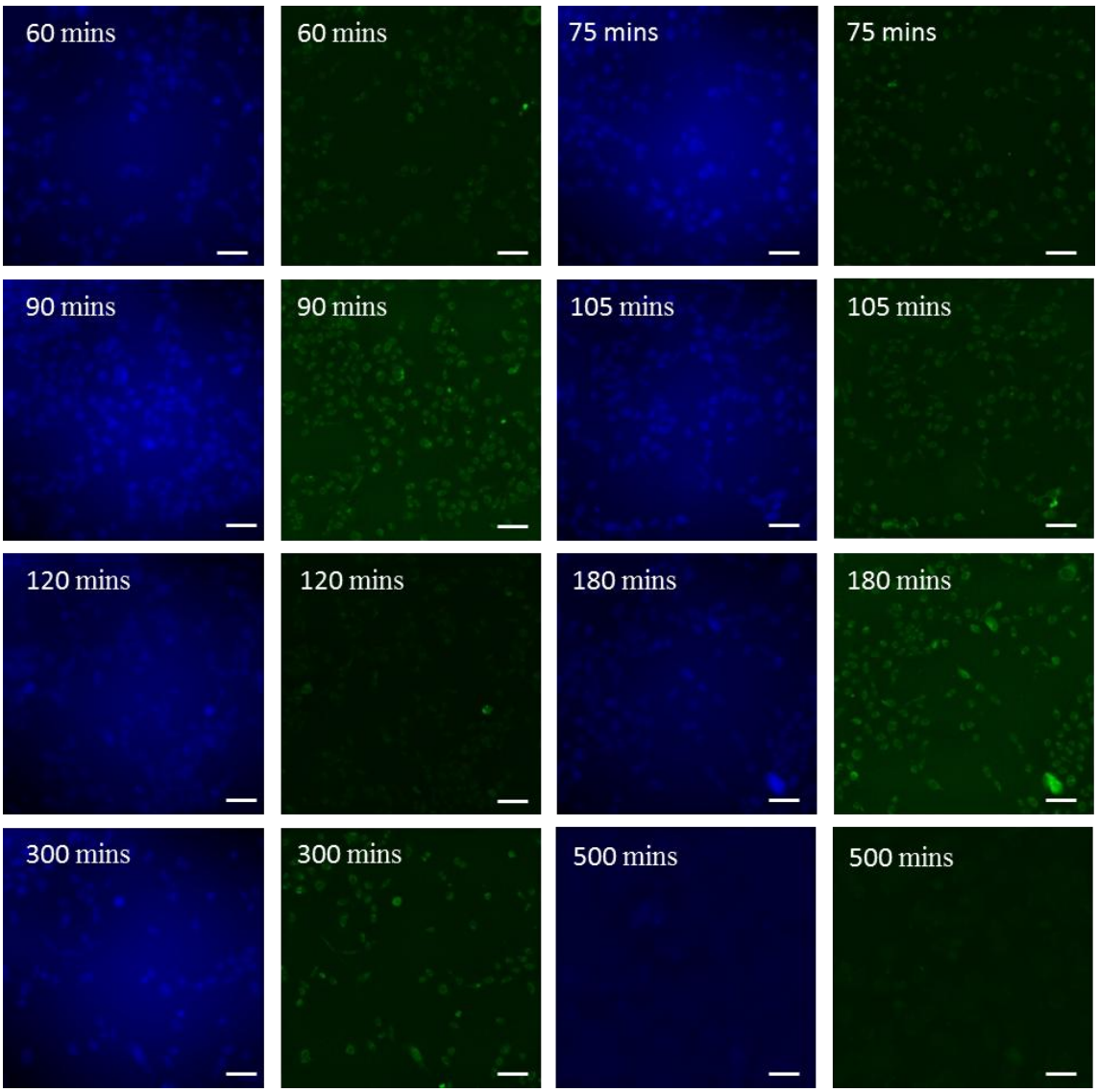

Appendix 3: A collection of micrographs obtained from incubating AQA-F (100 µM) for 0-500 minutes with RWPE-1 cells. Scale bar = 50 µm.

6.4. Co-localisation Fluorescence

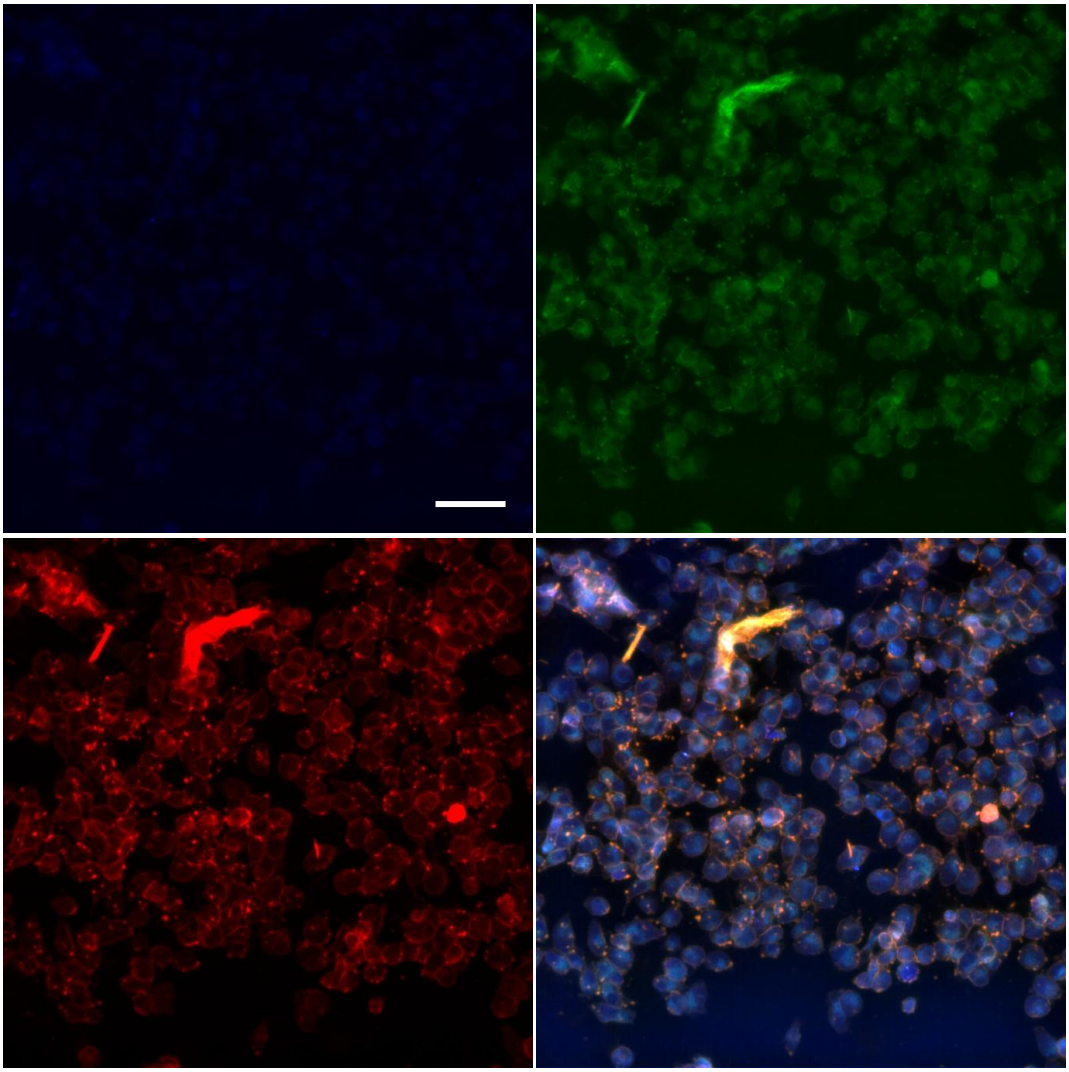

Appendix 4: A collection of micrographs obtained from incubating AQA-F (100 µM) and Rhodamine Concanavalin A for 30 minutes with RWPE-1 cells. Scale bar = 50 µm.

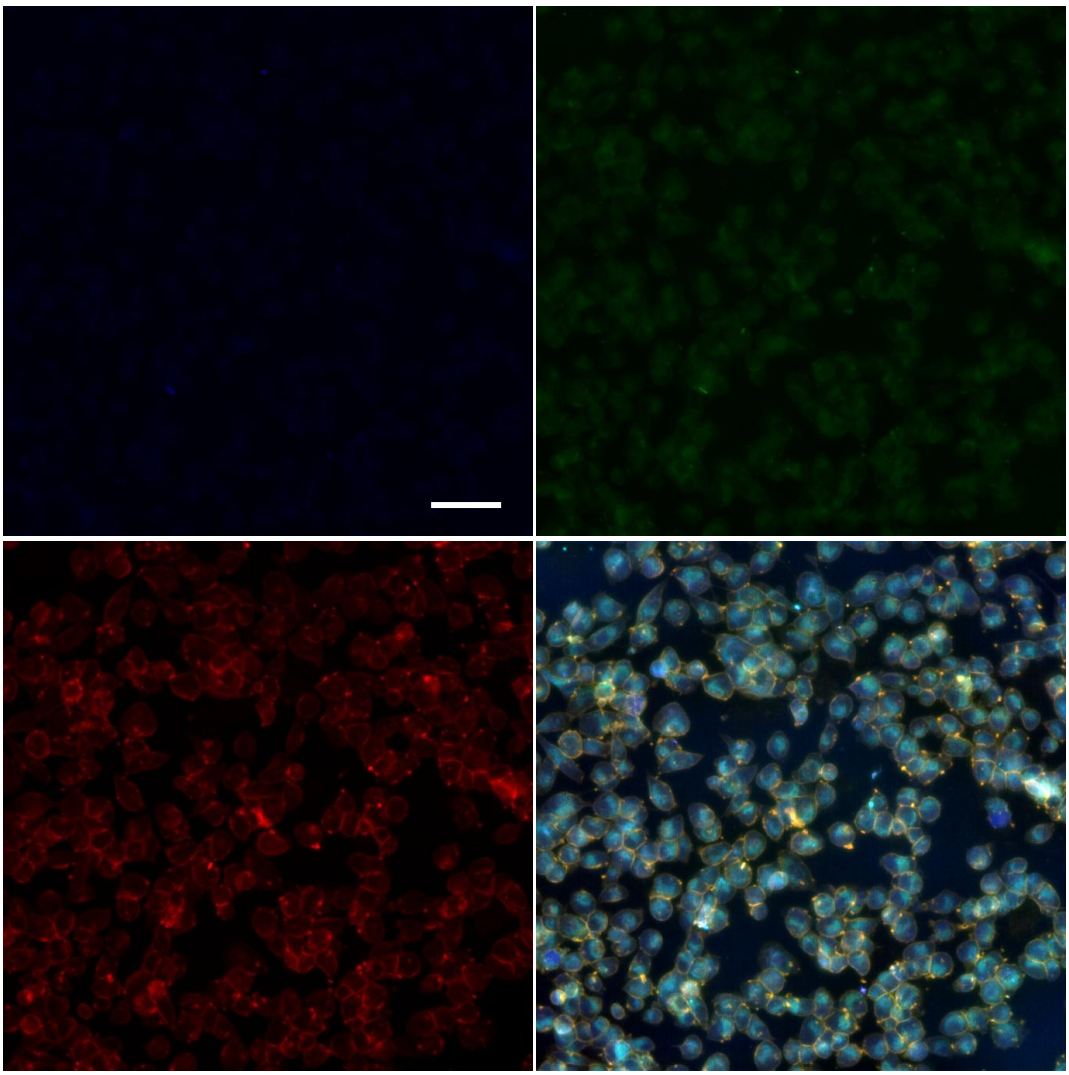

Appendix 5: A collection of micrographs obtained from incubating AQA-F (100 µM) and Rhodamine Concanavalin A for 30 minutes with RWPE-1 cells. These cells were also incubated overnight with a 1 mM zinc chloride solution prior to staining. Scale bar = 50 µm.

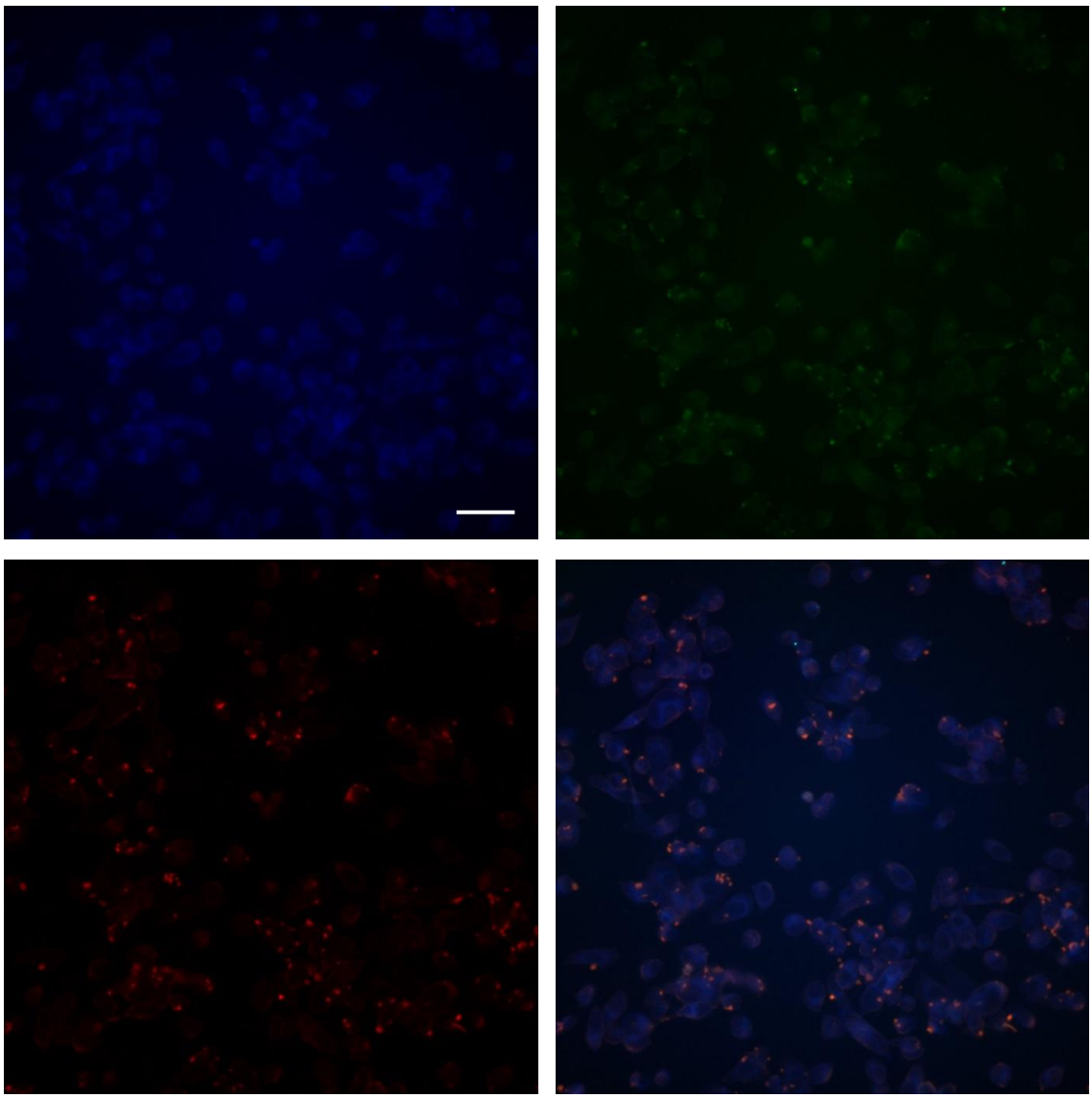

Appendix 6: A collection of micrographs obtained from incubating AQA-F (100 µM) and Rhodamine Concanavalin A for 30 minutes with PC-3 cells. Scale bar = 50 µm.

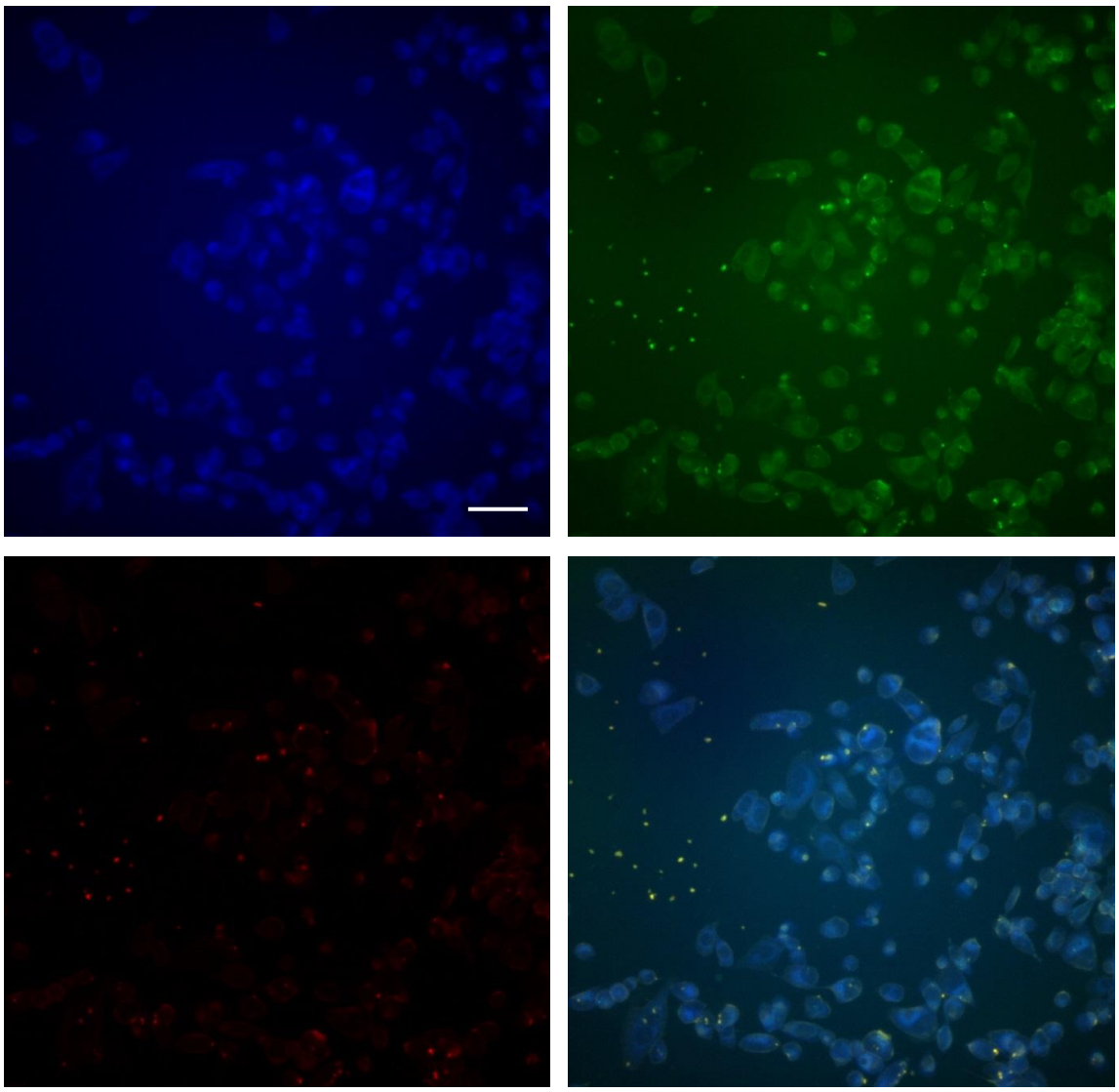

Appendix 7: A collection of micrographs obtained from incubating AQA-F (100 µM) and Rhodamine Concanavalin A for 30 minutes with PC-3 cells. These cells were also treated overnight with a 1 mM zinc chloride solution prior to staining. Scale bar = 50 µm.

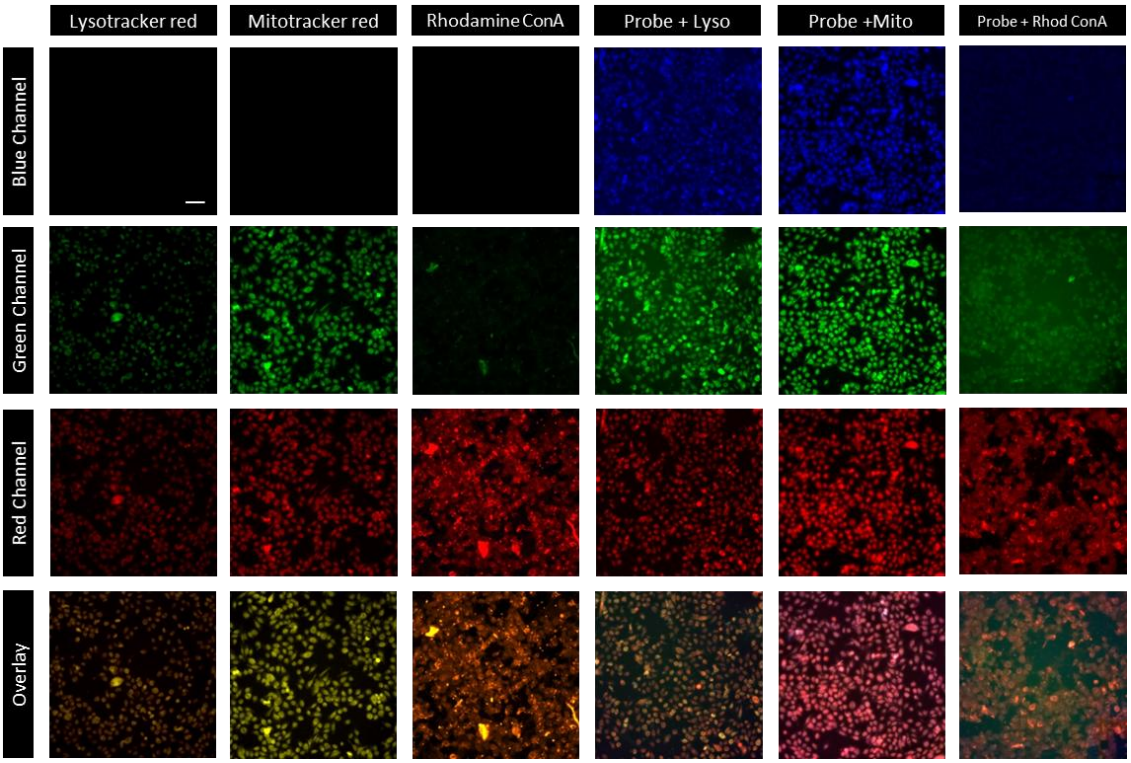

Appendix 8: A collection of micrographs obtained from incubating Lysotracker, Mitotracker, Rhodamine Concanavalin A and AQA-F (100 µM) for 30 minutes with RWPE-1 cells. Scale bar = 20 µm.

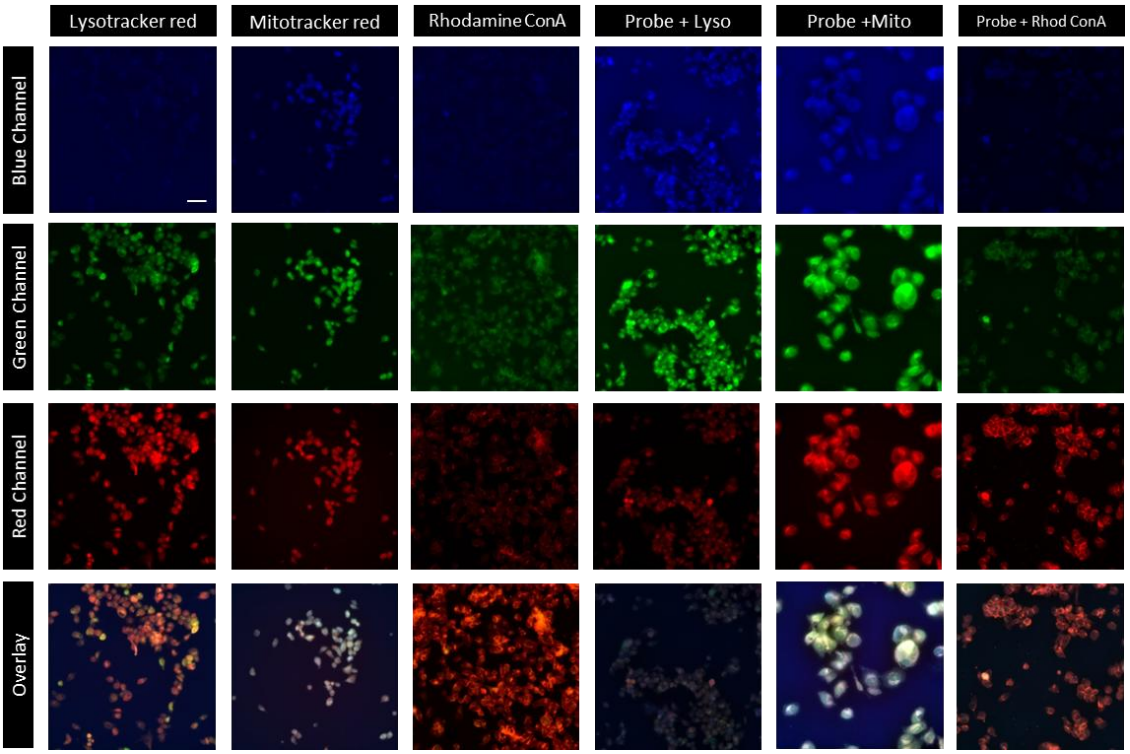

Appendix 9: A collection of micrographs obtained from incubating Lysotracker, Mitotracker, Rhodamine Concanavalin A and AQA-F (100 µM) for 30 minutes with PC-3 cells. Scale bar = 20 µm.

6.5. 3D Co-localisation Fluorescence

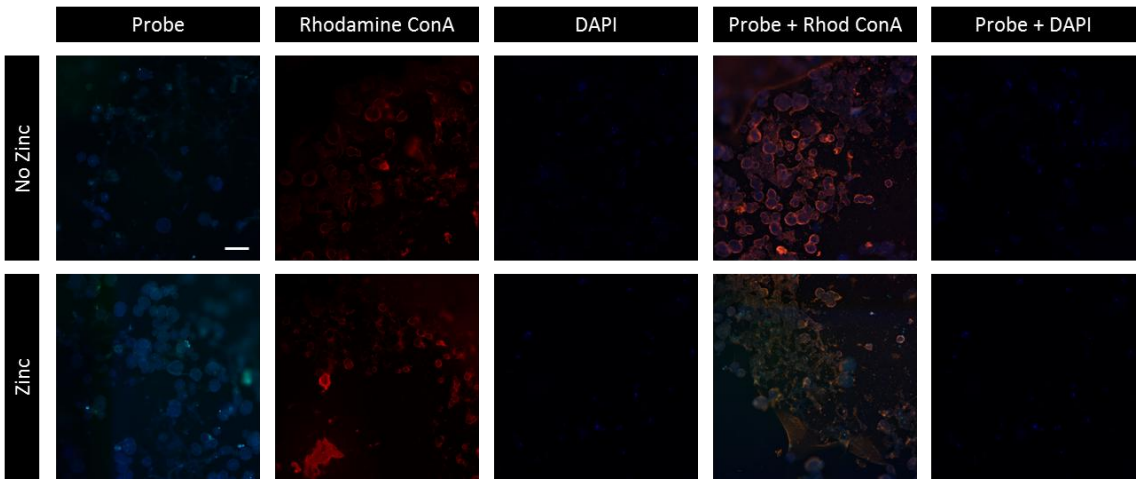

Appendix 10: A collection of micrographs obtained from incubating AQA-F, Rhodamine Concanavalin A and DAPI for 30 minutes with 3D RWPE-1 acini. Scale bar = 20 µm.

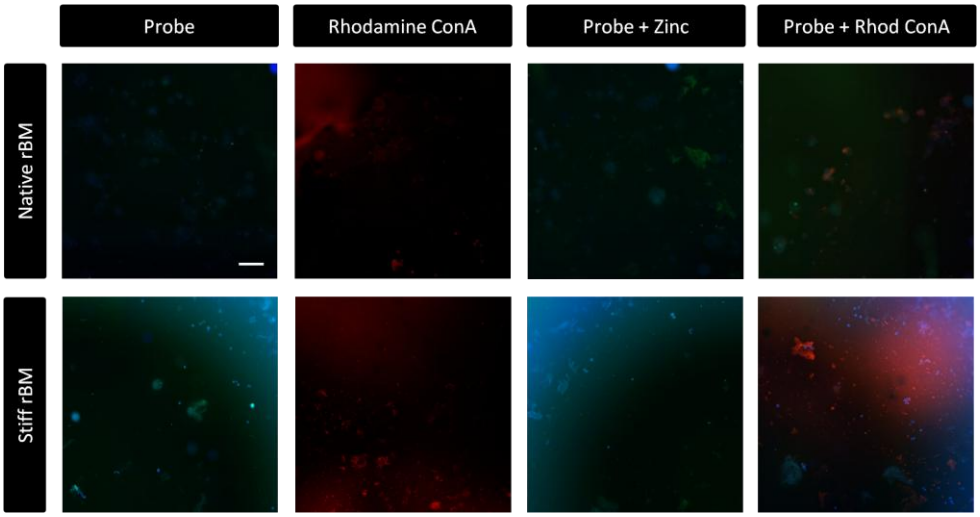

Appendix 11: A collection of micrographs obtained from incubating AQA-F and Rhodamine Concanavalin A for 30 minutes with 3D PC-3 acini cultured on native and stiff reconstituted basement membrane. Scale bar = 20 µm.

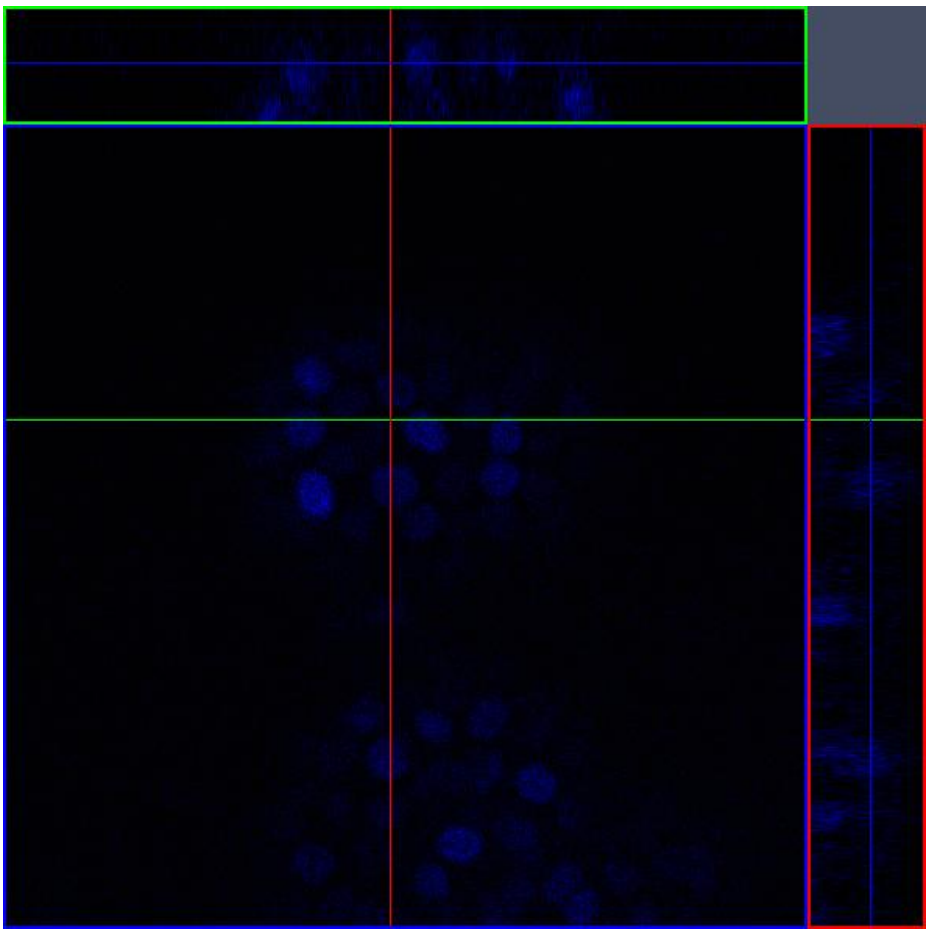

Appendix 12: A z-stack of RWPE-1 acini that have been incubated with DAPI (a nuclear stain).